INFLUENCE OF FUNDAMENTAL MATERIAL PROPERTIES AND AIR VOID STRUCTURE ON MOISTURE DAMAGE OF ASPHALT MIXES

A Dissertation

by

EDITH ARAMBULA MERCADO

Submitted to the Office of Graduate Studies of
Texas A&M University
in partial fulfillment of the requirements for the degree of

DOCTOR OF PHILOSOPHY

May 2007

Major Subject: Civil Engineering

INFLUENCE OF FUNDAMENTAL MATERIAL PROPERTIES AND AIR VOID STRUCTURE ON MOISTURE DAMAGE OF ASPHALT MIXES

A Dissertation

by

EDITH ARAMBULA MERCADO

Submitted to the Office of Graduate Studies of
Texas A&M University
in partial fulfillment of the requirements for the degree of

DOCTOR OF PHILOSOPHY

Approved by:

Co-Chairs of Committee,	Eyad Masad
	Amy Epps Martin
Committee Members,	Robert L. Lytton
	Hamn-Ching Chen
	David S. Schechter
Head of Department,	David V. Rosowsky

May 2007

Major Subject: Civil Engineering

ABSTRACT

Influence of Fundamental Material Properties and Air Void Structure on Moisture Damage of
Asphalt Mixes. (May 2007)

Edith Arámbula Mercado, B.S., Instituto Tecnológico y de Estudios Superiores de Monterrey;

M.S., Texas A&M University

Co-Chairs of Advisory Committee: Dr. Eyad Masad
Dr. Amy Epps Martin

Moisture damage in asphalt mixes refers to the loss of serviceability due to the presence of
moisture. The extent of moisture damage, also called moisture susceptibility, depends on internal
and external factors. The internal factors relate to the properties of the materials and the
microstructure distribution, while the external factors include the environmental conditions,
production and construction practices, pavement design, and traffic level.

The majority of the research on moisture damage is based on the hypothesis that
infiltration of surface water is the main source of moisture. Of the two other principal
mechanisms of water transport, permeation of water vapor and capillary rise of subsurface water,
the latter has been least explored. A laboratory test and analysis methods based on X-ray
computed tomography (CT) were established to assess the capillary rise of water. The amount
and size of air voids filled with water were used in the capillary rise equation to estimate the
distribution of the contact angles between the water and the mastic. The results were able to
show the influence of air void size on capillary rise and contact angles.

The relationship between air void structure and moisture susceptibility was evaluated
using a fundamental fracture model based on dissipated energy of viscoelastic materials.
Detailed description is provided in this dissertation on the deduction of the model equation, the
selection of the model parameters, and the required testing protocols. The model parameters
were obtained using mechanical tests and surface energy measurements. The microstructure of
asphalt mixes prepared in the laboratory having different air void structures was captured using
X-ray CT, and image analysis techniques were used to quantify the air void structure and air
void connectivity. The air void structure was found to influence the mix resistance to moisture
damage.

To validate the fracture model, asphalt mixes with known field performance were tested. The results demonstrated that the fracture model is an effective tool to characterize moisture susceptibility. In addition, the model showed good correlation with the reported field performance of the asphalt mixes.

The findings of this study will be useful to highway engineers to evaluate asphalt mixes with alternative mix designs and internal air void structures and to estimate the rate of moisture infiltration in order to maximize the resistance of asphalt mixes to moisture damage.

I dedicate this work to my beloved parents,

Martín

Lilia Raquel

and to my dear sisters,

Ivette

Lizette

Anette

TABLE OF CONTENTS

LIST OF FIGURES

LIST OF TABLES

CHAPTER I

INTRODUCTION

Transportation infrastructure is a key element for every country; it facilitates the movement of goods and people and thus allows economic and social advancement. Among the different types of transportation infrastructure, streets and highways are the principal means of personal mobility, freight movement, and transit operations. In 2005 there was approximately 4 million miles of rural and urban roads in the United States (U.S.), of which about 2.6 million miles were paved with either asphalt mix or Portland cement concrete. Of these high-type roads, which have a combined surface and base thickness of 175 mm (7 in) or more, about 91 percent were made of asphalt mix built over either flexible or rigid base (FHWA 2006). As shown in Figure 1.1, the increase in the total and paved roads from the early 1940s to the year 2005 follows a linear trend. The total road count increased from 3.3 million miles to about 4 million miles, while paved roads increased from around 600,000 to 2.6 million miles, which represents more than a four-fold increase (FHWA 1996; 1997; 1998; 1999; 2000; 2001; 2002; 2003; 2004; 2005).

The increase in the number of paved roads is a direct response to the rising demand on the transportation infrastructure. A survey conducted in the U.S. in 2001 showed that about 87 percent of daily trips were made using personal vehicles. In addition, the average number of vehicles per household was almost two, and the number of households having three or more vehicles increased from 19 percent in 1995 to 23 percent in 2001 (Hu and Reuscher 2004). Figure 1.2 shows that the number of motor-vehicle registrations has grown linearly from around 35 million in 1941 to around 241 million in 2005, almost a seven-fold increase (FHWA 1996; 1997; 1998; 1999; 2000; 2001; 2002; 2003; 2004; 2005; 2006).

On the other hand, the total disbursement on roads, at all levels of government, increased from $2.5 billion in the early 1940s to around $153 billion in 2005, a 62-fold increase. Through the years, maintenance and traffic services have represented, on average, 27 percent of the total disbursement. For example, in 2005 of the total $153 billion expended, around $38 billion corresponded to maintenance and traffic services (FHWA 2006). As shown in Figure 1.3, increases in both the total and maintenance expenditures follow an exponential trend, contrary to the linear trends presented by the number of constructed miles of roads and the number of

---

This dissertation follows the style of the *Journal of Materials in Civil Engineering*.

vehicle registrations (Figures 1.1 and 1.2). Since the early 1980s, the average annual increase in maintenance expenditures has been about $1 billion per year. These statistics expose the urgent need for building better, long-lasting, and more efficient roads and preventing or minimizing asphalt pavement distresses.
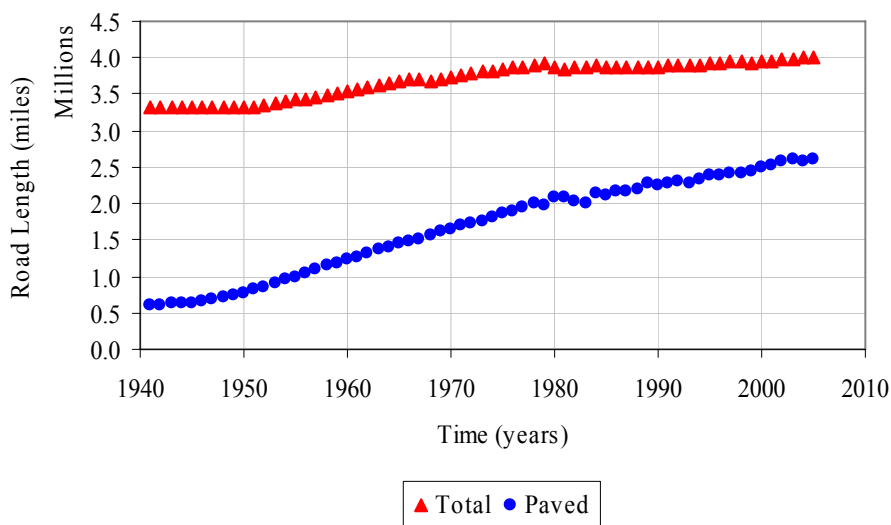
Figure 1.1. Total and paved road length per year
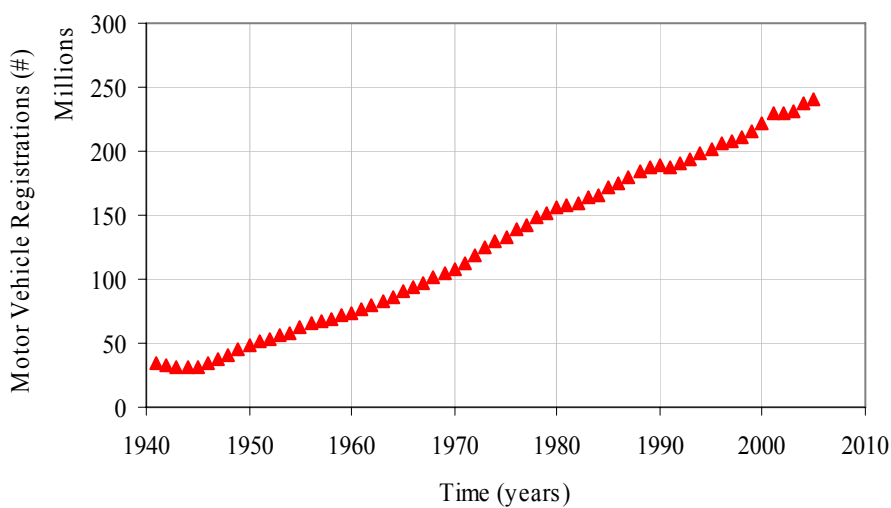
Figure 1.2. Number of motor vehicle registrations per year
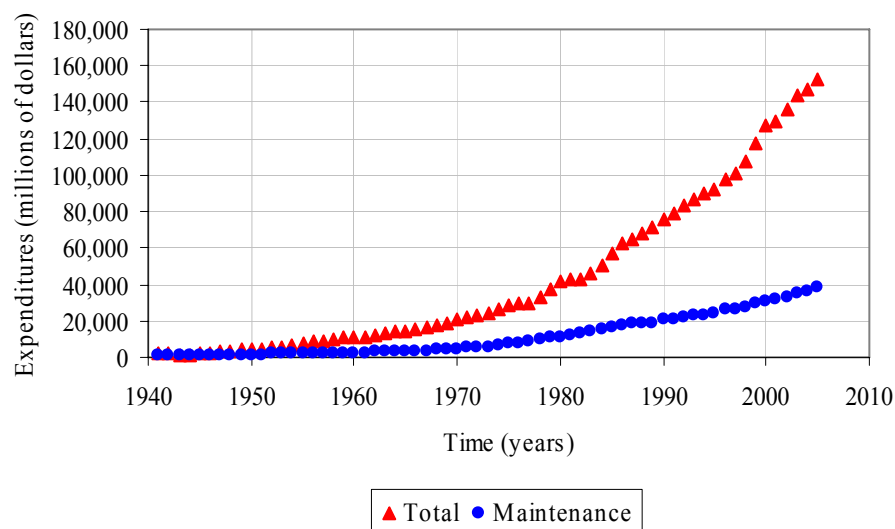
Figure 1.3. Total and maintenance expenditures per year

The condition of the roads has a direct impact on travel costs, from vehicle operations, to traffic delays, to crash-related expenses. Roads in poor condition cause vehicle wear, tear, and even damage. Also, traffic queuing and delays occur when vehicles slow down to avoid important pavement distresses (e.g., potholes) or when the road surface fails to provide safe maneuvering and/or adequate stopping conditions.

Many of the principal distresses in asphalt pavements initiate or increase in severity due to the presence of water. When water and water vapor are present in the pavement, the mechanical properties of the material deteriorate and the serviceability of the pavement is reduced. Moisture damage is the term used to encompass the detrimental effects that moisture in liquid or vapor form have on the pavement structure and on the asphalt mix. Researchers have defined moisture damage as "the progressive functional deterioration of a pavement mix by loss of the adhesive bond between the asphalt and the aggregate surface and/or loss of the cohesive resistance within the asphalt cement principally from the action of water" (Kiggundu and Roberts 1988).

Moisture damage in asphalt pavements is a topic of concern among researchers and highway agency officials. For instance in the early 1980s in the state of Texas, the increasing incidence of moisture-related distresses motivated researchers and state officials to conduct a

study to identify the causes and propose corrective and preventive solutions to the problem (McGennis et al. 1984). Also, a survey conducted in the early 1990s showed that 34 states in the U.S. observed moisture damage in their pavements, with the majority of agencies reporting up to 20 percent of their pavement infrastructure experiencing moisture damage (Hicks 1991). Even states with limited amounts of rainfall, such as Arizona, reported 30 to 50 percent of their pavement infrastructure experiencing moisture-related distresses. An investigation conducted by the Colorado Department of Transportation (DOT) in 2002 showed that 82 percent of the DOTs and other federal agencies in the U.S. applied some sort of treatment to prevent moisture damage in asphalt pavements such as anti-stripping liquids or lime and that 87 percent required testing for moisture sensitivity. Also, around 20 percent of those agencies and DOTs were funding research projects to expand their knowledge on the nature of the problem, to develop and improve test procedures, and to correlate laboratory test results with field performance (Hicks et al. 2003). These figures show that moisture damage is an extensive and prevalent problem in the U.S. and that although much is already known about the origin and nature of the problem, there are gaps in knowledge and therefore studies are needed in order to better understand and solve the problem.

Objective and Research Tasks

The objectives of this study are to investigate (using experimental and analytical methods) the influence of air void structure and fundamental material properties on moisture transport and moisture damage of asphalt mixes. Air void structure is a term that refers to the air void content, size distribution, and connectivity in the asphalt mix sample.

This study was divided into two main phases. The first phase explored permeability and capillary rise as mechanisms of water transport, while the second phase consisted of characterizing moisture damage by taking into account the air void structure of the mix and other fundamental properties. The analysis of moisture damage was conducted using a fracture model for viscoelastic materials. The specific research tasks are detailed in the following sections.

Task 1: Measurement of Material Properties and Preparation of Asphalt Mixes

The surface energy of the aggregates and the asphalt binder was measured using specialized laboratory techniques, and the aggregate imaging system (AIMS) was used to obtain the properties of the aggregates. Using these materials, asphalt mix samples were prepared in the

laboratory using the Superpave gyratory compactor (SGC). The samples were prepared using two different aggregate gradations and compaction angles. Half of the samples were moisture conditioned. The job mix formula corresponded to a Superpave type C mix with a nominal maximum aggregate size of 12.5 mm (0.5 in) that was used by the Texas DOT (TxDOT) in the construction of highway US 59.

Task 2: Characterization of the Microstructure of the Asphalt Mixes

Consistent with the objective of this study, the air void structure of the asphalt mix samples was one of the principal characteristics of interest. X-ray computed tomography (CT) and image analysis techniques were used to evaluate the air void structure of the samples. Several image analysis software and computer algorithms were used to analyze the X-ray CT images and quantify the air void content, size distribution, and connectivity. Based on a preliminary image analysis, a special trimming technique was used to further induce dissimilar air void structures.

Task 3: Study of the Mechanisms of Water Transport

Many researchers have assumed that the main cause of moisture damage is the permeation of rainwater from top to bottom of the asphalt mix and pavement structure. This assumption is reasonable due to the hydrophobic nature of the asphalt binder used in the preparation of the asphalt mix. However, the aggregate coating consists not only of pure asphalt binder but also of a mix of asphalt binder and fine aggregate particles, or mastic, which is capable of attracting water to its surface. Even in very dry environments, moisture-related distresses have been observed in asphalt pavements, which mean that besides water permeation other mechanisms such as capillary rise and diffusion are responsible for the occurrence of moisture damage. In this phase of the study, permeability and capillary rise were the two mechanisms of water transport studied. Moisture diffusion has been previously investigated in a study by Kassem et al. (2006).

Permeability is a property of a porous media to transmit and drain water. The constant head method was used to measure permeability. Permeability values were estimated using approximate equations and corroborated analytically using a computer algorithm to measure vertical air void connectivity within the asphalt mix sample. The rise of water in asphalt mixes due to capillary action was measured using a laboratory test setup and X-ray CT and image analysis techniques. The test setup allowed asphalt mix samples to sit in a shallow water bath for several weeks, and the level of water rise was determined after scanning the samples during the

wetting period. The periodically acquired scans were compared to scans acquired initially on the samples in a dry state using a computer algorithm that aligns and subtracts one image from the other in order to visualize the voids filled with water. The connectivity of the air voids was also explored and the results used to estimate the contact angle of the mastic.

Task 4: Use of Dynamic and Relaxation Tests to Examine Moisture Damage

Dynamic and relaxation tests were used to characterize the moisture damage of the asphalt mix samples prepared in the laboratory. The tests were performed on both unconditioned and conditioned samples, and their efficiency was assessed based on statistical analysis. The dynamic modulus test consisted of the application of a sinusoidal cyclic compressive load on the sample while maintaining the strain within a specific range. The relaxation test, performed in both direct tension and compression, consisted of the application of a static trapezoidal-shaped strain. A statistical analysis was used to evaluate the effectiveness of the tests in differentiating between the conditioned and unconditioned response and between the responses of samples with different air void structures.

Task 5: Development of a Fracture Model to Assess Moisture Damage

A fracture model for viscoelastic materials based on Paris' fracture law was used to characterize moisture damage in the asphalt mix samples prepared in the laboratory. The parameters of the crack growth model were acquired by performing several mechanical tests on the samples: relaxation, direct dynamic tension, and tensile strength. In addition, surface energy measurements were required as inputs to the model. The ratio of the conditioned to unconditioned response was used as an indicator of moisture susceptibility and to rank the mixes according to their expected performance.

To corroborate the effectiveness of the crack growth model, several asphalt mixes from the states of Texas and Ohio with known field performance were evaluated. The original aggregates and asphalt binders were used to reproduce the mix designs in the laboratory. The resulting ranking of the conditioned to unconditioned crack growth ratio was compared against the reported field performance.

Dissertation Outline

This document consists of eight chapters. The present chapter (Chapter I) demonstrates the significance of the topic, details the research objective and specific tasks, and provides the general outline for the dissertation. Chapter II provides a literature review on moisture damage including a discussion of the internal and external factors that influence moisture damage, the mechanisms of moisture damage, the distress manifestations of moisture damage in asphalt pavements, the measures used to control moisture damage, and the laboratory tests used to assess moisture damage.

Chapter III provides details about the material used to prepare the asphalt mix samples in the laboratory, the type and origin of the materials, the aggregate properties, the cohesive and adhesive surface energies of the asphalt binder and the aggregate, the mix design and gradations, and the mixing and compaction procedures. In addition, Chapter III includes information about the use of X-ray CT technology, image acquisition, and the different software and computer algorithms developed and used for image analysis. Details about the air void measurements in the laboratory and moisture conditioning are also provided in Chapter III.

The mechanisms of water transport are discussed in Chapter IV, including information on diffusion studies, laboratory measurements and estimations of permeability, and the capillary rise experiment. An explanation of the image analysis techniques used to estimate air void connectivity to corroborate permeability and estimate the level of water rise in the capillary rise experiment is included. In addition, the laboratory setup for the capillary rise experiment and the image analysis technique to estimate the contact angle of the mastic are explained. Chapter V includes the description of the dynamic and relaxation test protocols used to evaluate the moisture susceptibility of the asphalt mixes. Details about the statistical analysis performed on the results of these tests are also included.

The development of the fracture model for viscoelastic materials, the mechanical test protocols required to obtain the inputs to the model, and the ranking of the mixes according to the conditioned to unconditioned crack growth ratio are presented in Chapter VI. The description of the mixtures and test setups used to validate the fracture model are included in Chapter VII. Finally, Chapter VIII summarizes the main findings, provides conclusions and recommendations, and includes proposed future research work.

CHAPTER II
BACKGROUND ON MOISTURE DAMAGE

In this chapter, a literature review is presented. The majority of the topics have been extensively discussed by other authors and therefore the intent is not to provide an exhaustive report about each subject, but rather to highlight the main aspects related to the occurrence of moisture damage. The internal and external factors that influence moisture damage, mechanisms of moisture damage, distress manifestations of moisture damage in the pavement, measures used to control moisture damage, traditional laboratory tests used to assess moisture damage, surface energy methods used to estimate moisture damage, and the dynamic mechanical analyzer are discussed in the following sections.

Factors That Influence Moisture Damage

In the presence of water, the level and extent of moisture damage in asphalt mixes depends on the properties and interactions of its main components: aggregate, asphalt binder, and air voids. Variables such as the amount of water, residence period, and moisture state (flow, saturation, or diffusion) in the pavement are important, as well as the design and characteristics of the pavement structure. Additional external mechanisms such as the environmental conditions, the production and construction methods, and the level of traffic also play important roles in the occurrence of moisture-related distresses in the pavement.

The reason that water causes damage stems from its lower viscosity and surface tension, which translates into a greater affinity for the aggregate surface as compared to the attraction between the asphalt binder and the aggregate. This effect can be observed in the schematic of Figure 2.1, which represents a drop of asphalt binder in contact with an aggregate that is immersed in water (Figure 2.1a). As time progresses the contact angle, θ, between the two materials in the presence of water increases (Figure 2.1b) until the contact angle becomes large enough (while [180 - θ] decreases) that the asphalt binder loses contact with the aggregate surface (Figure 2.1c).
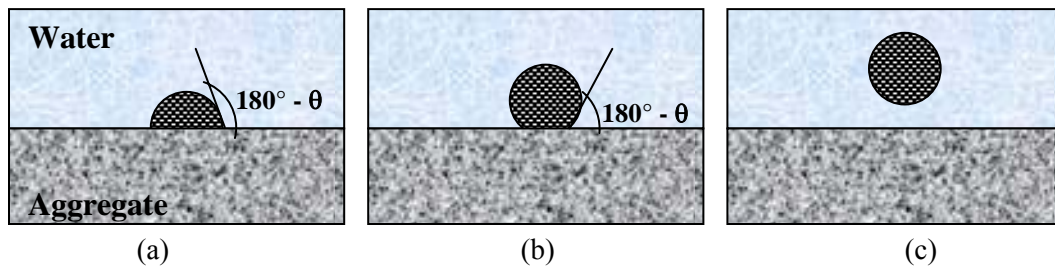
Figure 2.1. Schematic of the effect of water on an asphalt binder drop in contact with the surface of an aggregate (Adapted from Hicks 1991)

Internal Factors

The internal factors that influence moisture damage are directly related to the properties of the materials that form the asphalt mix: aggregates, asphalt binder, and air voids. The following sections provide a description of the properties of these different components and their relationship to the occurrence of moisture damage.

Aggregate and Asphalt Binder Properties

Several properties of the aggregate influence the moisture susceptibility of the asphalt mix: shape, texture, angularity, porosity, surface area, cleanliness, moisture content, mineralogical composition, and surface energy. The aggregate surface characteristics such as shape, texture, and angularity play an important role in the occurrence of moisture damage. If the aggregate is angular and has a rough texture, the adhesion and mechanical interlock between the asphalt binder are greater than if the aggregate is smooth and rounded (McGennis et al. 1984). However, highly angular aggregates are in some instances hard to coat uniformly and their edges often puncture the asphalt binder film, making the mix more susceptible to moisture damage (Hicks 1991). High porosity and absorption capacity of the aggregate allow the asphalt binder to penetrate deeper into the pores, crevices, and capillaries at its surface and to improve the mechanical interlock between the two materials. A large aggregate surface area also provides an improved bond with the asphalt binder because of the increased contact region between the two materials. Aggregates in stockpile condition are often moist and covered with dust; these two elements are detrimental since dust tends to increase the asphalt binder viscosity and moisture disrupts the bond between the asphalt binder and the aggregate (Little and Jones 2003). The mineralogical composition of the aggregate in terms of its hydrophilic and hydrophobic nature and its affinity to the asphalt binder are also important. Aggregates with high carbonate content

(hydrophobic or basic), such as limestone, are easier to coat and form a stronger bond with the asphalt binder than aggregates with high silica content (hydrophilic or acidic) like sandstone, for example (Emery and Seddik 1997). In addition, the chemical reaction that takes place between aggregates with high carbonate content and asphalt binder is usually stronger in the presence of water (Hicks 1991).

The principal properties of the asphalt binder that influence moisture damage are thickness, viscosity, chemical composition, aging, and surface energy. The thickness of the asphalt binder film coating the aggregate dictates the type of moisture damage failure; adhesive failure usually occurs in thinner films whereas in thicker films the failure is mainly cohesive. Authors have used micromechanics to examine the effect of asphalt binder thickness and determined that thicker asphalt binder films have a lower cohesive tensile strength while thinner asphalt binder films have a lower adhesive tensile strength (Lytton et al. 2005). It is often desirable to have an asphalt binder with better wetting ability to coat and completely cover the aggregate. Chemical compounds in the asphalt binder also have an effect on the moisture susceptibility of the mix; carboxylic acids and sulfoxide compounds are in general undesirable because they attach easily to the aggregate surface but are also removed with ease in the presence of water. On the other hand, nitrogen and phenol bases are usually desirable because of their lower desorption in the presence of water (Hicks 1991; Little and Jones 2003). In addition, asphalt binder aging makes the asphalt mix prone to moisture damage.

The surface energies of the asphalt binder and the aggregates are also important variables in terms of moisture damage. The non-uniform charge present at the surface of these materials occurs because of the missing interactions with the bulk phase. This energetically unfavorable condition increases the surface free energy of the system and attracts other materials' surface molecules to satisfy equilibrium. The adhesive bond between the asphalt binder and the aggregate depends on their individual surface free energy values. The Gibbs free energy (G), used to define the energy state of a system and predict if a process is likely to occur, is defined in this context as the excess surface free energy and is used to quantify the free energy of adhesion between different materials and the free energy of cohesion within a single material (Hefer 2004).

In the thermodynamic theory, surface energy (γ) is defined as the work required to create a new surface. The relationships between the Gibbs free energy, surface energy, and the work of adhesion (W^a) and cohesion (W^c) are as follows:

$$W_i^c = -\Delta G_i^c = 2\gamma_i \tag{2.1}$$

$$W_{ij}^a = -\Delta G_{ij}^a = \gamma_i + \gamma_j - \gamma_{ij} \tag{2.2}$$

where γ_i and γ_j are the surface energies of the two different materials and γ_{ij} is the interfacial surface energy between the two materials. The work of adhesion represents the energy required to create a new surface, which is equal to the surface energy of each material minus the interfacial surface energy that is lost when the two new surfaces are created. In addition, the surface energy of a single-phase material can be expressed in terms of its polar and non-polar components as follows (Hefer 2004):

$$\gamma_i = \gamma_i^{LW} + \gamma_i^{AB} \tag{2.3}$$

where γ_i^{AB} is the polar acid-base component (*AB*) and γ_i^{LW} is the non-polar Lifshitz-van der Waals component (*LW*). Likewise, the free energy of cohesion and adhesion can be defined in terms of the polar and non-polar components:

$$\Delta G_i^c = -2\gamma_i = \Delta G_i^{cLW} + \Delta G_i^{cAB} \tag{2.4}$$

$$\Delta G_{ij}^a = \gamma_{ij} - \gamma_i - \gamma_j = \Delta G_{ij}^{aLW} + \Delta G_{ij}^{cAB} \tag{2.5}$$

The *LW* component is assumed to characterize the interaction between symmetric molecules, and therefore a geometric mean is used to estimate its value:

$$\Delta G_{ij}^{aLW} = -2\sqrt{\gamma_i^{LW} \gamma_j^{LW}} \tag{2.6}$$

The *AB* component, on the other hand, pairs the acid (+) and base (-) fractions of the different materials (VanOss et al. 1988):

$$\Delta G_{ij}^{aAB} = -2\left(\sqrt{\gamma_i^+ \gamma_j^-} + \sqrt{\gamma_i^- \gamma_j^+} \right) \tag{2.7}$$

The previous relationships are not limited to two materials and can be expanded to the interaction of more than two phases:

$$\Delta G_{ikj}^a = \gamma_{ij} - \gamma_{ik} - \gamma_{jk} = \Delta G_{ikj}^{aLW} + \Delta G_{ikj}^{aAB} \tag{2.8}$$

In this case, the work of adhesion is formed by the interfacial surface energy between two materials and the interfacial surface energies between each material and the third phase. Equation 2.8 is especially useful when analyzing the effect of water (*k* component) on the bond surface energy of different asphalt binders and aggregates. As will be discussed later in this

chapter, there are different experimental methods to measure the surface energy components of the asphalt binder and the aggregate.

Permeability and Air Void Structure

Permeability can be defined as the capacity of a porous material to let water flow through its voids. This parameter has long been associated with the occurrence of moisture damage, and consequently, several agencies have prescribed maximum values of in-place air voids in an effort to minimize the effects of moisture damage and maximize the durability of the pavement. Extensive research has been conducted to measure, calculate, and simulate fluid flow in porous media (Al-Omari et al. 2002; Al-Omari and Masad 2004; Masad et al. 2004; 2006a; Maupin 2000; Mohammad et al. 2003). As expected, the results of many of these studies show that air void structure, size and gradation of the aggregates, asphalt binder thickness, thickness of the asphalt layer, and compaction effort are variables that affect permeability. However, due to the heterogeneity and anisotropic nature of the asphalt mix, it is not always easy to develop a direct relationship between these variables and permeability. In addition, the inherent characteristics of the air void structure such as content, size distribution, and connectivity also need to be considered.

Researchers have used the Kozeny-Carman equation as a basis to develop expressions for approximating permeability based on mix volumetrics (percent air voids, total and absorbed percent asphalt binder, and specific gravity of the asphalt binder and the aggregate), aggregate gradation, and surface area of the aggregates (Masad et al. 2004; 2006a). These equations are generally used during the design and compaction processes to ensure a desirable level of permeability in the field.

Researchers have also looked at the relationship between permeability and air void content and connectivity. As shown in Figure 2.2, they have classified the asphalt mixes based on their air void structure as effective, semi-effective, and impermeable (Chen et al. 2004). The relationship between these characteristics and permeability values is presented in Table 2.1. Effective mixes show a high number of interconnected voids and therefore allow a free flow of water; semi-effective mixes have a smaller number of connected voids and the connections span only part of the mix pavement layer thickness, and the air voids in impermeable mixes are usually isolated with a very small amount of connectivity.

Effective　　　　Semi-effective　　　　Impermeable
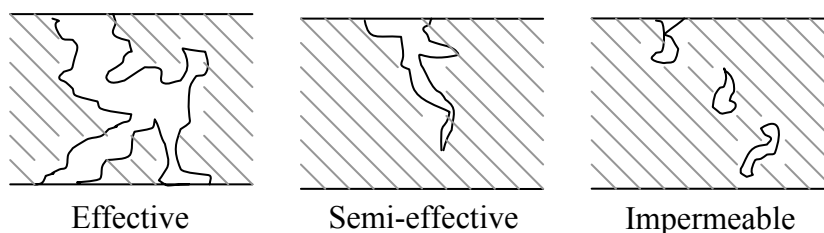
Figure 2.2. Classification of air voids based on connectivity (Adapted from Chen et al. 2004)

Table 2.1. Classification of Air Voids in Terms of Permeability (Adapted from Chen et al. 2004)

k (cm/s)	Permeable condition	Void type	Mix type	Approximate equation [a]	Air void range (%)
10^{-4} or lower	Impervious	Impermeable	Dense	$\ln(k) = 0.432 \cdot x - 13.386$	2 to 8
10^{-4} to 10^{-2}	Poor drainage	Semi-effective	Stone mastic asphalt	$\ln(k) = 0.459 \cdot x - 9.821$	4 to 9
10^{-2} or higher	Good drainage	Effective	Porous asphalt	$\ln(k) = 0.209 \cdot x - 7.017$	12 to 20

[a] x represents the percent air voids

　　　　One of the first efforts to study the relationship between moisture damage and air void content was part of a moisture sensitivity study. Asphalt mixes were prepared in the laboratory and tested before and after moisture conditioning. Researchers observed that the reduced resilient modulus strength of the conditioned samples was a function of the percent air voids of the asphalt mix (Terrel and Al-Swailmi 1994). As shown in Figure 2.3, they classified the mixes as impermeable, pessimum voids, and free drainage. The pessimum voids range corresponded to the air void content where maximum moisture damage was observed. In their study, the lowest retained strength corresponded to an air void content of about 8 percent.

　　　　In addition, researchers have studied the effect of air void size by testing asphalt mixes with different gradations but the same target percent air voids (Birgisson et al. 2003; Masad et al. 2006b). The air void size was determined using X-ray CT and correlated with parameters such as the energy ratio and the ratio of the conditioned to unconditioned number of cycles to failure (N_f) using the indirect tensile test. The results, presented in Figure 2.4, show that there is a range of air void sizes, called pessimum size, where moisture damage is maximized. Also, researchers

concluded that the relationship between moisture damage and permeability is not directly proportional since large moisture damage was evident at intermediate permeability values that corresponded to the pessimum size range (Figure 2.5).
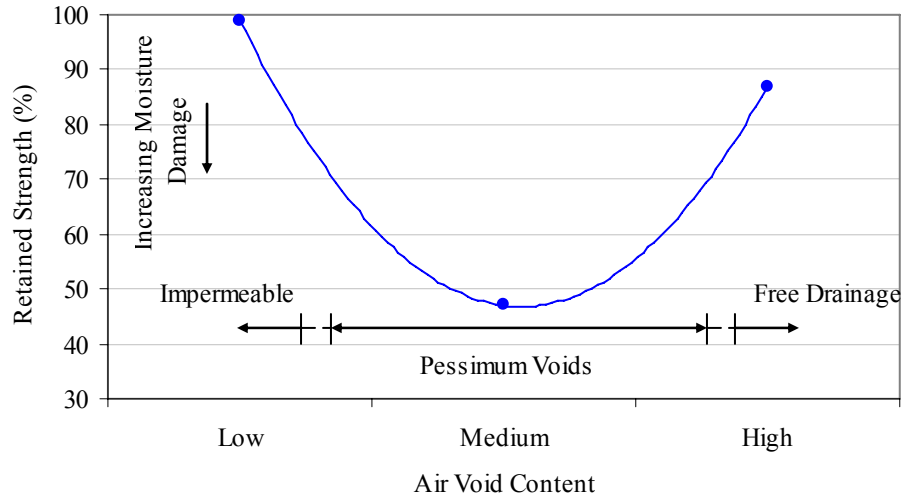
Figure 2.3. Retained strength in the conditioned samples as a function of air void content showing the pessimum voids range (Adapted from Terrel and Al-Swailmi 1994)
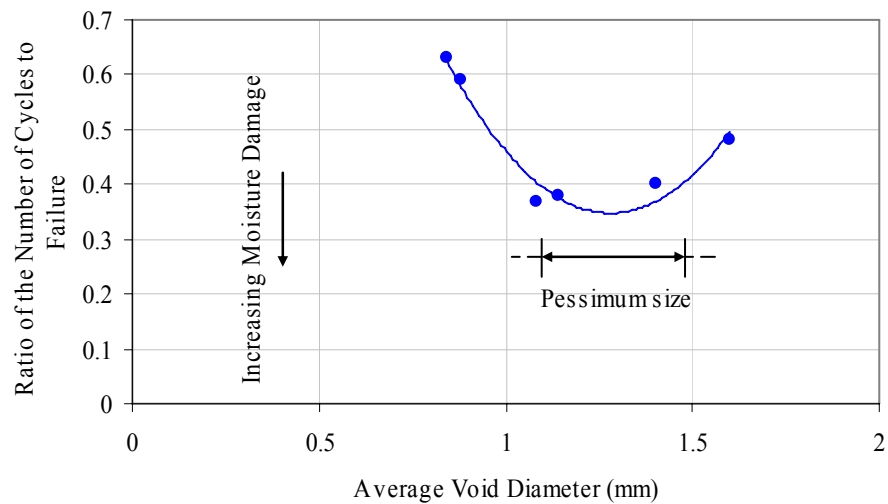
Figure 2.4. Conditioned to unconditioned N_f ratio as a function of air void size showing the pessimum size range (Adapted from Masad et al. 2006b)
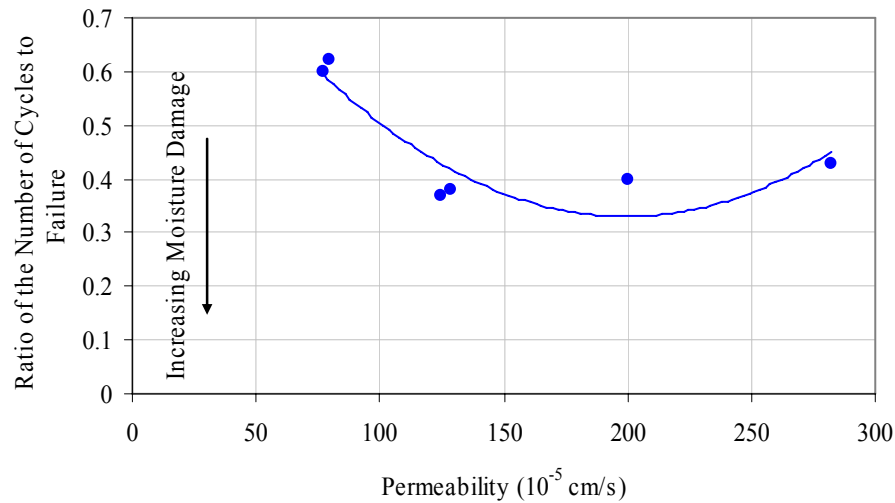
Figure 2.5. Conditioned to unconditioned N_f ratio as a function of permeability (Adapted from Masad et al. 2006b)

Permeability and adequate drainage characteristics are not only important for the surface course but also for the underlying pavement structure. The accumulation of water in the subsurface layers of the pavement usually leads to a reduced load-bearing capacity and accelerates the appearance of distresses. Water saturation in the subsurface layers also promotes vertical bottom-up movement of water through capillary rise. When highly permeable surface layers like permeable friction courses (PFC) or stone matrix asphalt (SMA) are used, the underlying pavement layers should be protected with impermeable barriers such as seal coats (D'Angelo and Anderson 2003).

External Factors

Some of the external factors that influence moisture damage are production, construction, traffic level, and environmental conditions. When the asphalt mix is produced, the aggregates are carried from the stockpile, heated, combined with the hot asphalt binder, and loaded in trucks to be transported to the field site. Segregation and improper aggregate drying need to be avoided during the production process to prevent later moisture damage problems in the pavement. The aggregates used for production need to be clean and dry and therefore kept in stockpiles where drainage is maximized while segregation is minimized. Also, the stockpiles need to be separated

from each other to avoid contamination but without causing aggregate degradation (St. Martin et al. 2003). During the heating process, moisture content measurements should be obtained to guarantee the aggregates are completely dry. Also, when the aggregates and the asphalt binder are combined, the mix design should be followed closely in terms of the amount of asphalt binder and the aggregate gradation (Hicks et al. 2003). The final product needs to be properly loaded into trucks to avoid segregation and transported promptly to avoid draindown of the asphalt binder and excessive cooling. These provisions help ensure that the pavement achieves the correct density, that the aggregates are properly coated, and that thermal segregation is minimized (St. Martin et al. 2003).

The construction process is also important to create a pavement with improved resistance to moisture damage; insufficient or poor compaction is one of the principal factors researchers report in relation to moisture damage (Hicks 1991). Special attention should be placed on the compaction of longitudinal joints between the travel lanes of the pavement and the shoulders, as improper densification could allow water to penetrate into the asphalt mix and the pavement structure (St. Martin et al. 2003). In addition, the compaction equipment should be of appropriate weight, and excessive rolling should be prevented in order to avoid fracturing the aggregates. Researchers have also looked at the effect of compaction-induced cracks as a route for water permeation, circulation, and accumulation. They observed that moisture damage occurred even in asphalt mixes with very low percent air voids, and they concluded that construction-induced cracks served as air void connectors and therefore have the effect of increasing the total percent air voids in the asphalt mix (Chen et al. 2004; Mohamed et al. 1993).

Compared to the air void content used during mix design, government agencies usually specify a higher initial air void content in the mix in the field (after construction). In Texas, for example, the in-place requirement for air void content for dense mixes is between 5 and 9 percent, while the design target air void content is 4 percent (TxDOT 2004a). The difference in the in-place and design values derives from expected mix densification under traffic. The traffic level is important, especially when a pavement is in a saturated state, since the increased pore pressure and the tension/compression phenomenon caused at the surface by the moving wheels can accelerate the occurrence of moisture-related distresses (Kiggundu and Roberts 1988).

Environmental conditions include temperature fluctuations, wet-dry cycles, freeze-thaw cycles, and the pH of the water. When the temperature of the air or the base material is too low, pavement construction is not advisable, as proper density might be difficult to achieve (St.

Martin et al. 2003). Wet-dry cycles dictate the amount of rainfall and the level and fluctuations of the water table underneath the pavement. Freeze-thaw cycles accelerate the occurrence of moisture-related distresses because the expansion of the water in the voids leads to increased pore pressure and subsequent fracture of the asphalt binder film coating the aggregates (Hicks 1991). The pH of the water at the interface of the asphalt binder and aggregate can also influence moisture damage; the higher the pH of the water, the more moisture susceptible the asphalt mix will be (Kiggundu and Roberts 1988; Little and Jones 2003). A summary of the internal and external factors influencing the occurrence and prevalence of moisture damage in asphalt pavements is presented in Table 2.2.

Table 2.2. Summary of the Factors That Influence Moisture Damage in Asphalt Pavements

Type	Factor	Variables
Internal	Aggregate	Shape
		Texture
		Angularity
		Porosity
		Surface area
		Cleanliness
		Moisture content
		Mineralogical composition
		Surface energy
	Asphalt binder	Thickness
		Viscosity
		Chemical composition
		Aging
		Surface energy
	Air void structure	Content
		Size
		Connectivity
		Permeability
External	Production	Physical segregation
		Aggregate drying
		Asphalt binder draindown
		Thermal segregation
	Construction	Equipment
		Method
	Environment	Temperature
		Freeze-thaw cycles
		Wet-dry cycles (rainfall)
		Water table level (saturation)
		Water pH
	Traffic	Heavy loads
		High levels

Mechanisms of Moisture Damage

As will be discussed Chapter IV, there are different ways in which water can access the asphalt pavement, which mainly depend on the environmental conditions and the air void structure. When water reaches the asphalt mix, it begins to interact with the asphalt binder and the aggregate. Therefore, depending on the aggregate and asphalt binder properties, the mechanism of water transport, and the amount and residence period of the water, moisture damage can:

    a) reduce the cohesive strength of the asphalt binder, lead to its dispersion or loss of concentration, and cause an ultimate reduction in the stiffness of the mix, and/or

    b) penetrate the interface between the aggregate and the asphalt binder, reduce the contact between the two materials, and cause an adhesive bond failure.

In open graded mixes, where water in relatively large amounts can flow at somewhat high speeds, water can mechanically 'wash' away the asphalt binder from the aggregate. This process, called advective flow, causes desorption of the asphalt binder and can eventually lead to a bond failure between the asphalt binder and the aggregate. Another process that affects the cohesive properties of the asphalt binder and also the bond between the asphalt binder and the aggregate is diffusion (Kringos and Scarpas 2005). Dispersion of the asphalt mastic and spontaneous emulsification defined as the "inverted emulsion of water droplets in asphalt cement" (Kiggundu and Roberts 1988) are resulting mechanisms caused by diffusion.

Other mechanisms affecting the cohesive bond energy of the asphalt binder and adhesive bond energy between the asphalt binder and the aggregate are detachment and displacement (Kiggundu and Roberts 1988; Little and Jones 2003). As shown in Figure 2.6, detachment is the separation of the asphalt binder film from aggregate under the influence of moisture but with no apparent damage to the asphalt binder film. This mechanism usually takes place when the aggregates are covered with dust or improperly dried during the construction process or when the asphalt binder film coating the aggregate is very thin, allowing moisture to easily reach the interface of the two materials by diffusion.

| Well coated aggregate | Detachment | Displacement |
| | Coating without adhesion | Defective coating |
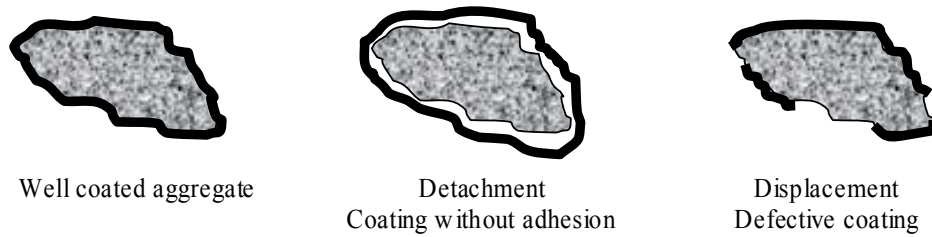
Figure 2.6. Schematic of the detachment and displacement failure mechanisms

Displacement is the removal of the asphalt binder film coating from the aggregate surface by water. Contrary to the detachment mechanism, the defects and discontinuities in the asphalt binder film allow water to access the interface between the two materials (Figure 2.6). This mechanism is likely to take place when the aggregate is not completely coated with the asphalt binder during the production process, is too angular and punctures the asphalt binder film, or is fractured during the compaction process. Freeze-thaw cycles can also cause film rupture. A summary of the moisture damage mechanisms, their definitions, and potential causes is shown in Table 2.3.

Table 2.3. Summary and Definition of the Mechanisms of Moisture Damage

Mechanism	Definition	Potential causes
Desorption	Wash away of the asphalt binder by mechanical action	High permeability
Detachment	Separation of the asphalt binder and the aggregate without apparent damage of the asphalt binder film	Dirty aggregate Moist aggregate Thin asphalt binder film
Dispersion	Loss of cohesive strength in the asphalt binder	Low cohesive bond surface energy Hydrophilic asphalt binder chemical composition Aged asphalt binder Thin asphalt binder film
Displacement	Removal of the asphalt binder film coating from the aggregate by the action of water	Partially coated aggregate Highly angular aggregate Highly fractured aggregate after compaction Frequent freeze-thaw cycles Low adhesive bond surface energy Hydrophilic asphalt binder chemical composition Hydrophilic aggregate mineralogical composition High water pH
Spontaneous emulsification	Inverted emulsion of water droplets in asphalt cement [a]	Low cohesive bond surface energy Hydrophilic asphalt binder chemical composition High water pH

[a] After (Kiggundu and Roberts 1988)

Distress Manifestations of Moisture Damage in Asphalt Pavements

When water and moisture enter the pavement, reducing the cohesive strength of the asphalt binder and/or displacing the asphalt binder coating the aggregate by one or several of the mechanisms previously described, a distress called stripping becomes visible in the asphalt pavement. Stripping can be classified as raveling or weathering. Raveling is evident at the surface of the pavement and consists of the dislodging of aggregates under the influence of traffic. Weathering, on the other hand, occurs when the asphalt binder coating the aggregate is lost but with no apparent aggregate detachment from the surface of the pavement (Miller and

Bellinger 2003). Initially, it is common to observe signs of weathering at the surface of the pavement that later evolve into raveling under the influence of traffic. Two examples of stripping in the form of raveling are presented in Figure 2.7.

Area of stripping
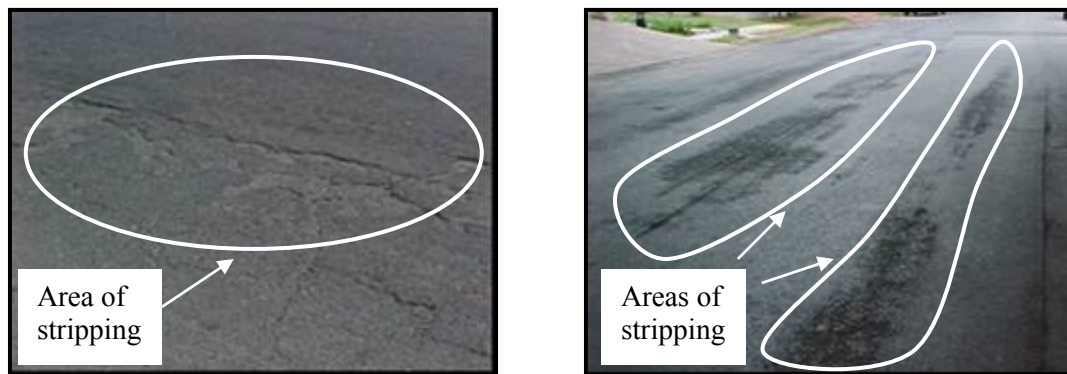
Areas of stripping

Figure 2.7. Examples of stripping in the form of raveling at the surface of the pavement

Some asphalt pavement distresses are directly related to the presence of water in the underlying pavement structure. These include corrugations, pumping, and water bleeding. Corrugations, also called shoving, consist of a localized plastic movement of the asphalt pavement surface in the form of ripples or waves (Figure 2.8). It is usually caused by a reduced cohesive strength in the asphalt binder and/or by excessive moisture in the subgrade that makes the pavement prone to deformations. Pumping and water bleeding occur when water carrying fine material seeps out of the pavement cracks or is ejected under the pressure of the moving traffic loads, which undermines the underlying base material and reduces its load bearing capability (Miller and Bellinger 2003).
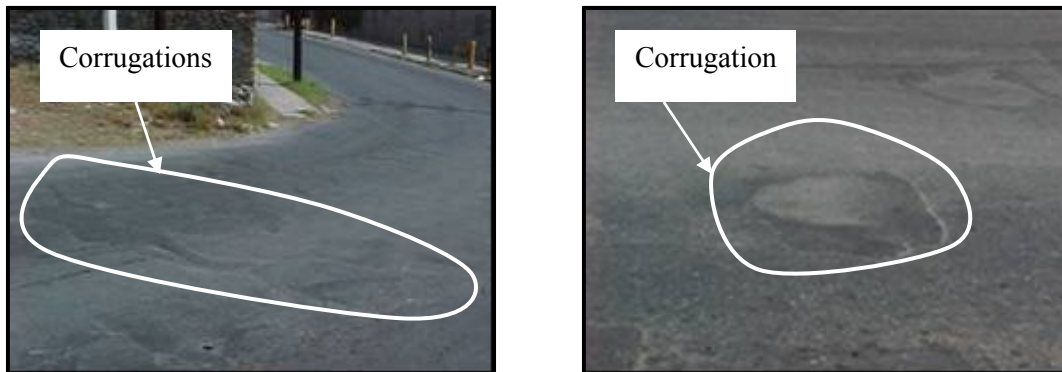
Figure 2.8. Examples of corrugations at the surface of the pavement

Some other types of asphalt pavement failures such as alligator cracking, block cracking, longitudinal and transverse cracking, potholes, shoulder drop off, lane to shoulder separation, patch deterioration, and rutting, although not initiated by the incidence of water, increase in extent and severity due to the presence of water and moisture (Epps et al. 2003). Water reduces the load carrying capacity of the asphalt mix and softens the underlying base, which in turn increases deflections. Cracking and poorly compacted longitudinal joints allow water infiltration into the pavement structure. Other distresses like depressions, for example, prolong the residence period of water at the surface of the pavement, inducing water seepage into the underlying pavement layers and causing bond failure between the aggregate and the asphalt binder in the mix. Figure 2.9 shows examples of the effect of water in the severity of pothole and patch deterioration distresses.

Figure 2.9. Detrimental effect of water in the severity of pothole (left) and patch deterioration (right)

Measures to Control Moisture Damage

Some government agencies prescribe the proper selection and treatment of aggregates and the use of surface seals to minimize the appearance of moisture-related distresses in the pavement. However, the most common corrective treatment consists of the use of chemical additives and lime (Emery and Seddik 1997; Epps et al. 2003; Hicks 1991). The investigation conducted by the Colorado DOT in 2002 showed that of the 82 percent of the agencies in the U.S. that applied some sort of treatment to prevent moisture damage, 56 percent used chemical additives, 29 percent used lime, and 15 percent used a combination of both (Hicks et al. 2003).

The function of the chemical additives, also called liquid anti-strip agents, is to modify the chemical composition and electric charge of the asphalt binder and to reduce the surface tension between the asphalt binder and the aggregate in order to obtain a strong and uniform aggregate coating. The composition of most of the chemical additives used in asphalt mixes are amines, a basic compound derived from ammonia (Hicks 1991). Amines consist of long hydrocarbon chains that are able to efficiently wet the aggregate surface because of their strong affinity to the silica compounds of the aggregates.

Lime, when activated with water, decreases the interfacial tension between the asphalt binder and the aggregate. Lime can be used in dry form, as hydrated lime slurry, or as hot or quicklime slurry. The calcium ions in lime react with the carboxylic acids in the asphalt and replace some cations on the aggregate surface, promoting a strong bond between the silica molecules of the aggregate and the nitrogen in the asphalt binder (Hicks 1991). Other positive effects of lime inclusion are a reduction in the asphalt binder viscosity and a reduction in the formation of oxidation products in the asphalt binder with aging (Emery and Seddik 1997).

Chemical additives are either added to the asphalt binder in a liquid state prior to combining it with the aggregate or mixed with the aggregate. Dry lime can be combined with dry or moist aggregates, and lime slurries are usually combined with moist aggregates. Lime can be introduced at different stages of production, during stockpiling, cold feed operations, or during mixing with the asphalt binder in the pug mill or drum unit.

Traditional Laboratory Tests Used to Assess Moisture Damage

Researchers have focused on evaluating moisture damage by performing laboratory tests on asphalt mixes. These tests are used to provide a qualitative or quantitative measure of the

moisture susceptibility of the asphalt mix. The first tests to evaluate moisture damage, introduced back in the 1920s, were the static immersion test and the boiling test. Both tests, applied to loose asphalt mixes, were based on a visual inspection of the samples after conditioning to determine the degree of moisture damage. Consequently, the evaluation of damage in these qualitative tests was quite subjective and dependent on personnel experience and interpretation. During the 1940s and 1950s, the focus changed toward quantitative test methods performed on compacted asphalt mix samples, such as the immersion compression test. The quantitative methods usually prescribe measuring a certain property of the asphalt mix sample, subjecting the sample to moisture conditioning, and measuring the given property after the conditioning process. The ratio of the conditioned to unconditioned test results is used to estimate the moisture susceptibility of the sample by comparing the value against a prescribed threshold. If the ratio is below the threshold, the mix is classified as susceptible to moisture damage. The ratios of different asphalt mixes can also be used to rank them according to their moisture susceptibility level.

During the 1960s and 1970s, better understanding of the mechanisms of moisture damage resulted in the development of different test protocols, including, among others, the modified Lottman test. This procedure, included in the American Association of State Highway and Transportation Officials (AASHTO) standards, is widely used by many U.S. government agencies and is part of the state-of-the-practice Superpave system (AASHTO 2002c; Asphalt-Institute 1995).The method prescribes an indirect tensile test and specifies a ratio of conditioned to unconditioned strength of above 0.8 for adequate moisture resistance. In the late 1980s and early 1990s, a number of test procedures to evaluate moisture damage were used, including the environmental conditioning system (ECS), the asphalt pavement analyzer (APA), and the Hamburg wheel tracking device (Solaimanian et al. 2003).

The results of the survey performed in 2002 showed that among U.S. DOTs and federal agencies that used laboratory tests to assess moisture susceptibility (Hicks et al. 2003; Solaimanian et al. 2003):

- 69 percent employed the Lottman or modified Lottman tests,
- 13 percent used the Tunnicliff and Root test,
- 10 percent utilized the immersion compression test; and about
- 4 percent used the Hamburg wheel-tracking device.

In addition, a study that compared the results of several laboratory tests to field performance ratings concluded that the percent success or number of correct predictions was (Kiggundu and Roberts 1988):

- 67 percent for the Lottman test, with a strength ratio of 0.7 percent,
- 67 percent for the Tunnicliff and Root test, with a strength ratio of 0.8 percent, and
- 47 percent for the immersion compression test, with a strength ratio of 0.75.

Table 2.4 provides a summary of the most common used laboratory tests according to the 2002 survey. More detailed descriptions of these and other laboratory tests are provided in subsequent sections. Information and additional references regarding other test methods can be found elsewhere (Airey and Choi 2002; Solaimanian et al. 2003).

Table 2.4. Summary of Commonly Used Laboratory Tests to Assess Moisture Damage

Test	Standard	Samples (#)	Dimensions (mm)	Air voids (%)	Conditioning [a]	Damage evaluation [b]
Lottman	Tex 531C	8	100 × 50	7 ± 1.0	GI: *Uc* GII: *VS* 30 min *Fr* 15 h -18 °C *Im* 24 h 60 °C *Im* 4 h 25 °C	$\dfrac{IDT_c}{IDT_u} \geq 0.7$
Modified Lottman	AASHTO T283	6	100 × 62.5	7 ± 0.5	GI: *Uc* GII: *VS* 70-80% *Fr* 15 h -18 °C *Im* 24 h 60 °C *Im* 2 h 25 °C	$\dfrac{IDT_c}{IDT_u} \geq 0.8$
Tunnicliff and Root	American Society for Testing and Materials (ASTM) D4867	6	100 × 62.5	7 ± 1.0	GI: *Uc* GII: *VS* 55-80% Optional *Fr* 15 hr -18 °C *Im* 24 h 60 °C *Im* 1 h 25 °C	IDT Visual inspection
Immersion Compression	AASHTO T162 and ASTM 1075	6	100 × 100	6	GI: *Uc* GII: *Im* 24 hr 60 °C *Im* 2 h 25 °C OR GII: *Im* 4 days 49 °C	$\dfrac{CS_c}{CS_u} \geq 0.75$

[a] GI: group 1, GII: group 2, *Uc*: unconditioned, *VS*: vacuum saturation, *Im*: immersion, *Fr*: freeze
[b] *IDT*: indirect tensile test, *c*: conditioned results, *u*: unconditioned result, *CS*: compressive strength

Lottman Test, Tex 531C

The Lottman test (Tex 531C) was established in the late 1970s as part of a National Cooperative Highway Research Program (NCHRP) study to predict moisture damage in asphalt mixes, and was later adopted by the Texas Department of Transportation (TxDOT) as part of their standard test procedures (Lottman 1978, 1982; TxDOT 1999). According to the TxDOT standard, eight asphalt mix samples 100 mm (4 in) in diameter by 50 mm (2 in) high are compacted to an air void content of 7 ± 1 percent and divided into two groups. One group is the control or unconditioned, the second group is subjected to conditioning consisting of vacuum saturation for 30 min followed by a 15 h freeze at -18 °C (0 °F) and a subsequent submersion in a hot water bath at 60 °C (140 °F) for 24 h. The samples are placed in a water bath at 25 °C (77 °F) for an additional 4 h before testing. An indirect tensile (IDT) test like the one presented in Figure 2.10 is used to evaluate the performance of the samples. The IDT test consists of placing the asphalt mix sample between two square steel bars and applying a compressive load at a constant rate along the diameter of the sample until failure. The compressive load indirectly creates a tensile load in the horizontal direction of the sample. The peak load is recorded and used to compute the tensile strength with the following equation:

$$S_t = \frac{2P}{\pi t D} \tag{2.9}$$

where P is the maximum load, t is the sample thickness, and D is the sample diameter. The ratio of the unconditioned to conditioned indirect tensile strength or tensile strength ratio (TSR) is used to determine the moisture susceptibility of the sample. A threshold value for TSR was established at 0.7 by Lottman (1978).
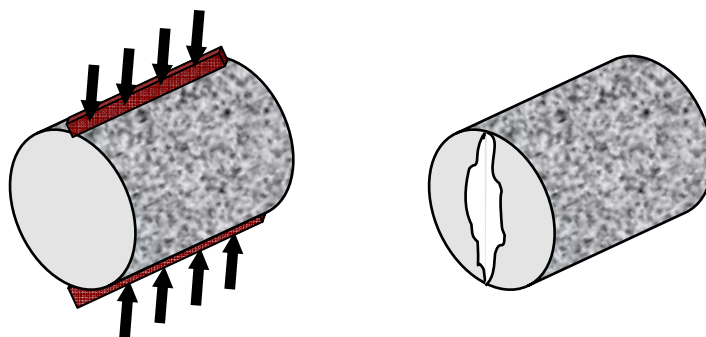
Figure 2.10. Schematic of the indirect tensile test showing the setup and loading of the asphalt mix sample (left) and the asphalt mix sample after failure (right)

Modified Lottman Test, AASHTO T 283

The modified Lottman test included in the Standard Method of Test for Resistance of Compacted Asphalt Mixtures to Moisture-Induced Damage is a modification of the original procedure developed by Lottman and explained in the previous section (AASHTO 2002c). The main difference is in the vacuum saturation procedure. Six asphalt mix samples 100 mm (4 in) in diameter by 62.5 mm (2.5 in) in height are prepared to an air void content of 7 ± 0.5 percent and divided into two groups. One group is left unconditioned while the other group is vacuum saturated for a short time to a level of saturation between 70 to 80 percent. The level of saturation, S', is estimated using the following equation:

$$S' = \frac{100(W_{SSD} - W_D)}{\dfrac{P_a E}{100}} \tag{2.10}$$

where W_{SSD} is the mass of the saturated surface dry sample after vacuum saturation, W_D is the mass of the dry sample, P_a is the percent air voids, and E is the volume of the sample.

The samples are then wrapped in plastic bags and subjected to a freezing cycle at -18 °C (0 °F) for 15 h. Then, the samples are submerged in a hot water bath at 60 °C (140 °F) for 24 h. Finally, the samples are placed in a water bath at room temperature for an additional 2 h. After conditioning, an IDT test is performed on both the unconditioned and conditioned samples. The Superpave standard that prescribes this test for evaluation of moisture susceptibility recommends a minimum TSR value of 0.8 for compliance (Asphalt-Institute 1995).

Tunnicliff and Root Test, ASTM D 4867

A study of antistripping additives in asphalt mixes conducted in the mid 1980s developed the Tunnicliff and Root (ASTM D 4867) laboratory test method, which was later adopted and included in the American Society of Testing and Materials (ASTM) standards (ASTM 2006b; Tunnicliff and Root 1984). Six samples 100 mm (4 in) in diameter by 62.5 mm (2.5 in) in height are compacted to an air void level of 7 ± 1 percent and divided into two subsets; one is the unconditioned subset, and the other is moisture conditioned. Liquid antistripping additives can be added to the mix. The conditioned subset of samples is partially saturated with a vacuum to a degree of saturation between 55 and 80 percent. Equation 2.10 is used to compute the degree of saturation. An optional freeze-thaw cycle like the one included in the modified Lottman procedure follows. Then, the samples are soaked in water at 60 °C (140 °F) for 24 h and finally

submerged in water at 25 °C (77 °F) for an additional hour. An IDT test is performed at room temperature on both subsets; the loading is done at a constant rate until failure. The evaluation of moisture susceptibility is based on a visual inspection of the failed faces and an estimate of the degree of moisture damage.

Immersion Compression Test, AASHTO T 165 and ASTM D 1075

The immersion compression test (AASHTO T 165 and ASTM D 1075) was widely used in the 1990s (AASHTO 2002d; ASTM 2006g). It is based on the measurement of compressive strength of compacted asphalt mix samples. Six samples 100 mm (4 in) diameter by 100 mm (4 in) height are prepared to a target air void content of about 6 percent. The samples are divided in two groups, one is the control or unconditioned subset, and the other is the conditioned subset. The conditioning consists of submerging the samples in a hot water bath at 60 °C (140 °F) for 24 h and then transferring the samples to a water bath at 25 °C (77 °F) for an additional 2 h. An alternative conditioning procedure is to submerge the samples in water at 49 °C (120 °F) for four days before transferring the samples to the water bath at 25 °C (77 °F).

A compressive test at 25 °C (77 °F) is performed on all the samples until failure. The compressive strength is calculated and the retained strength index estimated as the ratio of the conditioned to unconditioned compressive strength results. A retained strength above 0.75 is required for acceptability. The decline in use of this test was because in some cases the retained ratios values were close to 1.0 although stripping was evident in the samples (Hicks 1991). This could be due to the insensitivity of the compression test to measure the effects of moisture damage.

Hamburg Wheel Tracking Device, Tex 242-F

The Hamburg wheel tracking device (Tex 242-F), which was developed in the 1970s in Hamburg, Germany, has been widely studied and used in Colorado and Texas (Solaimanian et al. 2003; TxDOT 2004b). It measures the effects of rutting and moisture damage by rolling back and forth a steel wheel that applies a load of about 700 N (158 lb) to a set of samples that are submerged in a 50 °C (122 °F) water bath. The size of the sample is 150 mm (6 in) in diameter by 60 mm (2.4 in) height, and the rate of load application is about 50 passes per minute. When 20,000 wheel passes or when a permanent deformation of 20 mm (0.8 in) occurs in the samples, the test stops. Moisture sensitivity is assessed by measuring the number of passes to failure (if

less than 20,000 passes are required to achieve the 20 mm deformation) and the final rut depth in the asphalt sample. Initially, beam-like samples were used for this test, but the rise in the use of the SGC changed the requirement to two cylindrical samples in series. A cut of about 16 mm (0.6 in) is made on the samples before placing them inside the testing molds.

Environmental Conditioning System (ECS)

The Environmental Conditioning System was developed as part of an extensive study on the mechanisms of moisture damage (Alam et al. 1998b; Terrel and Al-Swailmi 1994). It determines the moisture susceptibility of compacted asphalt mixes that are subjected to different temperatures, moisture saturation levels, and dynamic loading. The samples 100 mm (4 in) diameter by 100 mm (4 in) height are prepared in the SGC and compacted to a target air void content of 7.5 ± 0.5 percent.

The air permeability and resilient modulus are determined on the samples in a dry condition by applying air under vacuum through the sample and a haversine load of 0.1 s with a rest period of 0.9 s. Then, the sample is saturated with water under vacuum and its permeability is determined. The sample is then subjected to a haversine dynamic loading of 900 N (200 lb) at a temperature of 60 °C (140 °F) for 6 h and then cooled down to room temperature for an additional 2 h. The resilient modulus is measured again and the process (heating, loading, and cooling) is repeated two additional times. The ratio of the conditioned to unconditioned resilient modulus or modulus ratio (MR) is calculated and prescribed to be above 0.7 for a mix to be considered acceptable.

This system was developed to simulate the effect of traffic loading and pore pressure. After its initial development, studies were performed to solve some of its deficiencies, like heating the water used for saturation and avoiding confinement during vacuum saturation (Alam et al. 1998a; 1998b; Tandon and Nazarian 2001). Some changes were recommended in the process including confinement with a rubber membrane during conditioning and testing, and applying a static immersion for 5 min and then circulating water at room temperature through the sample for 1 h before measuring the reference resilient modulus. Also, after the sample is conditioned and loaded at elevated temperatures for 6 h, the circumference of the sample is measured and if it increases by more than 2 percent, the sample is considered moisture susceptible. If not, the conditioning processes and resilient modulus measurement proceed as previously explained. In this revised methodology, the threshold for MR is set to 0.8.

Surface Energy Measurements and Analysis

The lack of a unified laboratory test method to estimate moisture damage and the shortcomings and lack of correlation with field performance of the majority of the traditional test methods motivated researchers to approach and assess moisture damage in a more fundamental way. Some of these studies have focused on measuring the surface energies of different asphalt binders and aggregates.

The surface energies have been used to compute the adhesive bond energy of the asphalt binder and the aggregate and the cohesive bond energy of the asphalt binder (Bhasin et al. 2006; Cheng 2002; Cheng et al. 2002; Elphingstone 1997; Hefer 2004; Lytton et al. 2005; Zollinger 2005). The results provide information about the ability of the asphalt binder to resist water and the best potential asphalt binder and aggregate combinations to resist moisture damage and serve as a preliminary screening for material selection. Several techniques are used to measure the surface energy components of the asphalt binder and the aggregates, such as the Wilhelmy plate (WP), the Universal Sorption Device (USD), the sessile drop, inverse gas chromatography, and the microcalorimeter, among others. The results obtained from these tests are used to approximate the adhesive bond energy between the asphalt binder and the aggregate with and without the presence of water (Equations 2.5 and 2.8). A brief explanation of the WP and USD methodologies and calculations is provided in the following sections.

Wilhelmy Plate (WP)

The WP technique, which is based on equilibrium of kinetic forces, uses 50 mm (2 in) length by 25 mm (1 in) deep by 0.15 mm (0.006 in) wide glass slides coated with asphalt binder that are suspended from a highly accurate balance. The glass slides are cleaned thoroughly before coating. The dynamic contact angle analyzer, the commercial equipment to measure surface energy, is presented in Figure 2.11.

Figure 2.11. Dynamic contact angle analyzer equipment and data acquisition system (left) and sample inside chamber during testing (right)

During testing, the thin glass slide, uniformly coated with asphalt binder, is immersed and then withdrawn at a very slow and constant speed from a container filled with a solvent of known properties (Figure 2.12). The contact angle between the asphalt binder and the solvent measured during the immersion process is called the advancing contact angle and is associated with healing, while the contact angle measured during the withdrawal process is labeled the receding contact angle and is usually associated with fracture.
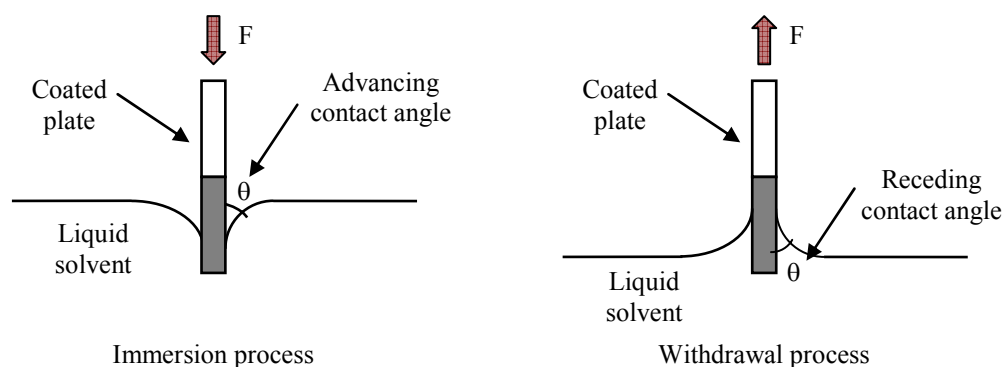
Figure 2.12. Schematic of the Wilhelmy plate method

The contact angles are estimated by measuring the force (represented by F in Figure 2.12) when the plate is suspended in air and when it is immersed and withdrawn from the fluid. The difference in the two force values, ΔF, is expressed as:

$$\Delta F = P_t \gamma_L \cos\theta - V_{im}\left(\rho_L - \rho_{air}\right)g \tag{2.11}$$

where P_t is the perimeter of the coated plate, γ_L is the surface energy of the liquid, θ is the contact angle between the asphalt and the liquid, V_{im} is the volume of the immersed plate, ρ_L is the density of the liquid, ρ_{air} is the density of air, and g is the acceleration due to gravity. Then, the value of the contact angles can be estimated as follows:

$$\cos\theta = \left(\frac{\Delta F + V_{im}\left(\rho_L - \rho_{air}\right)g}{P_t\gamma_L}\right) \tag{2.12}$$

After the values of the contact angles are estimated, the Young-Dupree equation is used to estimate the surface energy components. The Young-Dupree equation is based on Young's equation that describes the surface tension using the contact angle formed when a drop of liquid rests on top of a solid surface. As shown in Figure 2.13, θ is the contact angle between the solid and the liquid and γ_{LV}, γ_{SV}, and γ_{SL} represent the surface energy of the liquid-vapor, solid-vapor, and solid-liquid interfaces, respectively.
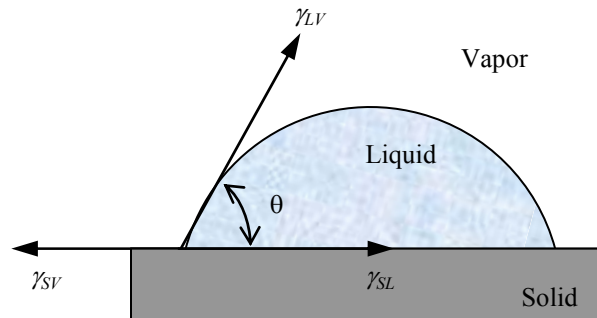
Figure 2.13. Schematic of the three-phase boundary of a liquid drop on top of a solid surface in the presence of vapor

Therefore, the equilibrium of forces presented in Figure 2.13 gives Young's equation:

$$\gamma_{SV} = \gamma_{SL} + \gamma_{LV}\cos\theta \tag{2.13}$$

When θ is small, the solid is considered hydrophilic, and the drop of liquid will tend to spread over the solid. On the other hand, when θ is large, even greater than 90°, the liquid is not likely to spread over the surface of the solid and thus the solid is considered hydrophobic.

Combining the work of adhesion expressed in Equation 2.2 and Young's equation (Equation 2.13), the Young-Dupree equation is obtained (Hefer 2004):

$$W_{LS}^{a} = \gamma_L \left(1 + \cos\theta\right) \tag{2.14}$$

Substituting equations 2.5 through 2.7:

$$\gamma_L \left(1 + \cos\theta\right) = 2\left(\sqrt{\gamma_L^{LW}\gamma_S^{LW}} + \sqrt{\gamma_L^{+}\gamma_S^{-}} + \sqrt{\gamma_L^{-}\gamma_S^{+}}\right) \tag{2.15}$$

By measuring the contact angle between the asphalt-coated plates and at least three different liquids or solvents with known surface energy components, Equation 2.15 can be solved as a system of three equations with three unknowns (γ_S^{LW}, γ_S^{-}, and γ_S^{+}). Commonly used solvents are water, formamide, glycerol, ethylene glycol, or diiodomethane. The system of linear equations is defined as follows:

$$\begin{bmatrix} y_1 \\ y_2 \\ y_3 \end{bmatrix} = \begin{bmatrix} a_{11} & a_{12} & a_{13} \\ a_{21} & a_{22} & a_{23} \\ a_{31} & a_{32} & a_{33} \end{bmatrix} \begin{bmatrix} x_1 \\ x_2 \\ x_3 \end{bmatrix} \tag{2.16}$$

$$a_{1i} = \frac{2\sqrt{\gamma_{Li}^{LW}}}{\gamma_{Li}} \tag{2.17}$$

$$a_{2i} = \frac{2\sqrt{\gamma_{Li}^{+}}}{\gamma_{Li}} \tag{2.18}$$

$$a_{3i} = \frac{2\sqrt{\gamma_{Li}^{-}}}{\gamma_{Li}} \tag{2.19}$$

$$x_1 = \sqrt{\gamma_S^{LW}} \tag{2.20}$$

$$x_2 = \sqrt{\gamma_S^{-}} \tag{2.21}$$

$$x_3 = \sqrt{\gamma_S^{+}} \tag{2.22}$$

$$y_i = 1 + \cos\left(\theta_i\right) \tag{2.23}$$

The advancing and receding angles are used in Equation 2.23 to estimate the corresponding surface energy components. The total surface energy of the asphalt binder is computed based on Equation 2.3 as follows:

$$\gamma_S = \gamma_S^{LW} + 2\sqrt{\gamma_S^{+}\gamma_S^{-}} \tag{2.24}$$

Universal Sorption Device (USD)

The USD is used to estimate the surface energy of the aggregates. It is based on a static vapor sorption technique and relies on a sorption isotherm to estimate the amount of vapor adsorbed on the surface of the material. The isotherm is estimated using a gravimetric method, by measuring the amount of vapor that is adsorbed on the surface of the solid while subjected to a vacuum. The advantage of this system is that it can be used on aggregates of different sizes, shapes, mineralogy, and surface textures.

A clean aggregate sample in the size range between the no. 4 (4.75 mm) sieve and no. 8 (2.36 mm) sieve is introduced in an open container and suspended inside the testing chamber. The chamber is closed and subjected to a vacuum, and then a probe vapor is injected into the chamber until a predetermined vapor pressure is reached. Using a highly sensitive magnetic balance the amount of probe vapor that is adsorbed on the surface of the aggregate is determined. Once the absorption level reaches equilibrium, an additional amount of probe vapor is added until the next predetermined value of vapor pressure is achieved. This process is repeated 8 to 10 times. The isotherm is built using the mass adsorbed at each probe vapor pressure level versus relative pressure. The test is conducted at 25 °C (77 °F).

The Brunauer, Emmett, and Teller (BET) model is used to estimate the specific surface area of the aggregate sample using the saturated vapor pressure of the solute, the amount adsorbed on the surface of the solid, and the properties of the solvent. Then, the Gibbs equation is used to calculate the spreading pressure at saturation vapor pressure as follows:

$$\pi_e = \frac{RT}{A} \int_0^{P_o} \frac{n}{P} dP \qquad (2.25)$$

where R is the universal gas constant, T is the temperature, and A is the specific surface area calculated with the BET model. Then, using the work of adhesion between a solid and the probe vapor is expressed as:

$$W^a = \pi_e + 2\gamma_L \qquad (2.26)$$

where γ_L is the total surface energy of the vapor. Substituting the expression in Equations 2.14 and 2.15 presented previously, the following final expression is obtained:

$$\pi_e + 2\gamma_L = 2\left(\sqrt{\gamma_L^{LW} \gamma_S^{LW}} + \sqrt{\gamma_L^+ \gamma_S^-} + \sqrt{\gamma_L^- \gamma_S^+} \right) \qquad (2.27)$$

Three different probe vapors are required in order to calculate the surface energy properties of the aggregate sample, represented by the subscript S in the previous equation. Commonly used vapors are n-hexane, methyl propyl ketone (MPK), and distilled water. The values of π_e and the surface energy components of the n-hexane, the nonpolar probe vapor, are used to calculate the aggregate LW surface energy component:

$$\gamma_S^{LW} = \frac{(\pi_e + 2\gamma_L)}{\left(4\gamma_L^{LW}\right)} \tag{2.28}$$

The values of π_e and surface energy characteristics of the monopolar probe vapor MPK are used to calculate the acidic surface energy component of the aggregate:

$$\gamma_S^+ = \frac{\left(\pi_e + 2\gamma_L - 2\sqrt{\gamma_S^{LW}\gamma_L^{LW}}\right)^2}{4\gamma_L^-} \tag{2.29}$$

Then, the π_e and surface energy characteristics of water (the bipolar probe vapor) are used to determine the basic surface energy component for the aggregate:

$$\gamma_S^- = \frac{\left(\pi_e + 2\gamma_L - 2\sqrt{\gamma_S^{LW}\gamma_L^{LW}} - 2\sqrt{\gamma_S^+\gamma_L^-}\right)^2}{4\gamma_L^+} \tag{2.30}$$

Finally, the total surface energy of the aggregate is calculated using Equation 2.24.

Dynamic Mechanic Analyzer (DMA)

The DMA is a versatile piece of equipment that has been recently used to evaluate the properties of sand asphalt samples (a mix of the finer fraction of the aggregate and the asphalt binder) in terms of their moisture susceptibility (Kim et al. 2004; Lytton et al. 2005; Zollinger 2005). This rheometer, which consists of a test station with a temperature control system, a controller, and a data acquisition system, is used to measure the viscoelastic and fracture properties of the material. Cylindrical sand asphalt samples of 12 mm (0.5 in) diameter by 50 mm (2 in) height are glued to holders and mounted inside the temperature-controlled chamber set at 25 °C (77 °F). To evaluate the effect of moisture, several samples are subjected to a moisture conditioning procedure prior to testing. The samples are subjected to a sinusoidal torsional load at a prescribed level of either stress or strain. Based on the angle of twist and the sample geometry the shear modulus is calculated.

Moisture damage is measured in terms of the initial level of damage and rate of damage evolution in the samples by monitoring the dissipated pseudo strain energy (DPSE) and the pseudo stiffness (PS). A conditioned to unconditioned ratio of the shear modulus or dynamic modulus is also used as an indicator of moisture susceptibility. Researchers have obtained satisfactory results using the DMA that correlated well with asphalt binder surface energy values and asphalt mix field performance (Kim et al. 2004; Zollinger 2005). More details on DMA analysis methods and results are presented in Chapter VII.

CHAPTER III
MATERIAL PROPERTIES AND SAMPLE FABRICATION

Asphalt mix samples were prepared in the laboratory using the SGC. The aggregate used was a crushed river gravel from Victoria, Texas, and the asphalt binder used was a performance graded (PG) 76-22 produced in Corpus Christi, Texas. The WP and the USD were used to measure the surface energy of the asphalt binder and the aggregates, and the AIMS was used to study the form, texture, and angularity of the aggregates. The mix type used was a Superpave Type C mix with a nominal maximum aggregate size of 12.5 mm (0.5 in). The mix design and job mix formula were developed by the TxDOT for use in the construction of highway US 59 in the Yoakum District in Texas. A modified aggregate gradation was also used, and a mix design was performed in accordance with the Superpave requirements. Washed sieve analyses were conducted on both gradations to account for excess fines present in the aggregates. Half of the samples were moisture conditioned following the modified Lottman procedure without the freezing step (AASHTO 2002c).

The following sections provide details regarding the individual material properties and the asphalt mix properties. A description of the AIMS system and results obtained for the aggregate are reported first, followed by the surface energy measurements and bond energies calculations for both the asphalt binder and the aggregate. Then, descriptions of the experimental design variables, the original aggregate gradation and mix design, the modified aggregate gradation and mix design, and washed sieve analyses results are included. Next, the protocols of mix preparation are explained, followed by the measurement of air void content in the laboratory, the air void structure results using X-ray CT, and the sample trimming method. Details about the moisture conditioning procedure are presented at the end of this chapter.

Aggregate Imaging System (AIMS)

Researchers have developed an automated aggregate imaging system to characterize the form, texture, and angularity of aggregates (Al-Rousan et al. 2005; Chandan et al. 2004; Fletcher et al. 2002; Masad et al. 2005). Form refers to the overall shape of the particle, angularity measures the sharpness of the edges or corners of the particle, and texture relates to the smoothness or coarseness of the surface. The main components of the system are a camera, a frame, a tray, and two types of light systems. The camera sits on the frame and moves in the transverse direction

while the tray moves in the longitudinal direction. The light system consists of a tray backlight and a top light. The system was developed along with image analysis software. The software uses wavelet decomposition to analyze texture, and the analysis of angularity is a gradient-based method. The form analysis is done based on the proportions of the three dimensions of the aggregate particles. The main advantages of the system are that it accounts for the effect of color variation on the surface of the aggregate, it measures the form of the particle in all three dimensions, and it significantly reduces the noise associated with the image acquisition (Chandan et al. 2004).

The system can analyze both fine and coarse aggregates. During image capture, individual aggregates are placed on the tray at an equidistant length of 50 mm (2 in) in the transverse direction (x-axis) and 40 mm (1.6 in) in the longitudinal direction (y-axis). For the fine aggregates, the tray backlight system is used and only black-and-white images are captured, while for the coarse aggregates both black-and-white images using the tray backlight and gray-scale images using the top light system are acquired. The black-and-white images are used to determine the shape and angularity, while gray-scale images are used for the texture analysis.

During the gray-scale image scan, to determine the thickness of the aggregates, the camera is calibrated to a point and given an altitude of zero, then the camera moves to the aggregate location and focuses on its surface. The difference between the zero altitude and the altitude required to focus is considered the depth of the aggregate.

Measurements on the river gravel used in this project were performed using AIMS. The source aggregates were blended and sieved, and three different sizes were selected for analysis: 9.5 mm (0.38 in), 6.35 mm (0.25 in), and 4.75 mm (0.19in or no. 4 sieve). The combined results yielded an angularity value of 3029.10, a texture value of 74.88, and a sphericity value of 0.68. Using a recently revised classification based on cluster analysis that ranks the three parameters on a low, medium, and high scale, the aggregate sphericity and angularity are considered medium and the texture is low (Masad et al. 2006c).

Surface Energy Measurements

The WP was used to measure the surface energy components of the PG 76-22 asphalt binder, and the USD was used to measure the surface energy components of the river gravel aggregate. The principles and operation of both systems were previously explained in Chapter II. The

results obtained for both materials are presented next, as well as the calculation of the cohesive and adhesive bond surface energies.

Wilhelmy Plate (WP)

A sample of the PG 76-22 asphalt binder was heated, and nine clean thin glass slides were coated uniformly by dipping them into the asphalt binder. The dimensions of the coated surface, including the thickness, were measured before testing using a precision caliper. The solvents used during testing were distilled water, formamide, and glycerol, which properties were obtained from previous reports and presented in Table 3.1 (Hefer 2004). According to the test procedure, the coated slide was immersed at a constant rate to a depth of about 5 mm (0.2 in) into the solvent and then withdrawn. Three replicate slides were used for each solvent. The test was performed at room temperature. The average advancing and receding contact angles for each solvent are presented in Table 3.2. Using Equations 2.15 through 2.23, the advancing or healing and receding or fracture components were estimated, as detailed in Appendix A. A summary of the asphalt binder (subscript b) components is presented in Table 3.3.

Table 3.1. Surface Energy Properties of the Solvents Used in the WP Test (After Cheng 2002)

Solvent	Γ_L (erg/cm^2)	Γ_L^{LW} (erg/cm^2)	Γ_L^{+} (erg/cm^2)	Γ_L^{-} (erg/cm^2)	Γ_L^{AB} (erg/cm^2)
Water	72.8	21.8	25.5	25.5	51.0
Glycerol	64.0	34.0	3.6	57.4	30.0
Formamide	58.0	39.0	2.3	39.6	19.0

Table 3.2. Contact Angles between the Asphalt Binder and the Solvents Measured in the WP Test

Solvent	Advancing contact angle (°)	Receding contact angle (°)
Water	97.97	62.18
Glycerol	84.21	44.64
Formamide	86.74	55.53

Table 3.3. Surface Energy Components of the Asphalt Binder

Component	Surface energy corresponding to the advancing angle (erg/cm^2)	Surface energy corresponding to the receding angle (erg/cm^2)
γ_b^{LW}	64.52	160.85
γ_b^{-}	0.18	0.05
γ_b^{+}	0.02	0.37
γ_b^{AB}	0.12	0.28
γ_b	64.64	161.13

Universal Sorption Device (USD)

A blend of aggregates consisting of 18.2 percent type C rock, 57.6 percent type D/F rock, 10.1 percent manufactured sand, and 14.1 percent limestone screenings was prepared and sieved. The sample used in the USD consisted of material smaller than 4.75 mm (passing the no. 4 sieve) and larger than 2.36 mm (retained on the no. 8 sieve). In preparation for the test, the sample was washed with distilled water and other solvents, dried, and desiccated. Then, a replicate of about 20 g (0.04 lb) was placed inside a fine-screen aluminum sample holder 27 mm (1.06 in) in diameter and 55 mm (2.16 in) in height. The sample holder containing the aggregates was suspended from the magnetic balance, and the chamber was closed. Degassing under vacuum then started, followed by the injection of the first probe vapor as described in Chapter II. When the test procedure using the first probe vapor was complete, the sample was removed from the chamber, washed, and the same steps previously described were repeated in order to prepare it for the next probe vapor. Three types of probe vapors were used: nonpolar, monopolar, and bipolar vapors corresponding to n-hexane, MPK, and water, respectively. The surface energy components of these vapors are presented in Table 3.4. Using Equations 2.24, 2.25, and 2.28 through 2.30, the surface energy components of the aggregate (subscript *a*) were computed. The results are presented in Table 3.5.

Table 3.4. Surface Energy Properties of the Solvents Used in the USD Test (After Cheng 2002)

Probe vapor	Γ_L (erg/cm^2)	Γ_L^{LW} (erg/cm^2)	Γ_L^{+} (erg/cm^2)	Γ_L^{-} (erg/cm^2)	Γ_L^{AB} (erg/cm^2)
n-hexane	18.4	18.4	0.0	0.0	0.0
MPK	24.7	24.7	0.0	19.6	0.0
Water	72.8	21.8	25.5	25.5	51.0

Table 3.5. Surface Energy Components of the Aggregate

Component	Surface energy (erg/cm^2)
γ_a^{LW}	84.34
γ_a^-	1.10
γ_a^+	426.85
γ_a^{AB}	43.31
γ_a	124.65

Bond Energy

Using the measurements acquired with the WP, the cohesive bond surface energy of the asphalt binder was computed using Equation 2.4. Equations 2.6 and 2.7 were used to estimate the *LW* and *AB* components with $i = j =$ asphalt binder (subscript *b*):

$$\Delta G_b^{cLW} = -2\gamma_b^{LW} \tag{3.1}$$

$$\Delta G_b^{cAB} = -2\gamma_b^{AB} = -4\sqrt{\gamma_b^+ \gamma_b^-} \tag{3.2}$$

The results are presented in Table 3.6.

Table 3.6. Cohesive Bond Surface Energy for the Asphalt Binder

Component	Cohesive bond surface energy corresponding to the advancing angle (erg/cm^2)	Cohesive bond surface energy corresponding to the receding angle (erg/cm^2)
$-\Delta G_b^{cLW}$	129.03	321.70
$-\Delta G_b^{cAB}$	0.25	0.56
$-\Delta G_b^c$	129.28	322.26

The adhesive bond energy between the asphalt binder and the aggregate was calculated using Equations 2.5 through 2.7 with $i =$ binder (subscript *b*) and $j =$ aggregate (subscript *a*). The advancing angle results were used to estimate the healing component, and the receding angle results were utilized to calculate the fracture component. Results are presented in Table 3.7. Large values of cohesive and adhesive bond energies represent a better ability to resist fracture and to heal.

Table 3.7. Adhesive Bond Energy between the Asphalt Binder and the Aggregate

Component	Adhesive bond energy corresponding to the advancing angle (erg/cm²)	Adhesive bond energy corresponding to the receding angle (erg/cm²)
$-\Delta G_{ba}^{aLW}$	144.88	228.77
$-\Delta G_{ba}^{aAB}$	6.90	25.48
$-\Delta G_{ba}^{a}$	151.78	254.24

The adhesive bond energy in the presence of water was also estimated using Equation 2.8 with i = binder (subscript b), j = aggregate (subscript a), and k = water (subscript w). The expanded form of Equation 2.8 is (Hefer 2004):

$$\Delta G_{bwa}^{a} = 2\left[\begin{array}{l} -\sqrt{\gamma_b^{LW}\gamma_w^{LW}} + \sqrt{\gamma_a^{LW}\gamma_w^{LW}} - \sqrt{\gamma_b^{LW}\gamma_a^{LW}} - \gamma_w^{LW} \\ + \sqrt{\gamma_w^{+}}\left(\sqrt{\gamma_b^{-}} + \sqrt{\gamma_a^{-}} - \sqrt{\gamma_w^{-}}\right) \\ + \sqrt{\gamma_w^{-}}\left(\sqrt{\gamma_b^{+}} + \sqrt{\gamma_a^{+}} - \sqrt{\gamma_w^{+}}\right) \\ - \sqrt{\gamma_b^{+}\gamma_a^{-}} - \sqrt{\gamma_b^{-}\gamma_a^{+}} \end{array}\right] \qquad (3.3)$$

The components of the adhesive bond energy in the presence of water are reported in Table 3.8. The total adhesive bond energy in Table 3.8 has a negative value, which corroborates that water has a greater affinity for the aggregate surface compared to the asphalt binder and that there is a driving force that tends to separate the two materials in the presence of water.

Table 3.8. Adhesive Bond Surface Energy between the Asphalt Binder and the Aggregate in the Presence of Water

Component	Adhesive bond surface energy corresponding to the advancing angle (erg/cm²)	Adhesive bond surface energy corresponding to the receding angle (erg/cm²)
$-\Delta G_{bwa}^{aLW}$	29.26	69.72
$-\Delta G_{bwa}^{aAB}$	-116.10	-100.22
$-\Delta G_{bwa}^{a}$	-86.84	-30.51

Experimental Design

The objective of the experimental design was to prepare a number of unconditioned and conditioned asphalt mix samples with different air void structures. To create different air void structures, two aggregate gradations (*A* and *B*) and mix designs were considered as described in the next section. Also, for one of the aggregate gradations two angles of compaction (1.25° and 2.5°) were used. The SGC was employed to compact cylindrical samples 150 mm in diameter by 165 mm in height. The samples of gradation *A* were initially cored and trimmed slightly from the top and bottom to a size of 100 mm (4 in) in diameter by 150 mm (6 in) in height. As will be explained in a subsequent section, based on the results of an initial X-ray CT image analysis it was decided to trim all samples further at different locations (centered trimmed and skewed trimmed) to a final height of 100 mm (4 in) in order to increase the difference between the air void structures.

Twelve samples were prepared for each gradation and trimming method in order to provide three replicates for each mechanical test to be performed. Half of the samples were moisture conditioned using the modified Lottman conditioning procedure without the freezing step. The experimental design variables and the sample labels used throughout this study are presented in Table 3.9. The conditioned samples are identified with the acronym *MC* following the sample label.

Table 3.9. Experimental Design Variables

Gradation	Sample label	Trimming	Moisture conditioning
A	*A1*	Centered	No
	A1-MC	Centered	Yes
	A2	Skewed	No
	A2-MC	Skewed	Yes
B	*B1*	Centered	No
	B1-MC	Centered	Yes
	B2	Skewed	No
	B2-MC	Skewed	Yes

The next sections provide details about the aggregate gradations and the mixing and compaction procedures. Then, the air void measurements on the asphalt mixes and details on the

air void structure using X-ray CT image analysis results are presented. Information about the moisture conditioning procedure is included at the end of this chapter.

Aggregate Gradations and Mix Design

The original aggregate gradation or gradation *A* and corresponding mix design were developed by the TxDOT and used in the construction of highway US 59 in Yoakum, Texas. The aggregate blend consisted of 18 percent type C rock, 57 percent type D/F rock, 10 percent manufactured sand, 14 percent limestone screenings, and 1 percent lime. The original gradation and proportions of each material provided by the TxDOT are presented in Table 3.10. To prepare the samples in the laboratory, aggregate materials from the same source were used. The aggregates in stockpile condition were damp and covered with dust. Therefore, the aggregates were combined according to the percentages prescribed by the TxDOT and allowed to dry by filling shallow flat trays and placing them overnight inside an oven at 110 °C (230 °F).

Table 3.10. Original Aggregate Gradation Developed by the TxDOT

Sieve size (mm)	Type C		Type D/F		Sand		Limestone		Lime		Σ Total (%)
	Pass (%)	Total (%)	Pass (%)	Total (%)	Pass (%)	Total (%)	Pass (%)	Total (%)	Pass (%)	Total (%)	
19	100	18.0	100	57.0	100	10.0	100	14.0	100	1.0	100.0
12.5	70	12.6	100	57.0	100	10.0	100	14.0	100	1.0	94.6
9.5	10	1.8	95	54.2	100	10.0	100	14.0	100	1.0	81.0
4.75	5	0.9	50	28.5	100	10.0	100	14.0	100	1.0	54.4
2.36	3	0.5	15	8.6	99	9.9	92	12.9	100	1.0	32.9
1.18	2.5	0.5	5	2.9	79	7.9	72	10.1	100	1.0	22.3
0.6	2	0.4	4	2.3	49	4.9	54	7.6	100	1.0	16.1
0.3	1.5	0.3	3	1.7	23	2.3	41	5.7	100	1.0	11.0
0.15	1	0.2	2	1.1	7	0.7	33	4.6	100	1.0	7.6
0.075	0.5	0.1	1	0.6	3	0.3	25	3.5	100	1.0	5.5

After drying, a washed sieve analysis was performed on the original gradation to account for any excess of fines coating the aggregates. The washed sieve analysis, following ASTM C 117, was performed on the combined gradation (last column of Table 3.10) (ASTM 2006d). A 5000 g (11 lb) sample was prepared and placed in a container large enough to permit vigorous agitation without loss of material. The sample was covered with water and agitated in order to

separate and bring into suspension all of the fine particles. Then, the water was poured over a pair of nested sieves, the bottom one having an opening size of 75 μm (no. 200 sieve) and the top one with an opening size of 1.18 mm (no. 16 sieve). The container was again filled up with water and the process repeated until the water after agitating the sample inside the container appeared clear. The material retained in the sieves was returned to the washed sample and then dried overnight at 110 °C (230 °F). After drying, the sample weight was measured and then the material sieved again. The results obtained were compared against the target gradation, and the differences were computed.

The washed sieve analysis is an iterative process; once the first results are obtained, the aggregate gradation is modified so that the differences between the target or original gradation and the washed gradation are minimized. A new batch is prepared and the washed sieve analysis process repeated until the differences between the target gradation and the gradation obtained after the washed sieve analysis are minimized. The tolerances are 1 percent for particle sizes larger than 4.75 mm (no. 4 sieve), 0.5 percent for particles between 4.75 mm (no. 4 sieve) and 0.15 mm (no. 100 sieve), and 0.3 percent for particle sizes smaller than 0.15 mm (no. 100 sieve). The results of the iterative washed sieve analysis procedure, which are presented in the last column of Table 3.11, are the actual values used to prepare the aggregate batches. Details of the asphalt mix preparation are provided in the next section.

Table 3.11. Aggregate Gradation *A*

Sieve Size (mm)	Original			Washed		
	Cumulative Passing (%)	Cumulative Retained (%)	Individual Retained (%)	Cumulative Passing (%)	Cumulative Retained (%)	Individual Retained (%)
19	100.0	0.0	0.0	100.0	0.0	0.0
12.5	94.6	5.4	5.4	94.6	5.4	5.4
9.5	81.0	19.1	13.7	82.0	18.1	12.7
4.75	54.4	45.6	26.6	52.5	47.5	29.5
2.36	32.9	67.1	21.5	31.0	69.0	21.5
1.18	22.3	77.7	10.6	20.4	79.6	10.6
0.6	16.1	83.9	6.2	13.2	86.8	7.2
0.3	11.0	89.0	5.1	8.1	91.9	5.1
0.15	7.6	92.4	3.4	4.7	95.3	3.4
0.075	5.5	94.5	2.2	2.6	97.4	2.2

In an effort to induce different air void structures in the samples, a different aggregate gradation was introduced by modifying the one previously described. The modified gradation was labeled gradation *B* as shown in Table 3.9. The intention was to obtain a coarser gradation without changing the aggregate, asphalt binder type, or nominal maximum aggregate size. A washed sieve analysis was also performed on the modified gradation, and the results are presented in Table 3.12. The mix design for gradation *B* was done according to Superpave requirements (AASHTO 2003c, d). The details of the mix design procedure and comparison against the Superpave standards are presented in Appendix B. The final parameters for both mix designs are presented in Table 3.13. The plot of both gradations *A* (original gradation) and *B* (modified gradation) along with the Superpave aggregate requirements for a 12.5 nominal maximum aggregate size mix are presented in Figure 3.1.

Table 3.12. Aggregate Gradation *B*

	Modified			Washed		
Sieve Size (mm)	Cumulative Passing (%)	Cumulative Retained (%)	Individual Retained (%)	Cumulative Passing (%)	Cumulative Retained (%)	Individual Retained (%)
19	100.0	0.0	0.0	100.0	0.0	0.0
12.5	90.0	10.0	10.0	90.0	10.0	10.0
9.5	75.0	25.0	15.0	76.2	23.8	13.8
4.75	48.4	51.6	26.6	45.6	54.4	30.6
2.36	28.0	72.0	20.4	27.6	72.4	18.0
1.18	17.3	82.7	10.7	16.0	84.0	11.6
0.6	11.0	89.0	6.3	9.7	90.3	6.3
0.3	7.5	92.5	3.5	5.5	94.5	4.2
0.15	5.7	94.3	1.8	3.5	96.5	2.0
0.075	4.0	96.0	1.7	2.0	98.0	1.5

Table 3.13. Mix Design Parameters and Superpave Requirements

Parameter	Gradation *A*	Gradation *B*	Superpave Criteria
Design binder content by weight of mix	5.3	6.1	–
Percent voids in the mineral aggregate (*VMA*)	15.9	16.9	Minimum 14
Percent voids filled with asphalt (*VFA*)	74.9	75.8	65 to 78
Dust-to-binder ratio	1.0	0.7	0.6 to 1.2
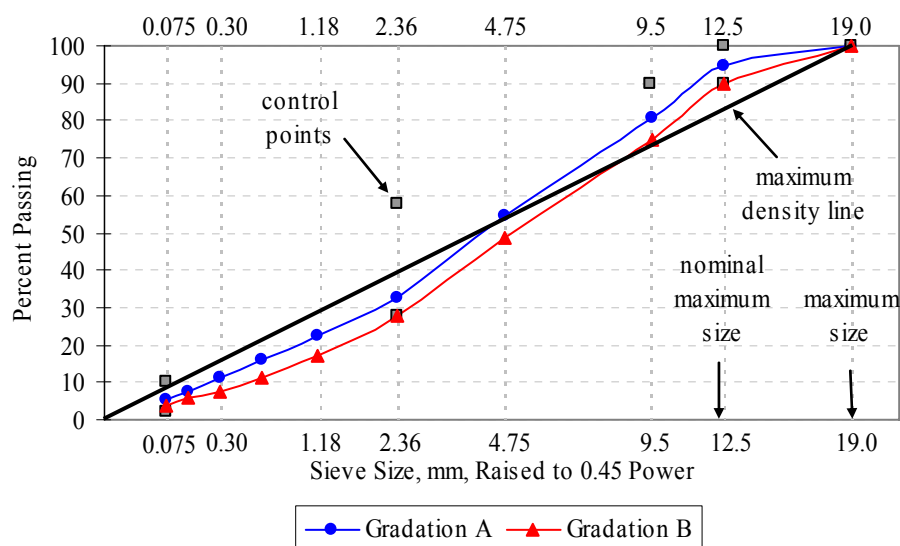
Figure 3.1. Aggregate gradations

Mix Preparation

Asphalt mix samples were prepared according to AASHTO standards (AASHTO 2002a). The mixing and compaction temperatures were obtained from the TxDOT test procedure standards based on the asphalt binder type (TxDOT 2005). The mixing temperature used was 163 °C (325 °F), and the compaction temperature was 149 °C (300 °F). Before compaction, the samples were short-term oven aged for 2 h at 135 °C (275 °F) according to the AASHTO standard (AASHTO 2003b). The conditioning time was only 2 h (instead of the 4 h prescribed by the standard) because more than the recommended 30 min was required to bring the asphalt mix to the compaction temperature after short-term aging. Therefore, a reduced short-term aging time was utilized to compensate for the additional heating time at a higher compaction temperature. The mixing and compaction steps are described in Table 3.14.

The SGC was used to compact cylindrical samples of 150 mm (6 in) diameter by 165 mm (6.5 in). Compaction angles of 1.25° and 2.5° were used in preparing the samples of gradation *A*, while only one angle of 1.25° was used in preparing the samples of gradation *B*. The samples of gradation *A* were initially cored and trimmed slightly from the top and bottom to a size of 100 mm (4 in) in diameter by 150 mm (6 in) in height. A circular diamond bit and a double blade diamond saw with a water cooling system were used to core and trim the samples. The target percent air voids for the gradation *A* 150 mm (6 in) height samples was 7 ± 0.5

percent. As will be detailed in the next section, the samples were further trimmed to 100 mm (4 in) height to increase the differences in air void distributions, which reduced their total air void content to around 5.8 percent. The samples of gradation *B* were cored and trimmed following the same trimming methodology developed for gradation *A* to a size of 100 mm (4 in) diameter and 100 mm (4 in) height. The target percent air voids for the gradation *B* 100 mm (4 in) height samples was 7 ± 0.5 percent.

Table 3.14. Mixing and Compaction Procedures Used to Prepare the Asphalt Mix Samples

Step	Action
1	Prepare aggregate batches according to the washed sieve analysis (last column of Tables 4.11. and 4.12) and adding 1 percent of lime. Prepare one batch per sample and use a different container for every batch.
2	Heat the aggregate batches overnight at the mixing temperature.
3	Heat the asphalt binder for 1 h at the mixing temperature.
4	Remove the aggregate batch from the oven and pour it inside the mixing container.
5	Place the mixing container on top if a scale, tare the scale, and pour the amount of heated asphalt binder specified by the mix design.
6	Place the mixing container in the mechanical mixer and mix the aggregates and asphalt binder until the aggregates are completely and uniformly coated.
7	Pour and spread the asphalt mix in flat shallow trays and place then inside an oven at the short-term oven aging temperature for 2 h.
8	Stir the asphalt mix while aging after 1 h to assure uniform aging.
9	After the short-term aging, heat the asphalt mix to the compaction temperature for 1 h along with the compaction mold and other compaction tools.
10	Remove the asphalt mix from the oven and measure the required amount to achieve the target percent air voids.
11	Remove the compaction mold from the oven and place a paper disk over the base plate of the mold.
12	Pour the mix in the mold in one lift without causing segregation.
13	Level the mix and place another paper disk on top.
14	Load the mold into the SGC.
15	Compact at a pressure of 600 kPa and specified compaction angle until the target height is achieved.
16	Remove the mold from the SGC and extrude the sample from the mold. [a]
17	Remove the paper disks from the top and bottom of the sample.
18	Return the mold to the oven if more samples are to be compacted. [b]

[a] It is recommended to leave the mold to cool down for some time or to use a poly vinyl chloride (PVC) pipe of the same diameter of the sample to surround it during extrusion to prevent deformations or crumbling
[b] It is recommended to use at least two molds

To determine the amount of asphalt mix required to obtain the specified target percent air voids (step 10 in Table 3.14), trial samples using varying mix amounts were compacted, cored, and trimmed to the desired dimensions and the air voids measured as detailed in the next section.

Air Void Characterization

Laboratory Measurements

The percent air voids was measured in the laboratory using the Corelok® system (ASTM 2006f; InstroTek 2003b). The procedure, in which the samples are sealed in plastic bags and subjected to a vacuum, is considered more reliable and accurate than the traditional surface-dry method for open graded mixes. The system consists of a vacuum chamber and control panel, a water tank with a cushioned weighing basket affixed to a balance, plastic bags in different sizes, and other accessories. The steps to determine the bulk specific gravity and air void content of the samples are detailed in Table 3.15.

Table 3.15. Corelok® Procedure to Determine Bulk Specific Gravity and Air Void Content

Step	Action
1	Turn on the Corelok® equipment, select program 1 in the control panel, and input the following values: vacuum = 99, dwell = 15, and seal = 0.5.
2	Smooth the edges of the asphalt mix sample if necessary.
3	Insert the filler plates and rubber sliding plates with the rubber pads facing up inside the vacuum chamber, making sure that the seal bar can move freely up and down and there is about 5cm (1 in) gap between the seal bar and the filler plates.
4	Take a puncture and rip free Corelok® plastic bag, weigh it, and place it inside the chamber.
5	Weigh and record the asphalt mix sample weight.
6	Place the sample inside the bag, rest the bag on top of the rubber sliding plates, and center the plates in the chamber.
7	Close the Corelok® equipment lid and hold it firmly until vacuum starts.
8	When the lid opens, remove the sample from the equipment and check efficiency of the vacuum; the bag should be tightly fixed to the sample.
9	Submerge the bag with the sample in the water bath, placing it on top of the weighing basket; make sure the flaps of the bag are not touching the sides of the water bath.
10	Wait for the scale to stabilize and record the weight.
11	Remove the bag from the water bath and place it on top of a soft cloth.
12	Cut the plastic bag using a pair of scissors and remove the sample from the bag.
13	Weigh and record the asphalt mix sample weight. [a]

[a] if the sample weight is 5 g (0.01 lb) heavier than the original sample weight (step 5) a leak in the plastic bag occurred and the procedure needs to be repeated using a different sample

To calculate the bulk specific gravity and air void content, first the ratio of the dry sample weight to the bag weight is calculated and used to estimate a bag correction factor (InstroTek 2003b). Then, the total volume of the sample is estimated as follows:

$$V_T = W_{bag} + W_{final} - W_{submerged} \tag{3.4}$$

where W_{bag} is the bag weight, W_{final} is the dry sample weight after water submersion, and $W_{submerged}$ is the sealed sample weight in water. The volume of the bag (V_{bag}) is estimated as the ratio of the bag weight and the bag correction factor. The volume of the sample is computed as:

$$V_{sample} = V_T - V_{bag} \tag{3.5}$$

The bulk specific gravity (G_{mb}) is then calculated as:

$$G_{mb} = \frac{W_{initial}}{V_{sample}} \tag{3.6}$$

where $W_{initial}$ is the dry sample weight before sealing determined in step 5 (Table 3.15). Finally, the total air void content in the sample is estimated as follows (AASHTO 2002f):

$$\%AV = 100\left(1 - \frac{G_{mb}}{G_{mm}}\right) \tag{3.7}$$

where G_{mm} is the Rice or maximum specific gravity that was also determined using the Corelok® system (ASTM 2006a; InstroTek 2003b). The resulting value for gradation A was equal to $G_{mm} = 2.411$ g/cm^3 and $G_{mm} = 2.373$ g/cm^3 for gradation B. The bulk specific gravity and air void content for the replicate samples of gradations A and B are presented in Tables 3.16 and 3.17, respectively. Only three replicate samples were prepared for mix $B2\text{-}MC$.

Table 3.16. Bulk Specific Gravity and Total Air Void Content for the 150 mm (6 in) Height Gradation *A* Mix Replicates

Variable	Replicate	Mix type			
		A1	*A1-MC* [a]	*A2*	*A2-MC* [a]
Gmb	1	2.235	2.256	2.244	2.253
(g/cm^3)	2	2.255	2.256	2.253	2.257
	3	2.233	2.245	2.251	2.251
	4	2.246	2.250	2.231	2.236
	5	2.250	2.235	2.252	2.245
	6	2.236	2.236	2.248	2.249
%AV	1	7.3	6.5	6.9	6.5
	2	6.5	6.4	6.5	6.4
	3	7.4	6.9	6.6	6.6
	4	6.8	6.7	7.5	7.3
	5	6.7	7.3	6.6	6.9
	6	7.2	7.2	6.8	6.7

[a] The measurements were performed before moisture conditioning the samples

Table 3.17. Bulk Specific Gravity and Total Air Void Content for the 100 mm (4 in) Height Gradation *B* Mix Replicates

Variable	Replicate	Mix type			
		B1	*B1-MC* [a]	*B2*	*B2-MC* [a]
Gmb	1	2.210	2.200	2.203	2.209
(g/cm^3)	2	2.207	2.217	2.202	2.210
	3	2.209	2.220	2.213	2.211
	4	2.206	2.200	2.214	–
	5	2.211	2.213	2.216	–
	6	2.208	2.202	2.212	–
%AV	1	6.8	7.3	7.2	6.9
	2	7.0	6.6	7.2	6.9
	3	6.9	6.4	6.7	6.8
	4	7.0	7.3	6.7	–
	5	6.8	6.7	6.6	–
	6	6.9	7.2	6.8	–

[a] The measurements were performed before moisture conditioning the samples

Air Void Structure Using X-ray CT and Image Analysis Techniques

X-ray CT, a nondestructive technique used to visualize the interior characteristics of the asphalt mix samples, was used to study the air void structure of the asphalt mix samples. The X-ray CT system is described next, followed by an explanation of the image analysis used to determine the

air void content and size. Then, the air void structure and a description of the sample trimming procedure used to increase the differences in the air void structures are included.

System Description

The X-ray CT systems used for industrial applications are similar to the medical computerized axial tomography or CAT scanners, with the difference that the industrial scanners have a higher energy and resolution. Scanners have been grouped into four categories depending on their resolution capabilities: conventional, high-resolution, ultra-high-resolution, and microtomography (Ketcham and Carlson 2001). The two main components of a typical X-ray CT system are the X-ray source and the detector. There are different types of X-ray CT scanners, according to the geometry of the X-ray beam. Some of the most common are parallel beam, fan beam, and cone beam geometries. In parallel beam systems, a single ray and detector are used and translated across the length of the object and the process is repeated from a number of different angles. In fan beam systems, the X-ray source is collimated and a fan of rays is used to encompass the whole sample while a series of linear or arc detectors is used as shown in Figure 3.2. The source and detector can move around the object or the object can rotate and translate while the other components stay stationary, which is more common in industrial systems. In the case of the parallel and fan beam geometries, two-dimensional (2D) scans are generated and successive scans in the vertical direction are needed in order to describe the entire volume of the sample. In cone beam systems, a highly collimated coned-shaped X-ray source and grid of detectors are used. The rays usually encompass the whole sample width and height to directly output three-dimensional (3D) data. This method is faster but computationally expensive and generally yields images with lower resolution. Comprehensive information about different generations of X-ray CT systems, spatial resolution, data capture and analysis, and definition of terms can be found elsewhere (ASTM 2006c).
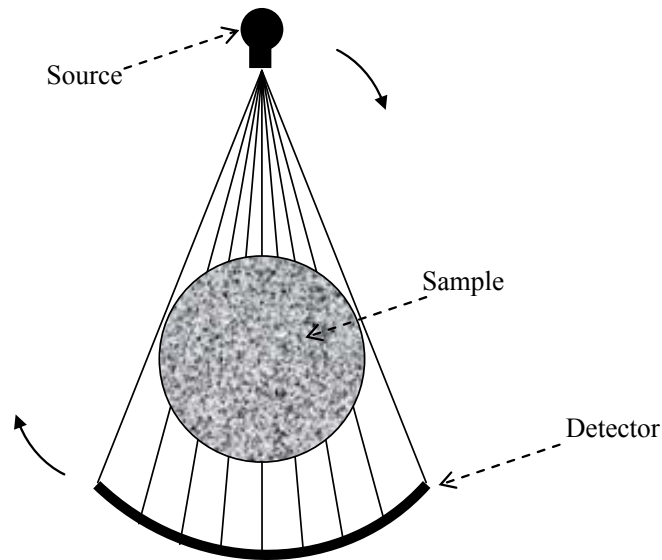
Figure 3.2. Schematic of the X-ray CT fan beam scan geometry (Adapted from Ketcham and Carlson 2001)

All X-ray CT systems are based on the measurement of intensities to estimate the density of the analyzed sample. As shown in Figure 3.2, during scanning, the sample is placed between the source and the detector and the X-ray source emits a beam of known intensity through the sample. Some of the X-rays pass through the sample, some get absorbed, and some others scatter. Based on the initial and measured attenuated X-ray intensities in the detector the density of the scanned material can be estimated as follows (Masad 2004):

$$I = I_o \exp \int_{ray} - \mu(x, y) ds \qquad (3.8)$$

where I is the intensity of the attenuated X-rays, I_o is the source intensity, $\mu(x,y)$ are the linear attenuation coefficients at any point in the sample, and ds is the differential length along the ray or line between the source and the detector. To generate enough equations and determine the values of the linear attenuation coefficients, multiple scans are done along the circumference of the sample. Then, based on the linear attenuation coefficients and using image reconstruction techniques, a full 2D image is rendered. The acquired X-ray CT images are often called slices because they show what would be observed if the sample was cut along the scan plane. When beam or fan beam geometries are used, the sample is moved a fixed gap in the vertical direction and the process repeated so images through the whole sample height are acquired. The quality of the resulting 2D image often depends on the sample size, source intensity, distance between the

sample and the source, noise, and artifacts. In order to reduce the occurrence of noise and artifacts a calibration sample, also called a wedge, is typically used to correct the beam hardening and ring artifact effects (Ketcham and Carlson 2001).

Image Analysis

A macro developed using the IPBasic capabilities of Image-Pro® Plus software was used to analyze the X-ray CT images (Al-Omari et al. 2002). The macro loads the images and converts them to black-and-white compositions based on a user-input threshold value between 0 and 256, which represents the levels of gray in the image. If the measured gray intensity is lower than the specified threshold, it is given a value of zero (black), and if it is above the specified threshold, it is given a value of 256 (white). In the threshold image, the black color represents the air voids while white represents the solids as shown in Figure 3.3. The appropriate user-input threshold value is obtained by matching the percent air voids obtained with the image analysis to the percent air voids measured in the laboratory.
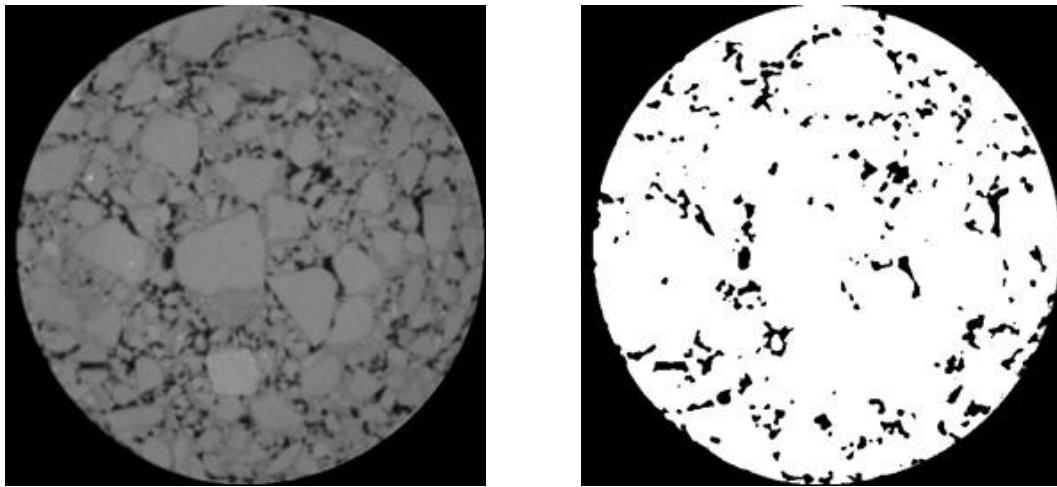
Figure 3.3. X-ray image threshold analysis showing the original grayscale image (left) and the black-and-white image after threshold (right)

The percent air voids for an image (*%AV$_i$*) and the total percent air voids of the sample (*%AV*) were computed as follows:

$$\%AV_i = \frac{A_{vi}}{A_{T_i}} \tag{3.9}$$

$$\%AV = \frac{\sum_{i=1}^{N} \%AV_i}{N} \tag{3.10}$$

where A_{vi} is the area of air voids in image i, A_{Ti} is the cross-sectional area of image i, and N is the total number of images. The air void radii in image i, also called air void size in this study, was computed as follows:

$$\bar{r}_i = \sqrt{\frac{A_{vi}}{\pi M_i}} \tag{3.11}$$

where M_i is the number of air voids in each image. Several threshold values are input to the macro until the total percent air voids of the sample (Equation 3.10) matches the laboratory measurements.

Researchers have used X-ray CT to characterize the internal structure of asphalt mixes and to describe the air void structure of field samples and laboratory samples prepared using the SGC or the linear kneading compactor (Al-Omari et al. 2002; Masad et al. 1999; Tashman et al. 2001; 2002). For the SGC samples, the plots of the air void content with respect to depth yield bathtub-shaped curves, with higher air void content at the top and bottom of the sample and lower and more uniform air void content in the middle section as shown in Figure 3.4a. On the other hand, the results for the field samples show different trends, but in general, the air void content is higher at the top of the sample and lower in the rest of the sample depth as shown in the schematic of Figure 3.4b.
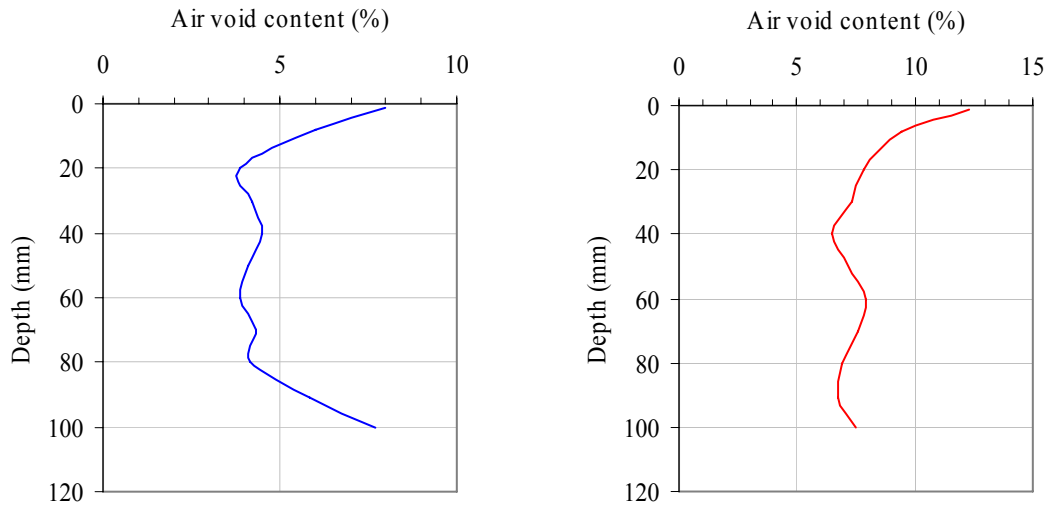
Figure 3.4. Schematic of air void structures in SGC samples (left) and field cores samples (right) (Adapted from Tashman et al. 2002)

Results

A high-resolution fan beam scanner with a maximum resolution of 100 μm, 512 detector channels, and a source X-ray intensity of 420kV was used to scan the asphalt mix samples. All scans and image processing were performed at the High Resolution X-ray CT Facility at the University of Texas at Austin. The sample setup and main components of the X-ray CT equipment are shown in Figure 3.5. During scanning, the sample was rotated 360° with respect to its center while the source and detector stayed stationary. A concrete core was used for calibration purposes, given its attenuation properties are similar to those of the asphalt mix samples that were analyzed. The vertical gap between slices was 1 mm (0.04 in). The output images were 16-bit, TIFF images, 512 by 512 pixels. Therefore, the size of the volume element bounded by the edges of the pixel and the thickness of the slice (also called voxel) size was about 0.195 mm (0.008 in) by 0.195 mm (0.008 in) by 1 mm (0.04 in).
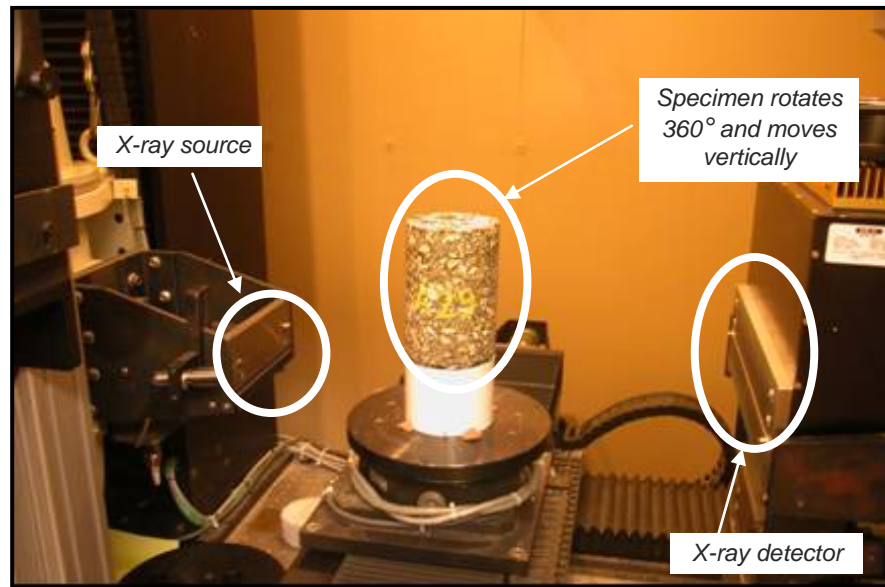
Figure 3.5. Sample setup during X-ray CT scanning

As previously mentioned, a macro developed using the IPBasic capabilities of Image-Pro® Plus software was used to analyze the X-ray CT images. Several threshold values were input to the macro until the average percent air voids of all images belonging to one sample (Equation 3.10) matched the laboratory measurements reported in Tables 3.16 and 3.17. The macro can estimate *%AV* including or excluding the air voids in contact with the sample edge. Since the Corelok® system was used to measure the air voids in the laboratory and a plastic bag surrounds the sample during the procedure, the air voids in contact with the sample edge were considered as part of the total percent air voids.

The results of the image analysis performed on six replicates of mix type *A1* and six replicates of mix type *A2* with a height of 150 mm (6 in) motivated further trimming of the samples. The change with depth of the air void content and the air void size are presented in Figures 3.6 and 3.7, where each curve represents the average of the six scanned replicates. Based on the results, it was apparent that the use of different compaction angles had almost no effect on the resulting air void structures.
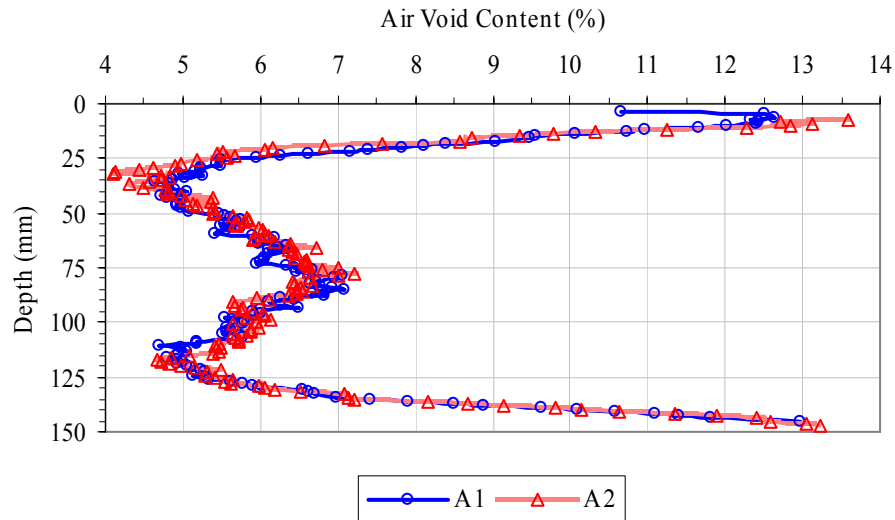
Figure 3.6. Air void content structure for the 150 mm (6 in) height *A1* and *A2* samples
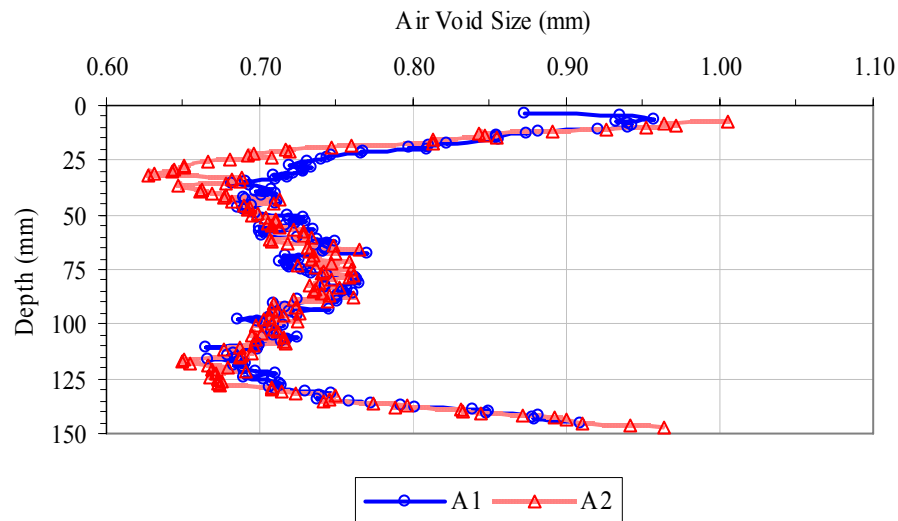
Figure 3.7. Air void size structure for the 150 mm (6 in) height *A1* and *A2* samples

Therefore, to increase the difference between the air void structures, the samples were further trimmed at different locations to a final height of 100 mm (4 in). Two primary considerations were taken into account when deciding on the location of the trimming. The first consideration was to achieve a uniform and nonuniform air void structure (similar to the one

observed in field cores). The second consideration was to have a comparable average percent air voids in both subsets (*A1* and *A2*) after trimming. Therefore, the replicates of mix *A1* were further trimmed an equal amount of 25 mm (1 in) from the top and the bottom (center trimmed) and the replicates of mix *A2* a smaller amount of 15 mm (0.6 in) from the top and a larger amount of 35 mm (1.4 in) from the bottom (skew trimmed). Based on the image analysis, the average air void content of the trimmed samples belonging to mix type *A1* was 5.7 percent and 5.9 percent for samples belonging to *A2* (Table 3.18).

The replicates of mix *B1* and *B2* were trimmed with this same methodology. From their original compacted size of 150 mm (6 in) diameter by 165 mm (6.5 in) height, mix *B1* samples were trimmed 32.5 mm (1.25 in) from top and bottom (center trimmed) and mix *B2* samples were trimmed 22.5 mm (0.85 in) from the top and 42.5 mm (1.65 in) from the bottom (skew trimmed). The target percent air voids for the gradation *B* 100 mm (4 in) height samples was 7 ± 0.5 percent. Therefore, the final dimensions for all replicates (gradation *A* and gradation *B*) were 100 mm (4 in) diameter by 100 mm (4 in) height. Two replicates of mix *B1* and two of mix *B2* were scanned. The air void structures for all mixes after trimming are presented in Figures 3.8 and 3.9.
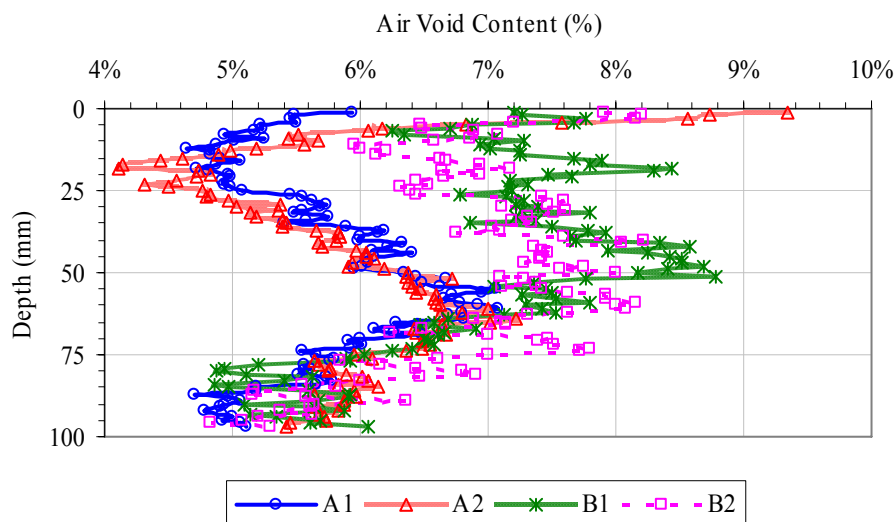
Figure 3.8. Air void content structure for the 100 mm (4 in) height samples
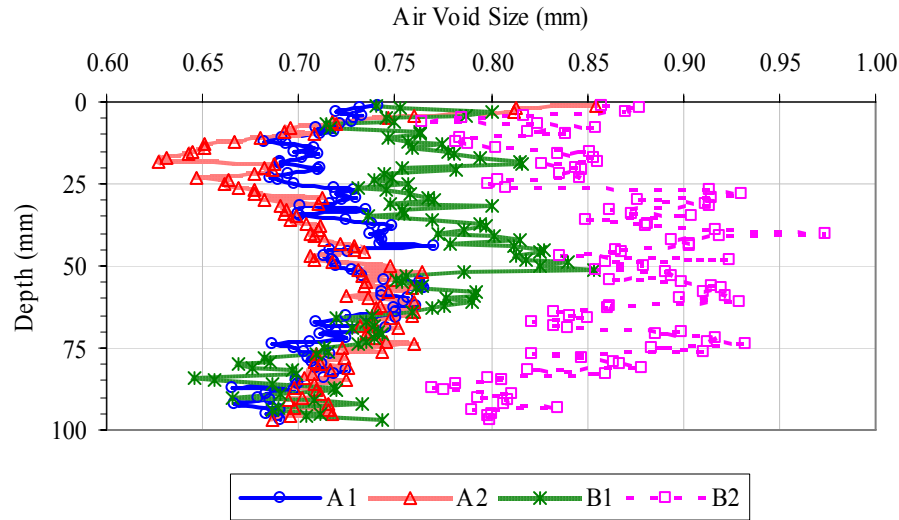
Figure 3.9. Air void size structure for the 100 mm (4 in) height samples

The relationship between air void content (*%AV$_i$* in Equation 3.9) and air void size ($\bar{r}_i$ in Equation 3.11) is presented in Figure 3.10. The values of these parameters obtained for each replicate are averaged to obtain the curve belonging to each mix type. This relationship is useful to observe the range of air void sizes (y-axis) and range of percent air voids (x-axis) through the depth of the sample. The minimum, maximum, and average values of that range are presented in Table 3.18. Mix *B2* has a the largest air void sizes (0.76 mm [0.031 in] to 0.97 mm [0.039 in]), whereas mix *A1* has the smallest range in terms of both percent and size (from 4.6 to 7.1 percent and 0.67 mm [0.027 in] to 0.77 mm [0.031 in], respectively). Mixes *B1* and *B2* have comparable percent air voids (4.9 to 8.8 percent for B1 versus 4.8 to 8.2 percent for B2), but mix *B2* has larger air void sizes (0.65 mm [0.026 in] to 0.85 mm [0.035 in] for *B1* versus 0.76 mm [0.031 in] to 0.97 mm [0.039 in] for B2) as shown in Figure 3.9, Figure 3.10, and Table 3.18. Note that the average air void content for all samples after trimming is 6.5 ± 1.0 percent.

Table 3.18. Air Void Content and Air Void Size Characteristics of the 100 mm (4 in) Height Samples

Mix type	Air void content (%)			Air void size (mm)		
	Minimum	Maximum	Average	Minimum	Maximum	Average
A1	4.6	7.1	5.7	0.67	0.77	0.72
A2	4.1	9.3	5.9	0.63	0.85	0.71
B1	4.9	8.8	6.9	0.65	0.85	0.75
B2	4.8	8.2	6.9	0.76	0.97	0.86
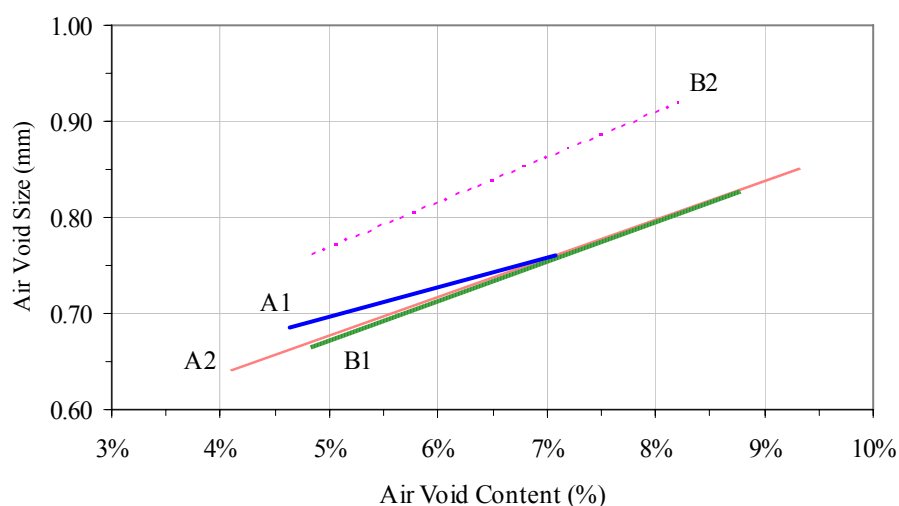
Figure 3.10. Relationship between air void size and air void content

Moisture Conditioning

Half of the prepared samples were subjected to moisture conditioning following the modified Lottman procedure without the freezing step (AASHTO 2002c). The samples were subjected to vacuum saturation to a target level between 70 to 80 percent. The degree of saturation of the sample was measured by weight using Equation 2.10 with $P_a = \%AV$ from Tables 3.16 and 3.17. To determine the time required to vacuum saturate the samples to achieve the specified degree of saturation, several tests were performed on trial samples by applying a partial vacuum between 650 mm to 700 mm Hg (26in to 28 in). The required vacuum saturation time for gradation *A* samples of 100 mm (4 in) in diameter by 150 mm (6 in) height was 2 min while for gradation *B* samples trimmed to 100 mm (4 in) in diameter by 100 mm (4 in) height the required vacuum

saturation time was 35 s. The degree of saturation for the asphalt mix replicates is reported in Table 3.19.

Table 3.19. Level of Saturation for the Moisture Conditioned Samples

| Replicate | Mix type | | | |
	A1-MC	A2-MC	B1-MC	B2-MC
1	79	85	76	73
2	77	84	77	78
3	81	79	74	69
4	71	82	71	–
5	79	81	65	–
6	80	78	77	–

After measuring the degree of saturation, the samples were kept in water and transported to a water bath at 60 °C (140 °F). The samples were completely submerged inside the hot circulating water, leaving about 25 mm (1 in) of water above their surfaces as shown in Figure 3.11. After 24 h in the hot water bath, the samples were removed and placed in water at room temperature for an additional 2 h. The samples were then removed from the water bath at room temperature and left to air dry before testing.

The percent porosity, defined as the fraction of voids connected to the surface and accessible to water (water-permeable voids), was measured using the Corelok® system and used in lieu of the total air void content to compute the degree of saturation (InstroTek 2003b). The percent porosity in all cases was considerably lower than the total air void content, ranging from 2.3 to 6.6 percent. Therefore, the degree of saturation computed using the percent porosity yielded values close to or above 100 percent. A value higher than 100 percent would imply that water not only filled the water-permeable voids but also permeated into the asphalt binder or possibly caused more connectivity between voids due to moisture damage.

Figure 3.11. Samples submerged in the circulating hot water bath during the moisture conditioning procedure

CHAPTER IV

MOISTURE TRANSPORT IN ASPHALT MIXES [*]

The majority of the research on moisture damage is based on the hypothesis that infiltration of surface water is the main source of moisture damage. The problem is usually explored assuming moisture is already present or saturating the asphalt mix, without investigating the mechanism of moisture transport. One factor that has been usually overlooked and thus left out of these discussions is how moisture gets inside the asphalt pavement. Even in dry places with a limited amount of rainfall, like Arizona, pavement distresses due to moisture damage have been observed and reported (Hicks 1991). Therefore, in some dry regions capillary rise and moisture diffusion could be the main source of moisture reaching the asphalt pavement rather than infiltration of surface water.

Three mechanisms of moisture transport in asphalt pavements can be identified:

a) infiltration of surface water,

b) capillary rise of subsurface water, and

c) permeation or diffusion of water vapor.

In this study, the infiltration of surface water and capillary rise mechanisms were studied using laboratory experiments. Permeability tests were performed and the results corroborated with a computer algorithm developed to analyze the connectivity of air voids using X-ray CT images. Capillary rise was also evaluated using a laboratory test setup along with several X-ray CT image analysis techniques used to determine the amount and size of air voids filled with water. These results were used in the capillary rise equation to estimate the distribution of contact angles between water and asphalt mastic. The next section includes a description of some recent experiments regarding diffusion of water vapor performed by others. Then, the permeability measurements and connectivity algorithm are described. The last section of the chapter includes a description of the capillary rise experiment, analysis, and results.

Diffusion of Water Vapor

Studies with regard to diffusion of water vapor in asphalt mixes are limited. Because moisture damage occurs even in mixes with very low percent air voids, a research project was recently conducted to develop a new test method to assess the permeation of water vapor in asphalt mixes (Sasaki et al. 2006). The evaluation of moisture permeation utilized a test apparatus that simulated the fluctuations in ambient temperature, ambient relative humidity, and pavement surface temperature and measured the water content in terms of weight increase (stored water weight). Two different types of field core samples were analyzed in that study; some samples belonged to a runway that had moisture damage distresses, while other samples belonged to an unaffected road pavement. The air void content of the runway samples was 3.5 percent, and the air void content of the road samples was 4.7 percent. The moisture permeation test was able to detect moisture vapor diffusion, accumulation, and variation with respect to daily temperature fluctuations. More importantly, the results were able to differentiate between the two sample types; the sample coming from the runway showing moisture damage distress registered a larger water storage (about 15 g [0.03 lb] after 18 h), while the sample corresponding to the unaffected area stored a smaller amount (about 5 g [0.01 lb] after 18 h) as shown in Figure 4.1.
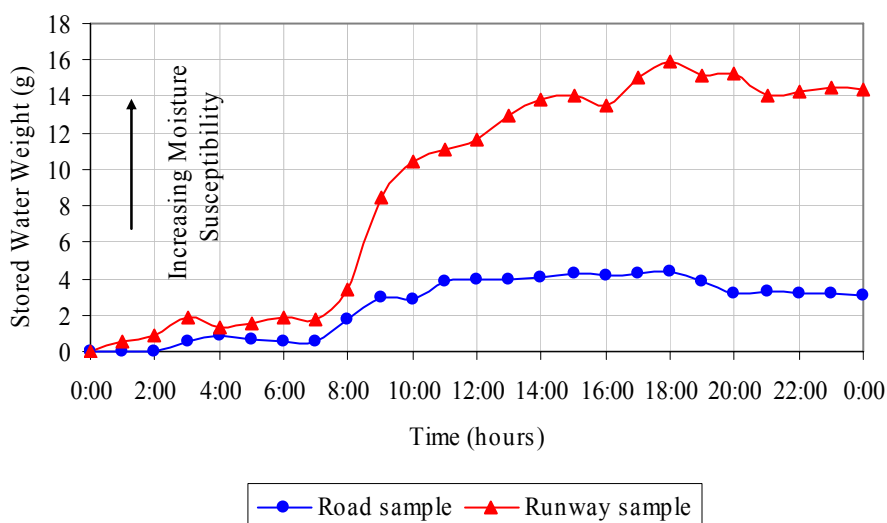
Figure 4.1. Weight change during the moisture permeation test (Adapted from Sasaki et al. 2006)

The diffusion coefficients of asphalt mastic samples were recently determined using the suction potential of sand asphalt samples made of a mix of fine aggregates (passing the no. 16 fg1.18 mm] sieve) and asphalt binder (Kassem et al. 2006). A thermocouple psychrometer introduced in the sand asphalt samples was used to measure the changes in relative humidity. The top of the samples was sealed with silicon glue to minimize the interchange of moisture with the environment, and then the samples were placed in a shallow water bath at room temperature. Periodic humidity readings were acquired, and the diffusion coefficients estimated. As shown in Figure 4.2, the sand asphalt samples belonging to the mix with good field performance in terms of moisture susceptibility (mix 1) had a lower diffusion coefficient value and a larger elapsed time for the psychrometer to detect changes in relative humidity. The opposite was true for the mixes with fair to poor field performance (mix 2 and 3) as shown in Figure 4.2. In addition, measurements of total suction using the same type of psychrometers in asphalt mixes were used to create suction-moisture content curves. The study found good correlation between moisture diffusion, air void structure of the mix, and moisture damage.
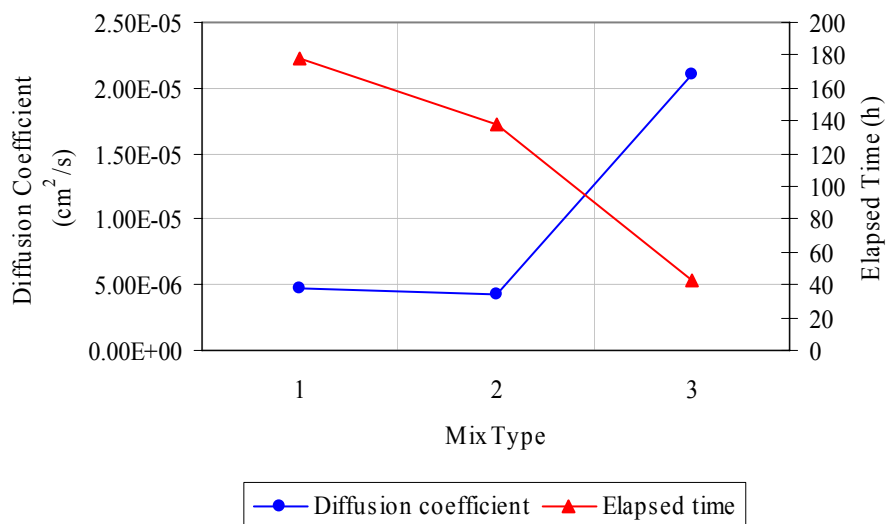
Figure 4.2. Diffusion coefficient and elapsed time for the psychrometer to detect changes in relative humidity in sand asphalt samples (Adapted from Kassem et al. 2006)

Infiltration of Surface Water

The permeability of a porous media measures the ability of the material to transmit and drain water. The constant head method was used to measure the permeability of several gradation *A* and *B* samples (ASTM 2006e). During the test, each sample was wrapped with a rubber membrane and then placed inside a triaxial type permeability cell, where water was used to apply a lateral confining pressure of 34.5 kPa (5 psi). Then, pressure was applied to induce water flow through the sample. Even at relatively high levels of applied pressure (up to 276 kPa [40 psi]) no water flow was achieved. A second attempt was made after vacuum saturating the samples with water to a level of 70 to 80 percent. Similar to the first case, no water flow through the sample was achieved. A third attempt was done using vacuum saturated porous stones on top of the vacuum saturated sample in an effort to even out the flow at the boundaries, but again no water flow was achieved. Research experience shows that sawing the edges of compacted asphalt mix cylinders can significantly reduce their permeability (Maupin 2000). To rule out this possibility, new samples of gradation *A* were prepared without trimming the top and bottom edges (165 mm [6.5 in] height). Unsaturated and vacuum saturated samples were tested, and no water flow was achieved in either case. Therefore, the conclusion was that gradation *A* and gradation *B* samples are impermeable.

Air Void Connectivity Algorithm

The lack of permeability observed in the asphalt mix samples was also corroborated using X-ray CT image analysis by estimating the vertical air void connectivity in the samples. The air void connectivity was explored by converting the threshold images into binary files using Image-Pro® Plus. The binary files, which consist of a matrix of numbers, are formed by translating each pixel in the image into a numerical value. If the pixel represents a void, the corresponding number in the binary file is a zero, and if it represents a solid, the corresponding number is a one. The binary files were then used as input in a FORTRAN-built algorithm presented in Figure 4.3.
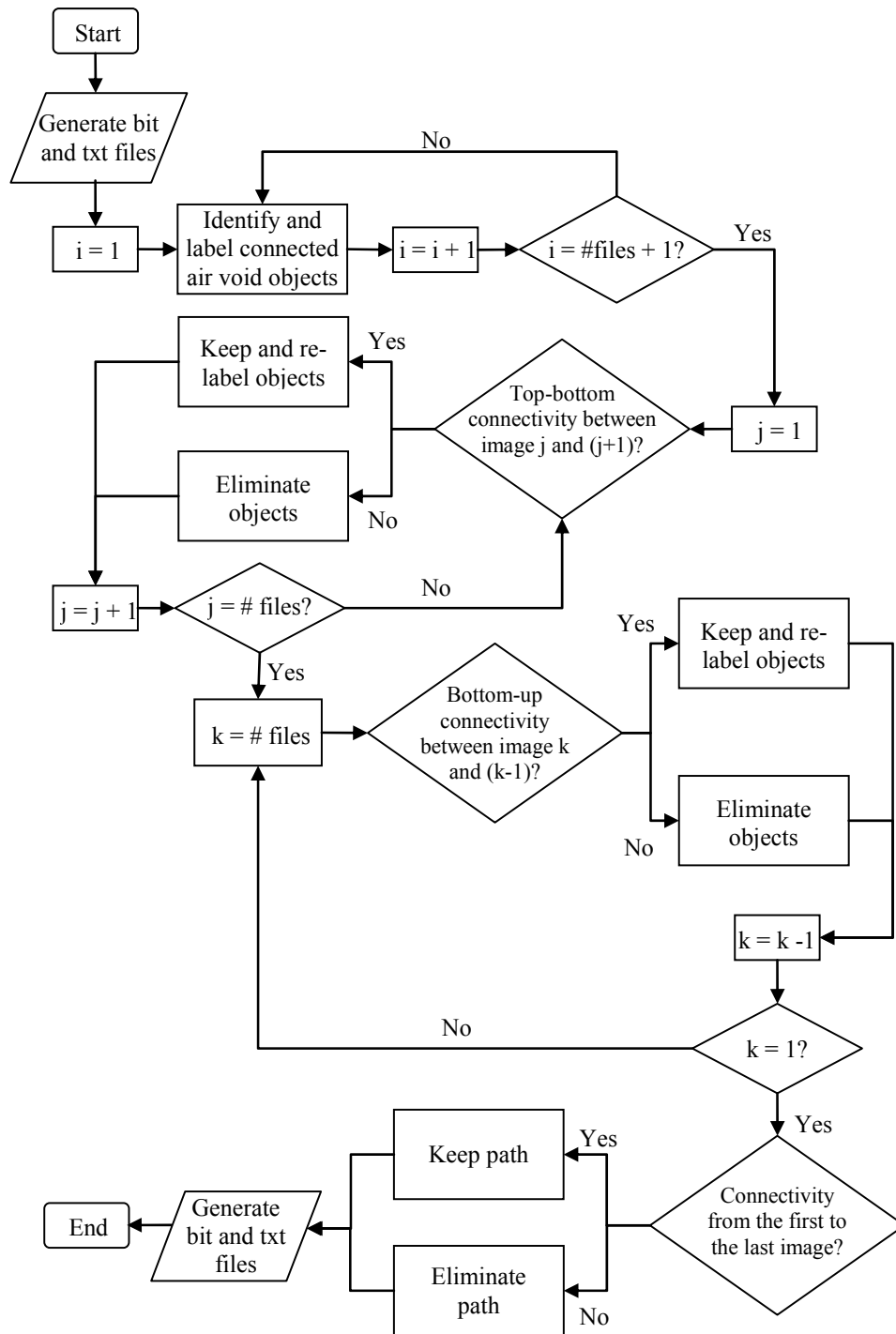
Figure 4.3. FORTRAN algorithm for analyzing air void connectivity

The algorithm takes each binary file and revises every numerical value. When it encounters a zero, it checks the eight immediate surrounding numbers and if there are any zeros in those positions, they are grouped together as part of the same air void object. Then, the algorithm proceeds to analyze the vertical connectivity starting from the first input file, in this case the top image. For each identified air void object, it checks the same position in the next image and the eight immediate surrounding numbers to that position. If there is another zero in any of those places, the voids are considered connected in the vertical direction and given the same air void object number. To account for the tortuosity in the air paths, the process is repeated, this time starting from the last input file that corresponds to the bottom image. Finally, the objects that are not vertically connected all the way from the first to the last image are eliminated.

The output of the algorithm is a set of binary files (BIT extension files) containing the connected air void paths and a text file specifying the area, perimeter, and volume of the objects belonging to each path. The binary output files were processed with Image-Pro® Plus software to convert them back into images, which show as black objects the connected voids or are blank if no connected voids were identified in the sample. The output of the connectivity analysis for both gradation *A* and gradation *B* samples resulted in blank images, meaning that no connected voids could be detected in any of the analyzed samples. This finding supports the lack of permeability in the samples that was discussed in the previous section.

Capillary Rise of Subsurface Water

One of the least explored mechanisms of moisture transport in asphalt mixes is capillary rise of subsurface water. As shown in Figure 4.4 and described by the capillary rise equation subsequently, water tends to rise and wet a surface due to its hygroscopic properties and to the surface tension of its contractile skin.
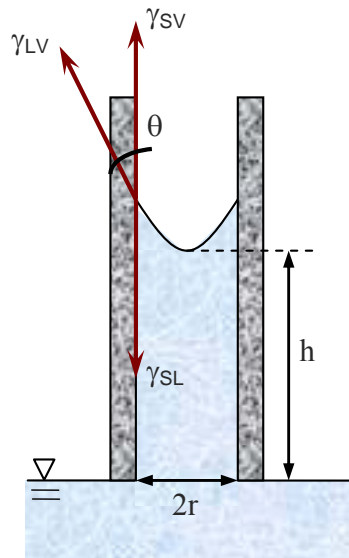
Figure 4.4. Schematic of the forces acting on a capillary tube

The equilibrium of the vertical forces acting in the capillary tube, the liquid vapor interfacial energy (γ_{LV}), the solid vapor interfacial energy (γ_{SV}), and the solid liquid interfacial energy (γ_{SL}) that are shown in the schematic of Figure 4.4 can be described by the capillary rise equation (Fredlund and Rahardjo 1993):

$$2\pi r \gamma_{LV} \cos\theta = \pi r^2 hg\rho \qquad (4.1)$$

where r is the radius of the capillary tube, θ is the contact angle, h is the height of the column of water, g is the acceleration due to gravity, and ρ is the density of water. The left-hand side of Equation 4.1 represents the resultant of the surface tension of the water, and the right-hand side is the weight of the column of water.

The surface tension around the circumference of the capillary tube acts at an angle (θ) from the vertical, equivalent to the contact angle previously presented in Figure 2.13. The magnitude of the contact angle is a function of the type of tube material. In the case of asphalt mixes, the hydrophobic nature of the asphalt binder coating the aggregates will result in a contact angle close to 90°, and thus no water rise would be observed. However, the aggregate coating consists not only of pure asphalt binder but also of a mixture of asphalt binder and fine aggregate particles or mastic, which is capable of attracting water to its surface.

In order to investigate the mechanism of capillary rise in asphalt mixes a laboratory experiment using X-ray CT was employed for observing the bottom-up water rise (assuming a subsurface water source) into the void structure of asphalt mix samples. Then, the air void connectivity algorithm previously described was used to assess the air voids filled with water. Subsequently, the radius or size of the voids filled with water along with the observed level of water rise was used in the capillary rise equation to estimate the contact angle between the water and the asphalt mastic.

The next section provides a description of the asphalt capillary rise test setup. Then, the connectivity analysis results and the assessment of water rise using X-ray CT image analyses methods are included. At the end of this section, the estimation of the contact angle between the water and the mastic is presented.

Air Void Structure of the Samples Used in the Capillary Rise Experiment

Six individual trimmed samples having a dimension of 100 mm (4 in) diameter by 100 mm (4 in) height and belonging to mix types *A1*, *A1-MC*, *A2*, *A2-MC*, *B1*, and *B2* were used in this experiment. The samples were scanned in dry condition to estimate their air void structure using Equations 3.9 to 3.11. In Figures 4.5 and 4.6, the 25th, 50th, and 75th percentiles of the air void content and air void size for the individual samples used in the capillary rise experiment are presented, respectively. A percentile represents a value that has a specified percent of the total number of measurements below it, e.g., 25 percent below for the 25th percentile. The percentiles are useful to rank the measurements and estimate the variability or spread of the results. The percentiles for the air void content and size for each individual sample are reported in Table 4.1.
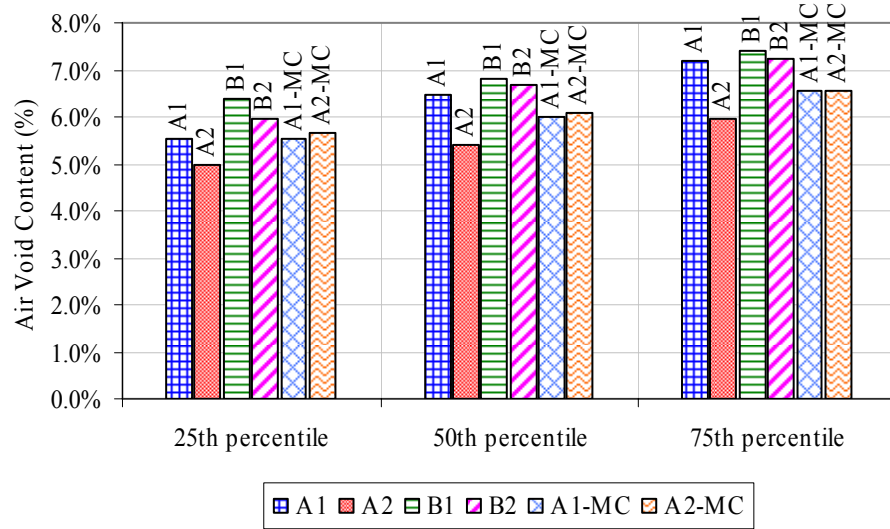
Figure 4.5. Percentiles of the air void content for the individual samples
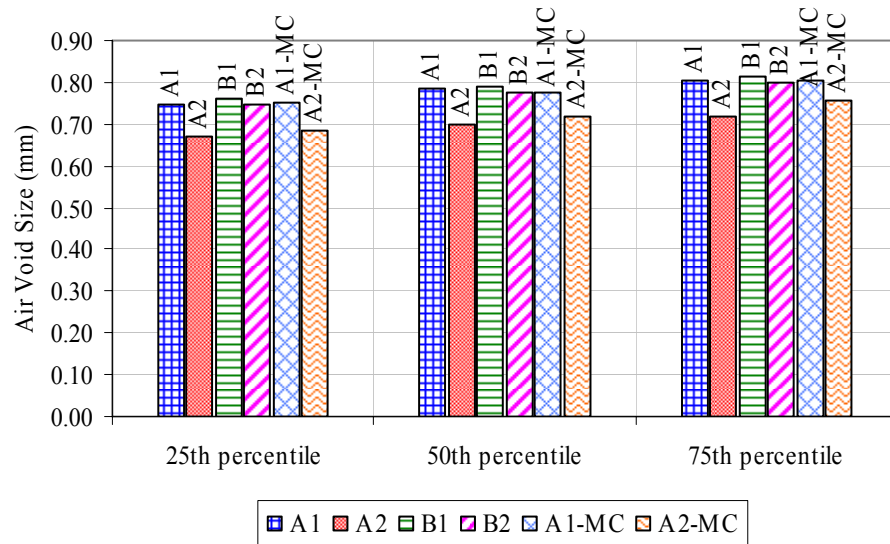
Figure 4.6. Percentiles of the air void size for the individual samples

Table 4.1. Percentiles of the Air Void Content and Air Void Size for the Individual Trimmed Samples Used in the Capillary Rise Experiment

Mix type	Air void content (%)			Air void size (mm)		
	25th	50th	75th	25th	50th	75th
A1	5.5	6.5	7.2	0.75	0.78	0.81
A1-MC	5.5	6.0	6.5	0.75	0.78	0.80
A2	5.0	5.4	6.0	0.67	0.70	0.72
A2-MC	5.6	6.1	6.5	0.69	0.72	0.75
B1	6.4	6.8	7.4	0.76	0.79	0.82
B2	6.0	6.7	7.2	0.74	0.77	0.80

According to Figure 4.5 and Table 4.1, the air void content percentiles for mixes *A1*, *B1*, and *B2* are larger than the other samples. In addition, sample *A2* has the lowest air void content percentile values among all samples. The percentile results for the air void size show similar values for mixes *A1*, *A1-MC*, *B1*, and *B2*; only mix *A2* had a somewhat lower air void size percentile values (Figure 4.6).

Experimental Setup

To assess the potential of water rise in asphalt mixes, the samples were allowed to sit in a shallow distilled water bath at a constant depth of 10 mm (0.4 in) for a period of 36 days (Figure 4.7). An initial X-ray scan was done on the samples, and then scans were performed after 7, 13, 25, 29, and 36 days. The scanning method and image analysis were the same as described in Chapter III, except that the slices were captured every 0.5 mm (0.02 in) in the vertical direction (voxel size of 0.195 mm [0.008 in] by 0.195 mm [0.008 in] by 0.5 mm [0.02 in]) and that only 20 mm (0.8 in) of the sample height was scanned.

To prevent lateral water evaporation, the sides of the samples were covered with a 0.3 mm (0.012 in) thick nonporous latex rubber membrane. The top and bottom of the sample were left uncovered. To improve the water accessibility through the bottom of the sample, a perforated foam pad was placed under the samples as shown in Figure 4.7.

The water bath containing the samples was covered during the first 25 days of the wetting period to promote an environment of high relative humidity and to prevent excessive water evaporation. After 25 days, the water bath was uncovered to create a greater gradient between the relative humidity of the ambient air and the bottom of the samples. The depth of the water bath was kept constant at 10 mm (0.4 in) throughout the experiment.

The samples were transferred from the water bath to a container using impermeable foam at the bottom in an effort to prevent water loss during transfer. This impermeable foam was removed prior to scanning and replaced with a perforated foam pad as shown in Figure 4.8. The perforated foam pad was used at the bottom to improve water accessibility since water at a depth of 10 mm (0.4 in) was used to allow a constant supply during the scanning period.
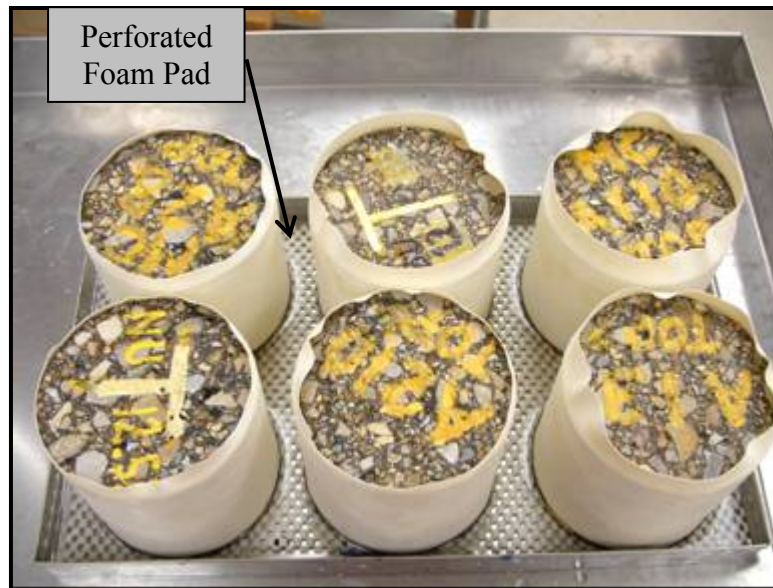
Figure 4.7. Sample setup during the capillary rise laboratory experiment
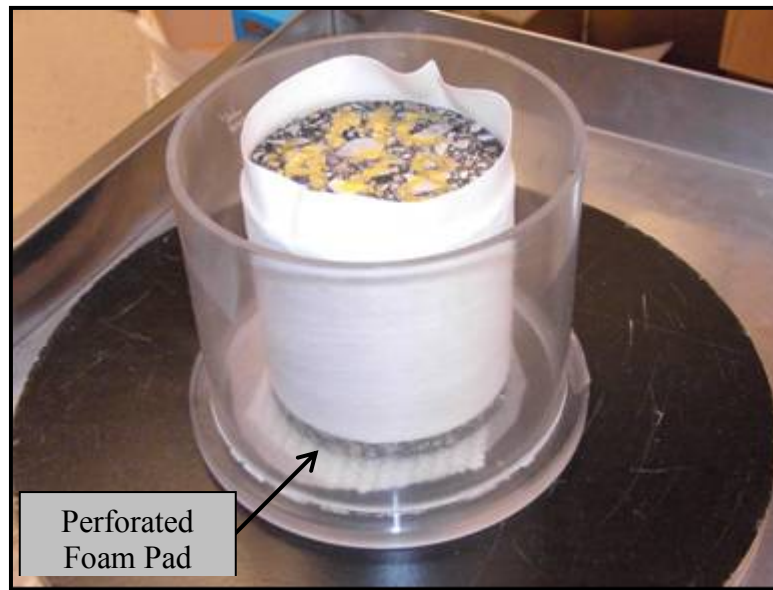
Figure 4.8. Scanning container and sample setup during scanning

Air Void Connectivity

When the thick nonporous latex rubber membranes were removed from the samples at the end of the experiment, it was observed that the membrane had pulled water up all the way to the top. Therefore, the outer 2 mm (0.08 in) along the circumference of the sample was not considered in the connectivity or subsequent water rise analysis. The connectivity algorithm presented before was used to analyze the air void connectivity within the scanned depth of the individual samples. The output files of the algorithm were processed with Image-Pro® Plus software, and then using Amira software the images were stacked to create a 3D render. Figure 4.9 shows the renders of the connected voids for each individual sample with the *x* and *y* axes spanning 100 mm (4 in) and the z-axis 20 mm (0.8 in). Based on these results, the connected voids are not uniformly distributed within a sample, which highlights the heterogeneity of the air void structure in asphalt mixes. Table 4.2 reports the air void content of the connected and total air voids in the bottom 20 mm (0.8 in) of the sample height corresponding to the scanned depth.

Table 4.2. Total and Connected Air Void Content in the Bottom 20 mm (0.8 in) of the Sample

Mix type	Connected air voids (%)	Total air voids (%)
A1	0.94	5.98
A1-MC	2.36	5.87
A2	1.28	5.40
A2-MC	2.04	6.22
B1	1.66	5.19
B2	0.58	4.28

(a)　　　　　　　　　　　　　　　(b)

(c)　　　　　　　　　　　　　　　(d)

(e)　　　　　　　　　　　　　　　(f)
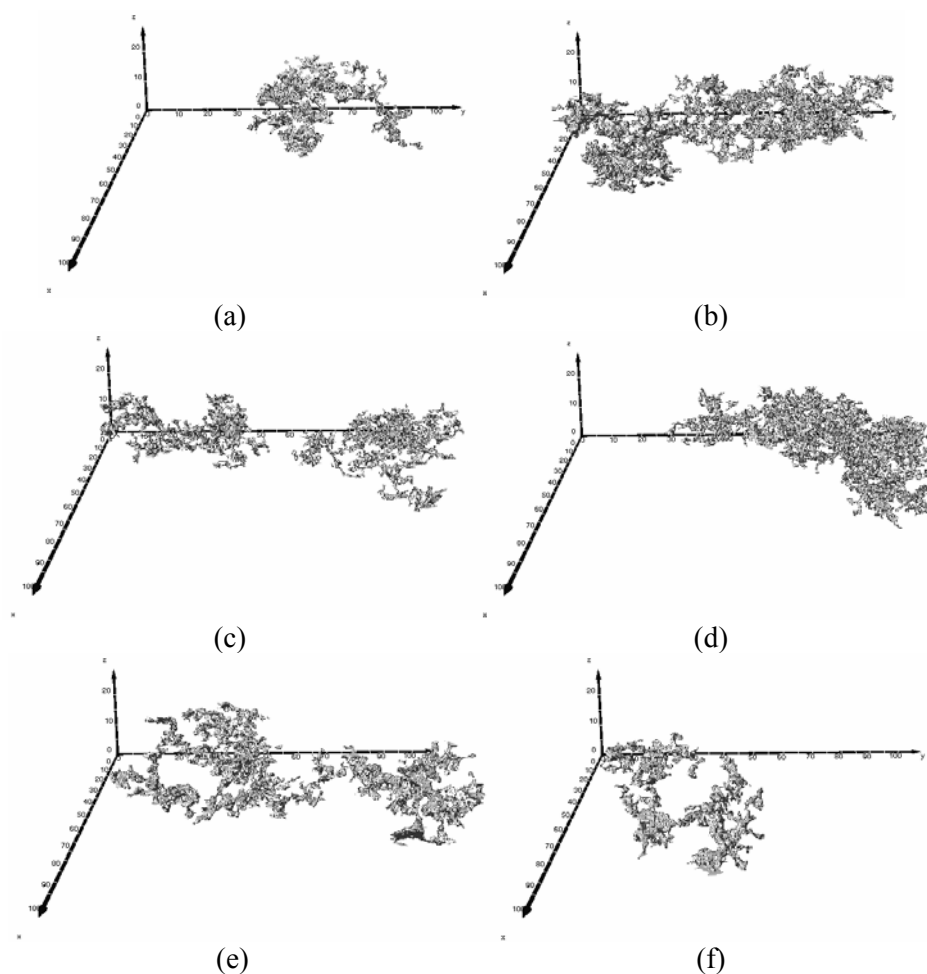
Figure 4.9. 3D renders of the connected voids in the bottom 20 mm (0.8 in) of the individual samples. (a) *A1* (b) *A1-MC* (c) *A2* (d) *A2-MC* (e) *B1* (f) *B2*

Histograms (normalized with respect to the total object count for each sample) of the connected air void sizes are presented in Figures 4.10 and 4.11. Among the dry samples, *A2* had

the highest percentage of small voids (Figure 4.10). The conditioned samples had similar air void structures (Figure 4.11) and the highest percentage of connected voids (Table 4.2).
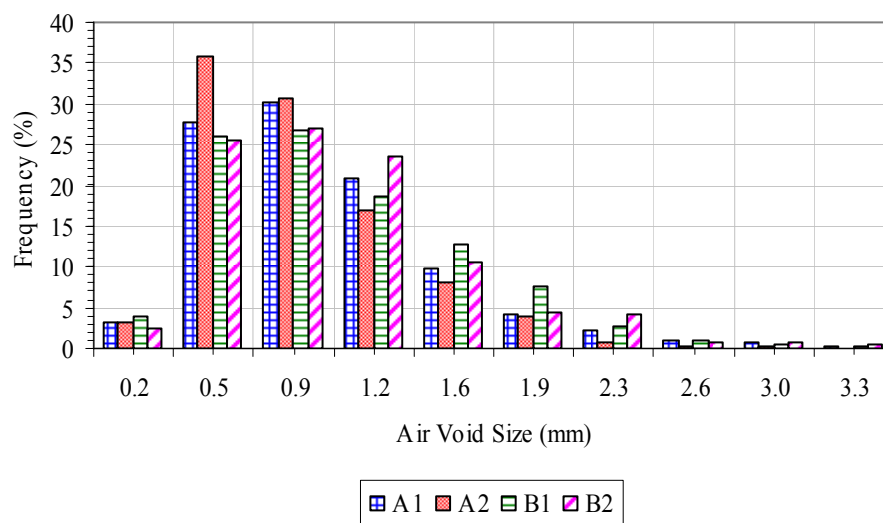
Figure 4.10. Histograms of the air void size for the connected voids in the bottom 20 mm (0.8 in) of the unconditioned samples
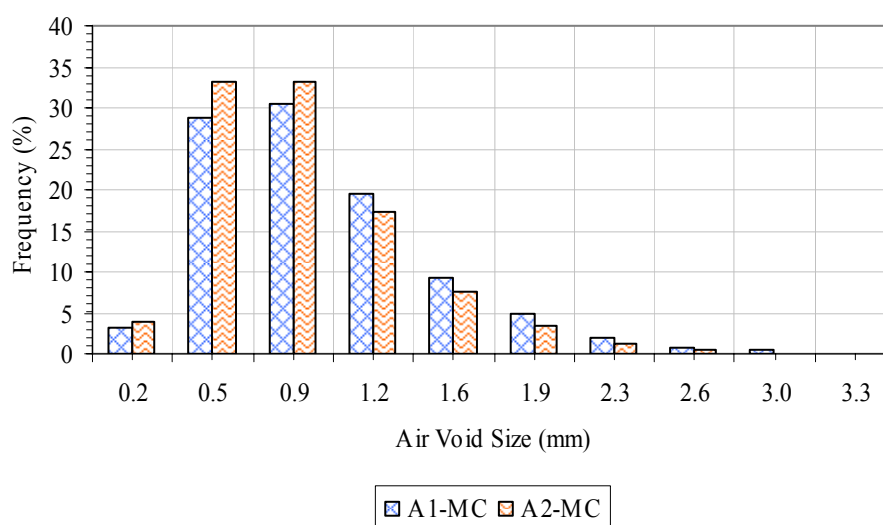
Figure 4.11. Histograms of the air void size for the connected voids in the bottom 20 mm (0.8 in) of the moisture conditioned samples

The significance of these air void structures in capillary rise is discussed in the following section. Moisture conditioning was expected to give a calculated percentage of connected voids less than the actual value because water density is close to asphalt density and it would be considered as part of the asphalt phase during image threshold based on gray intensity (a function of material density). Therefore, the fact that the connected air voids in the conditioned samples was higher suggests that another mechanism could have caused this phenomenon. It is possible that the moisture conditioning damaged the samples in terms of washing some asphalt away or opening new flow paths inside the samples.

Capillary Rise Results

A method developed and used to measure permeability and porosity in rocks was employed in this study to assess the level of water rise in the asphalt mix samples (Ketcham and Iturrino 2005). The method consists of performing a 3D alignment and comparison of scans performed initially on dry samples and after capillary rise of water. Beam attenuation, which is a function of the material density, atomic number, and X-ray energy, forms the basis of this methodology. When the beam of X-rays passes through a void space, the attenuation is less than when it passes through a fluid. Therefore, by subtracting the data set of the initial scans from that acquired after water rise, when some or the total amount of air has been displaced by water, an estimate of the air voids filled with water can be obtained. During the capillary rise experiment, scans after 7, 13, 25, 29, and 36 days were performed on the samples, and therefore the alignment of the images acquired at different times was critical.

After running the algorithm to align and subtract the initial images from the images after capillary rise, the result was a new image showing in white the voids filled with water. In Figures 4.12 and 4.13 the results for samples *B1* and *A2* after 7, 25, and 36 days are presented. Practically no water rise was observed in sample *B1* after 7 days, while water had infiltrated into the air void structure after 25 and 36 days. For sample *A2*, even after 36 days of wetting, no significant water rise was detected.

(a)   (b)   (c)
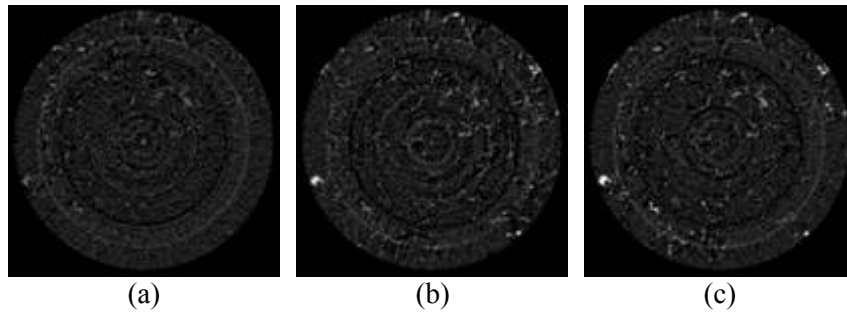
Figure 4.12. Resulting images after alignment and subtraction for mix type *A2* showing in white the permeated water at a height of 20 mm (0.8 in). (a) after 7 days (b) after 25 days (c) after 36 days

(a)   (b)   (c)
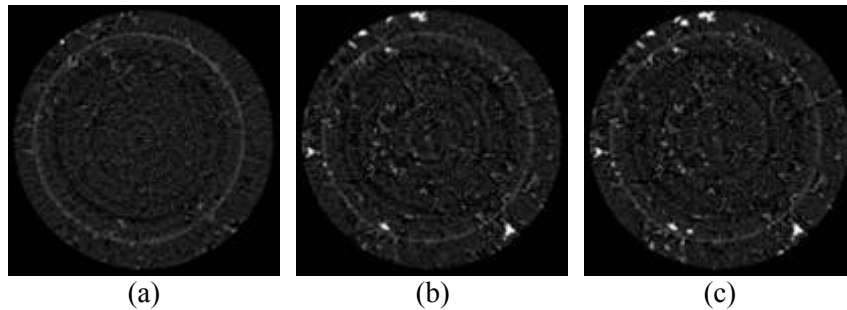
Figure 4.13. Resulting images after alignment and subtraction for mix type *B1* showing in white the permeated water at a height of 20 mm (0.8 in). (a) after 7 days (b) after 25 days (c) after 36 days

The images after alignment and subtraction were further thresholded and inverted to show again in black the air voids filled with water. Using Amira software, the images were stacked to create 3D renders. Figures 4.14 and 4.15 show the resulting renders after 7, 13, and 25 days of wetting for samples *B1* and *B2*, respectively. The objects represent the voids filled with water. Based on these illustrations, more voids filled with water were observed as time evolved. In addition, sample *B1* had more water due to capillary rise as compared to sample *B2*.

(a)

(b)

(c)
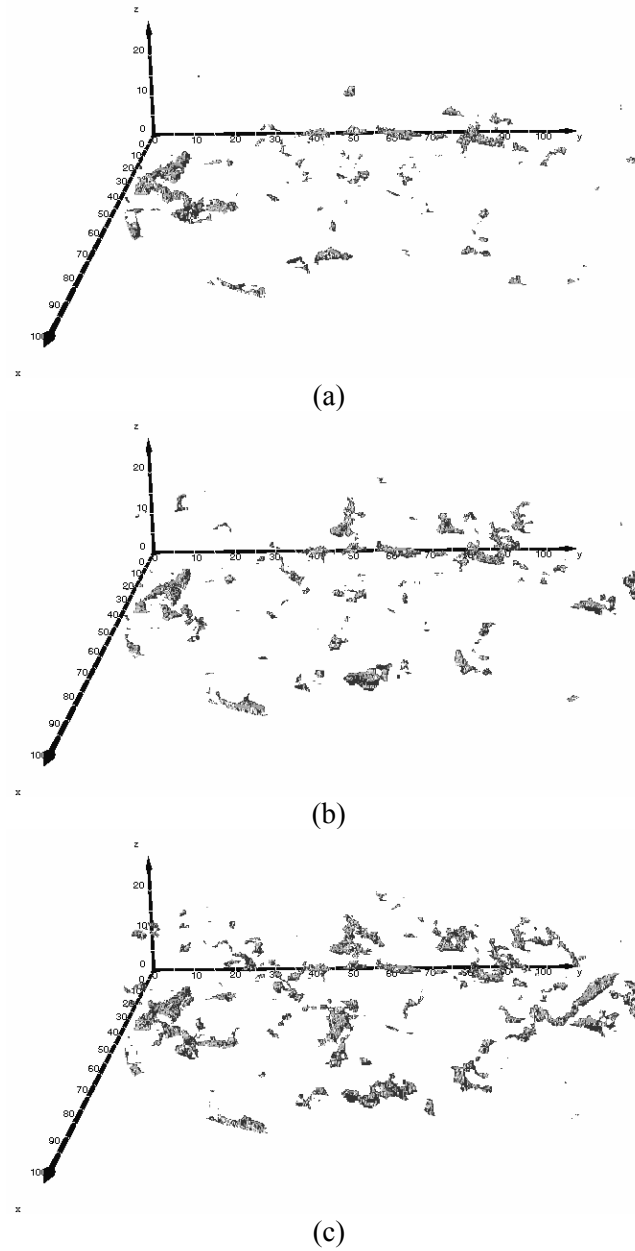
Figure 4.14. 3D renders for individual sample of mix type *B1*. (a) after 7 days (b) after 13 days (c) after 25 days

(a)

(b)

(c)
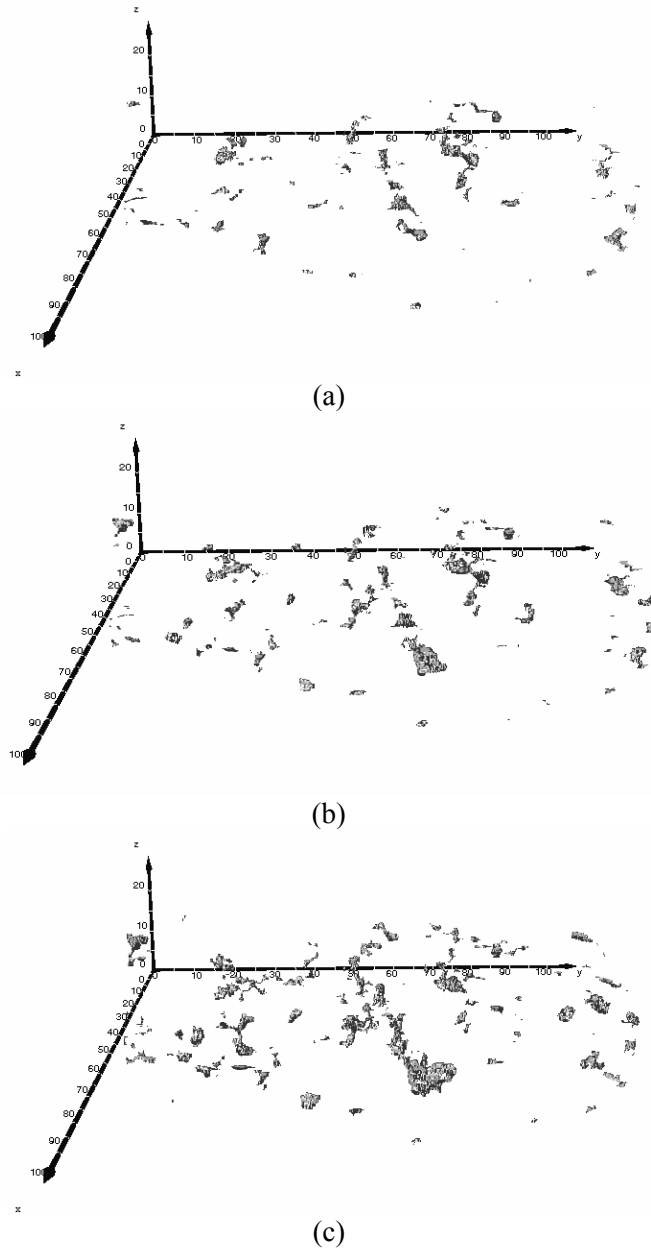
Figure 4.15. 3D renders for individual sample of mix type *B2*. (a) after 7 days (b) after 13 days (c) after 25 days

The individual samples in which water reached a higher level with respect to depth were *A1*, *B1*, and *B2*, while the amount of voids filled with water in samples *A1-MC*, *A2*, and *A2-MC* was much less. Among the unconditioned samples, *A2* had the lowest percentile of total air void

content and air void sizes (Figures 4.5 and 4.6) and it had the smallest frequency of sizes for the connected air voids within the bottom 20 mm (0.8 in) of the sample height (Figure 4.10).

Based on the static capillary rise equation (Equation 4.1), smaller air voids should have a higher level of capillary rise. However, the velocity of capillary rise becomes slower as the air void size decreases. This phenomenon is well described by the Washburn equation for the rate of capillary rise (Washburn 1921):

$$\frac{dl}{dt} = \frac{\left[P_A + g\rho h + \frac{2\gamma_{LV}}{r}\cos\theta\right]\left(r^2 + 4\varepsilon r\right)}{8\mu l}$$ (4.2)

where P_A is the atmospheric pressure, g is the acceleration due to gravity, ρ is the density of the liquid, h is the height of the column of water above the saturation surface, γ_{LV} is the interfacial energy of the liquid, θ is the angle of contact, r is the radius of the capillary tube, ε is the coefficient of slip, μ is the viscosity of the liquid, and l is the length of the column of liquid in the capillary. Therefore, in the samples with smaller air void sizes, the expected velocity of the capillary rise is less. This explains why no capillary rise was detected within the experiment period in sample *A2*, which had the smallest void sizes.

The conditioned samples (*A1-MC* and *A2-MC*) also had negligible water rise. Moisture conditioning increases the relative humidity (*RH*) in the mix, resulting in a reduced potential of water rise in those mixes. This phenomenon is described by Laplace's equation for cylindrical pores (Young et al. 1998):

$$\ln(RH) = -\frac{2\gamma_{LV}\cos\theta}{r}$$ (4.3)

As shown in Equation 4.3, the contact angle increases (less wetting) as *RH* increases. Another possible reason for the observed behavior is that the image resolution was not small enough to capture the smaller voids and microcracks opened by the conditioning, and some of the capillary rise could have occurred in these microcracks (Chen et al. 2004; Mohamed et al. 1993).

To estimate the water rise in the samples with time, the amount of air voids filled with water during the wetting period was estimated using Equation 3.10. The values of percent of air voids filled with water with respect to the total volume of a sample are presented in Figure 4.16, and the fraction of these air voids with respect to the connected air voids in the bottom 20 mm (0.8 in) of the sample is presented in Figure 4.17. For samples *A2-MC* and *B1* it was not possible

to align and subtract the set of images acquired after 36 and 29 days, respectively, from the initial dry images and thus the corresponding results are unavailable. Samples *A1-MC*, *A2-MC,* and *A2* did not show water rise for the first 13, 25, and, 29 days, respectively. Sample *B1* had the largest percent of air voids filled with water after 36 days, followed by sample *B2* and then *A1*.

The fraction of air voids filled with water with respect to the connected air voids in the bottom 20 mm of the sample was largest for sample *B2* followed by sample *B1* and then *A1*. This indicates that although sample *B1* had the largest percent of air voids filled with water after 36 days, this number only represented around 50 percent of the available connected voids and probably more water rise would have been observed with additional elapsed time.
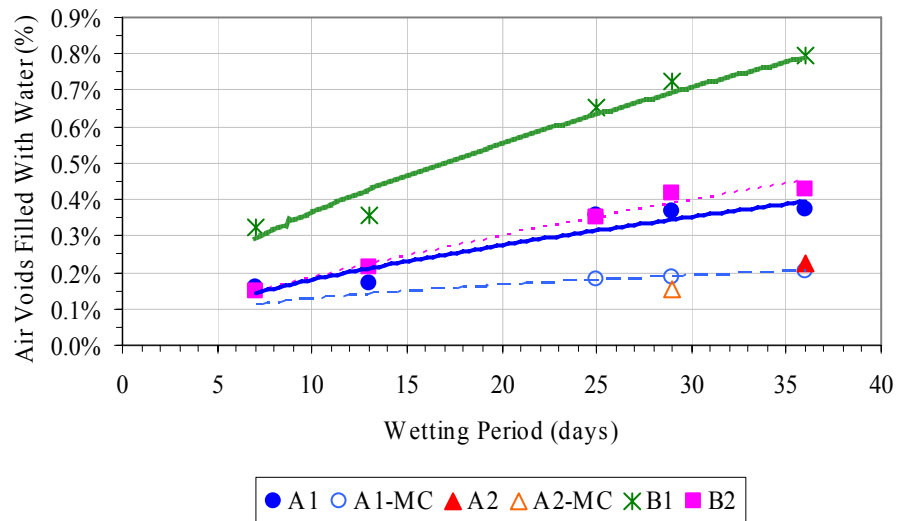
Figure 4.16. Air voids filled with water in the bottom 20 mm (0.8 in) of the sample at different wetting times
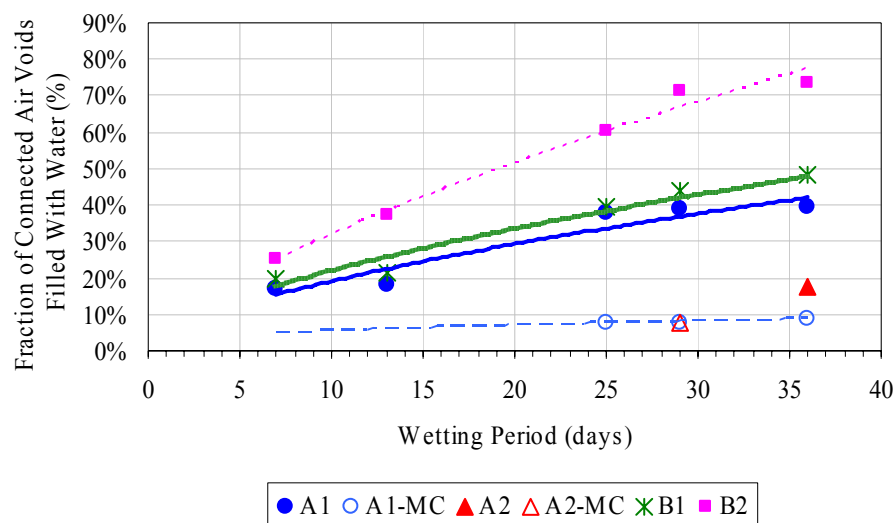
Figure 4.17. Percent of the connected air voids filled with water in the bottom 20 mm (0.8 in) of the sample at different wetting times

Using the trend lines presented in Figure 4.16, an estimate was obtained of the wetting period that would be required to fill all the connected voids in the bottom 20 mm (0.8 in) of the sample. The percent connected air void values was previously presented in Table 4.2. The power equations used to fit the data points, R-squared values, and estimated wetting period are presented in Table 4.3. The results show that mix *B2* has the shortest estimated wetting period, which is consistent with Figure 4.17, where mix *B2* shows the largest fraction of connected voids filled with water at the end of the experiment. Also consistent with Figure 4.17, mix *A1-MC* had the largest estimated wetting period, while mix *B1* and *B2* had similar wetting periods.

Table 4.3. Estimated Wetting Period to Fill All Connected Air Voids in the Bottom 20 mm (0.8 in) of the Sample

Mix type	Power equation [a]	R-squared value	Estimated wetting period (days)
A1	$\%AV_{filled} = 0.0004(t)^{0.6142}$	0.8944	170.7
A1-MC	$\%AV_{filled} = 0.0005(t)^{0.3728}$	0.9732	30916.3
B1	$\%AV_{filled} = 0.0009(t)^{0.6060}$	0.9370	122.7
B2	$\%AV_{filled} = 0.0004(t)^{0.6934}$	0.9910	47.3

[a] With $\%AV_{filled} = \%AV_{connected}$

Contact Angle for the Mastic

The images corresponding to a wetting period of 36 days (assuming the water had reached a level close to equilibrium) were used to estimate the contact angle for the mastic using the capillary rise equation:

$$\theta = \cos^{-1}\left(\frac{rhg\rho}{2\gamma_{LV}}\right) \tag{4.4}$$

where $h = 10$ mm, $g = 980$ cm/s^2, $\rho = 1$ g/cm^3, and $\gamma_{LV} = 72.8$ erg/cm^2. For the estimation of the contact angle, the value of r in Equation 4.4 was the size of the air voids filled with water at each level. With these results, histograms (normalized with respect to the total object count for each sample) of the contact angles were obtained for each sample, as presented in Figures 4.18 and 4.19. These results show that the unconditioned samples, with a greater level of water rise (*A1*, *B1*, and *B2*), are the ones with a larger frequency of smaller contact angle values and a smaller frequency of larger contact angle values. The moisture conditioned samples (Figure 4.19) had larger contact angles than *A1*, *B1*, and *B2* (Figure 4.18).
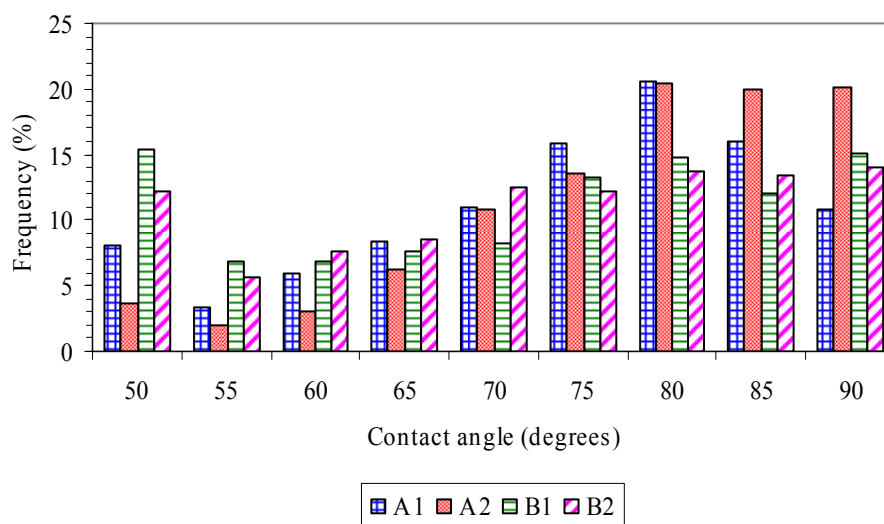
Figure 4.18. Histograms of the estimated contact angle for the mastic of the unconditioned samples
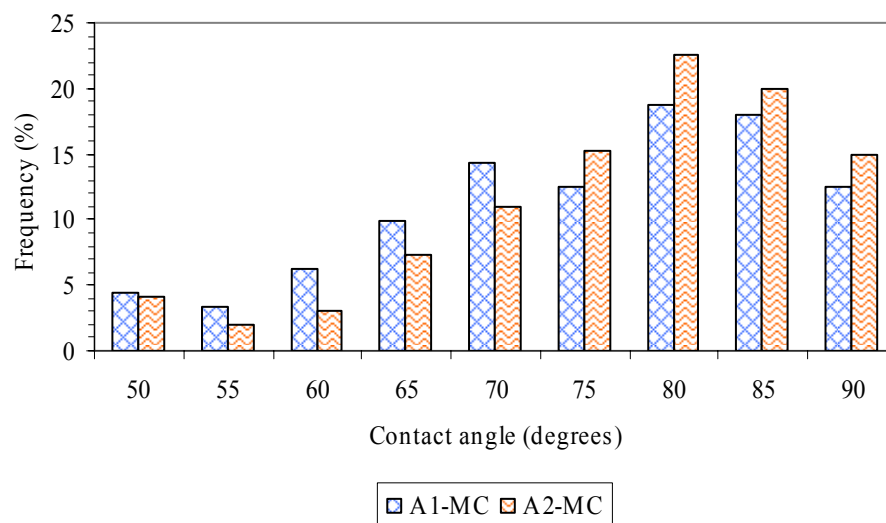
Figure 4.19. Histograms of the estimated contact angle for the mastic of the moisture conditioned samples

An average value of r, obtained using Equation 3.11 and the air voids filled with water after a wetting period of 36 days, was also used in Equation 4.4. The resulting estimated contact angle values are presented in Table 4.4. Consistent with the histograms of Figures 4.18 and 4.19, the estimated average contact angles show that the samples with less water seepage (*A1-MC*, *A2*, and *A2-MC)* were the ones with higher contact angle values, close to 70°. For the other samples *A1*, *B1*, and *B2*, in which water seepage was more evident, the contact angle values ranged between about 59° and 66°. The results also indicate that the higher the percent of air voids filled with water as presented in Figure 4.16, the lower the average value of the contact angle. Sample *B1* had the largest percent of air voids filled with water after 36 days of wetting, followed by sample *B2* and then *A1*. Consistent with these results, the average values for the contact angle were 59.2°, 63.4°, and 65.8°, respectively (Table 4.4).

Table 4.4. Estimated Average Contact Angles for the Mastic

Mix type	Contact angle (°)
A1	65.8
A1-MC	68.8
A2	71.2
A2-MC	70.5
B1	59.2
B2	63.4

These contact angle values show that the mastic coating the aggregates in the asphalt mix is capable of attracting water due to capillary rise. The analysis was completed assuming that capillary rise of water had reached equilibrium; however, as shown in Figure 4.16 and Table 4.3, some of the samples needed more time to achieve this state. If the capillary rise experiment had spanned a longer period, the estimated value of the contact angle would have been smaller than the ones presented in Table 4.4.

All the capillary results presented in this section were limited by the smallest air void size that can be captured by the image resolution. It is reasonable to assume that there are smaller air voids that would have capillary rise as well. To prove this, contact angles representing the values in Figures 4.18 and 4.19 were used to estimate the capillary rise of water in pores smaller than the horizontal image resolution (0.2 mm [0.0008 in]) as shown in Figure 4.20.
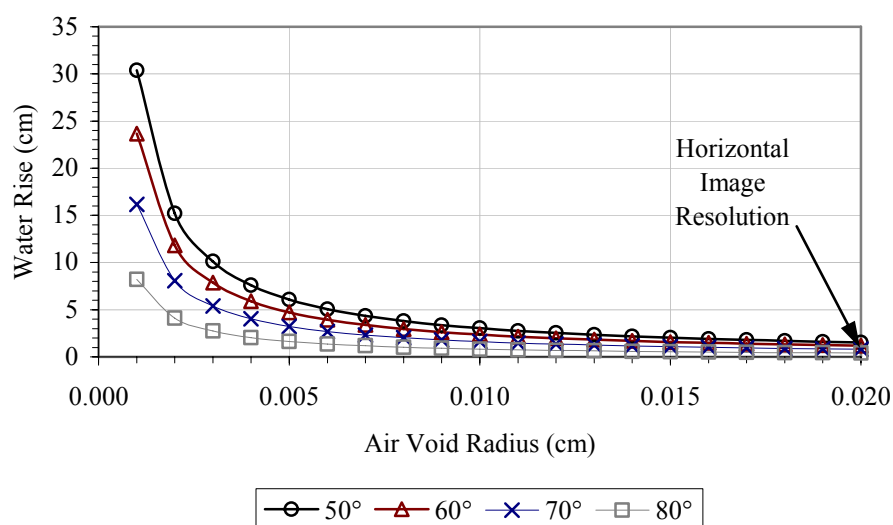
Figure 4.20. Level of water rise for different contact angles on air void sizes smaller than the horizontal image resolution

Figure 4.20 demonstrates that a higher rise than that measured in this study could occur in asphalt mixes. The implication of this water rise can be very important in terms of moisture damage because the water in these voids is more accessible to asphalt binder. Given the relative humidity gradient (or suction) between the voids filled with water and the asphalt-aggregate

interface, moisture would be driven by this gradient to diffuse through the binder or mastic film, ultimately causing debonding between the binder and the aggregate. The diffusion of moisture under a relative humidity gradient in asphalt mixes and mastics has been recently documented (Kassem et al. 2006).

Saturation Experiment and Results

At the end of the capillary rise experiment, all the samples were vacuum saturated. The level of saturation of the samples after about 60 s of vacuum was between 76 and 86 percent. The samples were kept in water and scanned while completely submerged as shown in Figure 4.21. The setup was the same as the one described before. The images of each saturated sample, acquired for the bottom 20 mm (0.8 in) of the sample height, were aligned and subtracted from the initial dry images to obtain the voids filled with water. The results were then compared to the connected voids in the bottom 20 mm (0.8 in) of the sample from the air void connectivity analysis (Table 4.2). These values of the connected voids and the water-saturated voids are presented in Table 4.5.

Figure 4.21. Saturated experiment setup during scanning

Table 4.5. Connected and Water-Saturated Air Voids in the Bottom 20 mm (0.8 in) of the Sample

Mix type	Connected air voids (%)	Water-saturated air voids (%)
A1	0.94	1.09
A1-MC	2.36	0.77
A2	1.28	0.57
A2-MC	2.04	0.49
B1	1.66	3.97
B2	0.58	1.69

These results lead to two observations. Samples *A1-MC*, *A2*, and *A2-MC* in which less capillary rise was measured had a smaller percentage of voids saturated with water compared to the percentage of connected voids. This proves that these connected voids were not accessible to moisture, probably because of their small size in the case of sample *A2* and the high relative humidity in the voids of the moisture conditioned samples in the case of samples *A1-MC* and *A2-MC*. In contrast, the other three samples, *A1*, *B1*, and *B2*, had values of saturated voids filled with water greater than the connected voids. This finding again suggests that some damage occurred during the saturation process, when water is forced into the pores by vacuum and is available from all sides of the sample.

CHAPTER V

DYNAMIC AND RELAXATION TESTS TO EXAMINE THE RESISTANCE TO MOISTURE DAMAGE

Dynamic and relaxation tests were used to estimate the moisture susceptibility of the samples prepared, conditioned, and characterized as described in Chapter III. The tests included in this study are a dynamic modulus test and a relaxation test in both direct tension and direct compression. Researchers have used the dynamic modulus test as a moisture sensitivity indicator on samples conditioned using the ECS (Solaimanian et al. 2006).

The specific goals were to:

a) assess the efficiency of dynamic and relaxation tests in evaluating the moisture susceptibility of asphalt mix samples with different air void structures conditioned using the modified Lottman procedure without the freezing step,

b) compare the compressive relaxation results to the tensile relaxation results, and

c) compare the compressive relaxation results to the dynamic test results using three different approximation methods to convert frequency-domain data (dynamic modulus) to time-domain data (relaxation modulus).

The dynamic test consisted of the application of a sinusoidal cyclic compressive load on the sample while maintaining the strain within a specific range; the relaxation test, performed in both direct tension and compression, consisted of the application of a static trapezoidal-shaped strain. A statistical analysis was used to study the effectiveness of the tests in differentiating between the conditioned and unconditioned response (dynamic modulus or relaxation modulus) and between the different mix types within each condition. The approximation methods used to convert the dynamic modulus data to time-domain data were the generalized Maxwell model, the Schapery and Park approximation, and the Ninomyia and Ferry interconversion.

The next section explains the protocols of the tests. Then, a section including the test data and statistical analysis is presented. Next, the analysis and comparison of different methods of approximation between frequency-domain data and time-domain data are included.

Test Protocols

The samples used for the dynamic modulus test were 150 mm (6 in) height gradation *A* samples and 100 mm (4 in) height (after trimming) gradation *A* and gradation *B* samples. For the

relaxation test, only trimmed samples of gradation *A* and gradation *B* mix types having a final height of 100 mm (4 in) were used. The properties of the materials and air void characteristics of these mix types were previously discussed in Chapter III. The test protocols are described next.

Relaxation Test

A servo-hydraulic testing machine was used to apply a static constant trapezoidal-shaped tensile strain level of 200 microstrain ($\mu\varepsilon$) for 60 s. After a rest period of 600 s, the sample was subjected to a similar static constant trapezoidal-shaped compressive strain of 200 $\mu\varepsilon$ as shown in Figure 5.1. The ramp of the trapezoidal-shaped strain spanned 6 s. The relaxation test was performed at 10 °C (50 °F), 20 °C (68 °F), and 30 °C (86 °F), starting with the lowest temperature. The samples were temperature-conditioned for at least 2 h before testing, and readings from a thermocouple probe inserted in a trial sample that was placed inside the temperature chamber were used for temperature monitoring purposes. The same sample replicate was used for all three temperatures, and three replicates were tested for each mix type and moisture condition.
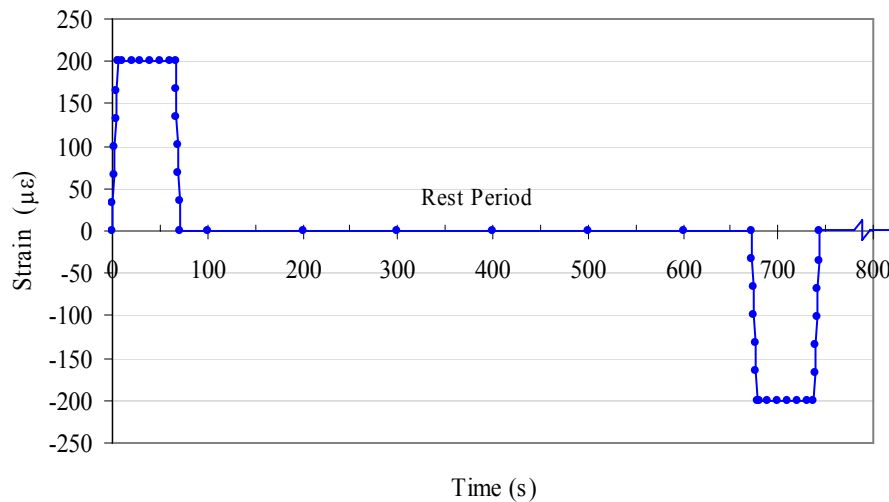
Figure 5.1. Loading protocol for the relaxation test

The strain-induced load was measured using three axial linear variable differential transducers (LVDT) attached at 120° from each other along the sample diameter as shown in Figure 5.2. The LVDT holders were attached using high strength glue and an accelerator, and samples were glued between two metal plates using high strength 2-ton epoxy glue as detailed in Appendix C. The distance between the LVDT holders was 50 mm (2 in) since the relaxation test was only performed on 100 mm (4 in) height samples. An environmental chamber was used to condition the samples and to maintain the target temperature during testing, while a trial sample with a thermocouple mounted at the center was used for temperature verification. Liquid nitrogen was used to reduce and maintain the temperature at 10 °C (50 °F). The sample was loaded and aligned with the vertical load axle. The LVDTs used to measure the load-induced displacements were placed and zeroed before the start of the test. The sample configuration inside the environmental chamber of the testing machine is presented in Figure 5.3.

Figure 5.2. Configuration of the LVDT holders

Figure 5.3. Sample setup for the tensile and compressive relaxation tests

Dynamic Modulus Test

A dynamic modulus test was conducted on the samples following the standard AASHTO procedure (AASHTO 2002b). A servo-hydraulic testing machine was used to apply a cyclic sinusoidal axial compressive load. The samples were tested at 21.1 °C (70 °F), 37.8 °C (100 °F), and 54.4 °C (130 °F), with loading frequencies at each temperature of 0.1, 0.5, 1, 5, 10, and 25 Hz. The same replicate sample was used for all three temperatures, and three replicates were tested for each mix type and moisture condition. An environmental chamber attached to the equipment was used to condition the samples and to maintain the target temperature during testing. A trial sample with a thermocouple mounted at the center was used for temperature verification. The tests were performed starting from the lowest temperature and proceeding to the highest. At any given temperature, the frequency sweep was done from the highest frequency to the lowest. The number of applied load cycles depended on the load frequency; 200 load cycles were applied for 25 and 10 Hz, 100 load cycles for 5 Hz, 20 load cycles for 1 Hz, and 10 load cycles for 0.5 and 0.1 Hz. A rest period of 30 s was allowed between each frequency test.

The load magnitude was adjusted in order to achieve an axial strain of between 50 $\mu\varepsilon$ and 150 $\mu\varepsilon$ and a cumulative permanent strain of no more than 1500 $\mu\varepsilon$. The load-induced displacements were measured using three LVDTs attached at 120° from each other along the sample diameter as shown previously in Figure 5.2. The distance between the LVDT holders for

the 150 mm (6 in) height samples was 100 mm (4 in) and for the 100 mm height samples was 50 mm (2 in). Details regarding the LVDT configuration are included in Appendix D. Static stress levels of 5 kPa (0.72 psi) for the 150 mm (6 in) height samples and of 2 kPa (0.29 psi) for the 100 mm (4 in) height samples were applied through the test. The dynamic stress levels, which are listed in Table 5.1, were estimated using trial samples to achieve the previously mentioned axial strain and cumulative strain requirements.

The samples were set between two loading plates, and an end treatment consisting of two 0.5 mm (0.02 in) thick latex membranes separated with silicone grease was used between the sample and the plates to reduce friction and minimize the end effects. The sample setup inside the test chamber is presented in Figure 5.4. A summary of both tests parameters is presented in Table 5.2.

Table 5.1. Dynamic Stress Levels in kPa for the Dynamic Modulus Test

Sample height (mm)	Temperature (°C)	Frequencies (Hz)					
		25	10	5	1	0.5	0.1
150	21.1	200	120	120	100	100	75
	37.8	25	15	15	15	10	10
	54.4	10	8	8	5	5	5
100	21.1	150	120	120	100	100	75
	37.8	15	12	12	10	5	5
	54.4	10	8	8	5	5	5

Table 5.2. Relaxation Test and Dynamic Modulus Test Parameters

Test	Load shape	Load duration/cycles	Rest period	Strain level ($\mu\varepsilon$)	Temperature (°C)	Frequency (Hz)
Relaxation	Trapezoidal	6 s – ramp 60 s – steady	600 s	~200	10, 20, 30	N/A
Dynamic modulus	Sinusoidal	200, 20, or 15 cycles depending on frequency	None	50 - 150	21, 38, 54	0.1, 0.5, 1, 5, 10, 25

Figure 5.4. Sample setup for the dynamic modulus test inside the environmental chamber of the testing equipment

Data Analysis and Statistical Results

Relaxation Test

The relaxation test was only performed on the 100 mm (4 in) height samples. The magnitude of the load measured during the tensile and compressive relaxation tests was used to compute the time-dependent relaxation modulus as follows:

$$E(t) = \frac{P(t)}{\pi r^2 \varepsilon} \tag{5.1}$$

where $E(t)$ is the time-dependent relaxation modulus, $P(t)$ is the measured load, r is the radius of the sample, and ε is the target tensile strain $\varepsilon = 200 \ \mu\varepsilon$.

A power law equation was used to generate a master curve in order to fit the time-dependent relaxation modulus acquired at the three different temperatures to a single reference temperature as follows:

$$E(t) = E_1 t_{red}^{-m} \tag{5.2}$$

where $E(t)$ is the time-dependent relaxation modulus at the reference temperature, E_1 is the initial relaxation modulus when the reduced time $t_{red} = 1$ s, and m is the relaxation rate. The reduced time was computed as:

$$t_{red} = \frac{t}{\log(a_T)} \tag{5.3}$$

where t is the elapsed time and a_T is the temperature shift factor. To estimate the temperature shift factors, the relaxation modulus results at 10 °C (50 °F) and 30 °C (86 °F) were shifted to a reference temperature of 20 °C (68 °F) using the Arrhenius equation (Medani et al. 2004):

$$\log(a_T) = \log(e)\left(\frac{\Delta H}{R}\right)\left(\frac{1}{T} - \frac{1}{T_{ref}}\right) \tag{5.4}$$

where T is the test temperature, T_{ref} is the reference temperature, ΔH is the activation energy, and R is the gas constant = 8.314 J/(mol K). The values for E_1, m, and ΔH were obtained by minimizing the sum of squared errors between the measured and estimated relaxation modulus obtained using Equations 5.1 and 5.2, respectively.

Several authors have compared the results of the Arrhenius equation against the results of other approaches, such as the Williams-Landel-Ferry (WLF) (Medani and Huurman 2003; Medani et al. 2004). One of the conclusions is that if the difference between the temperatures to be shifted, T, and the reference temperature, T_{ref}, is less than 20 °C (68 °F), the Arrhenius equation gives a better fit. On the other hand, if the difference between the temperatures ($T - T_{ref}$) is more than 20 °C (68 °F), the WLF method provides better results (Medani et al. 2004). In addition, as part of the Strategic Highway Research Program (SHRP), several asphalt mixes were analyzed using the Arrhenius equation (Equation 5.4). The results show that the average value of the activation energy for flow below the reference temperature was equal to 261kJ/mol (Christensen and Anderson 1992).

Other researchers have defined a constant related to the Arrhenius equation as:

$$C = \log(e)\left(\frac{\Delta H}{R}\right) \tag{5.5}$$

and reported values of C in the range of 7,680K to 13,060K (Medani and Huurman 2003). The values of ΔH, C, $E1$, and m for each mix type for the results in both tension and compression shifted to a reference temperature of 20 °C (68 °F) are listed in Table 5.3. Plots of the relaxation modulus results are shown in Figures 5.5 through 5.8. For the tensile test results, the values of the activation energy for gradation A samples were around 217 kJ/mol, and the values of the constant C were close to 11,348 K. In the case of the gradation B samples, the values of the

activation energy and constant C were around 333kJ/mol and 17,438K, respectively, somewhat higher than the ones reported in the literature.
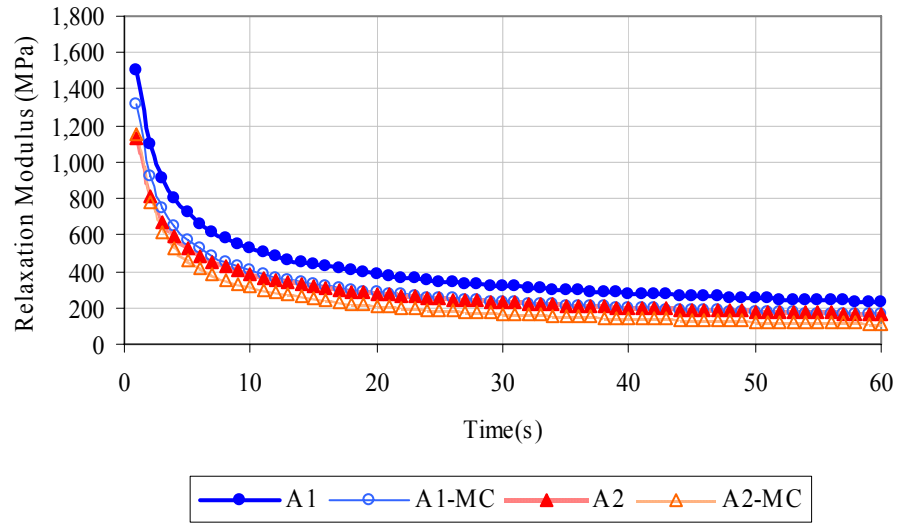
Figure 5.5. Tensile relaxation modulus test results for mix type A
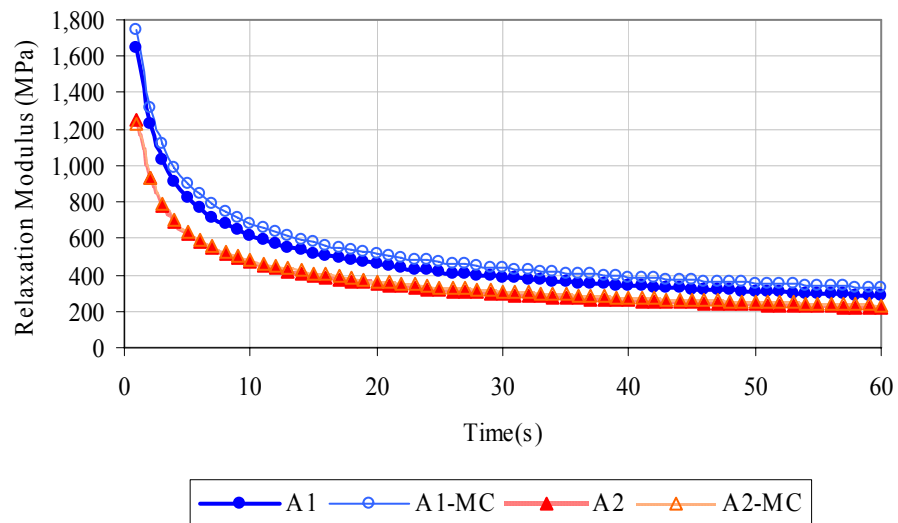
Figure 5.6. Compressive relaxation modulus for mix type A
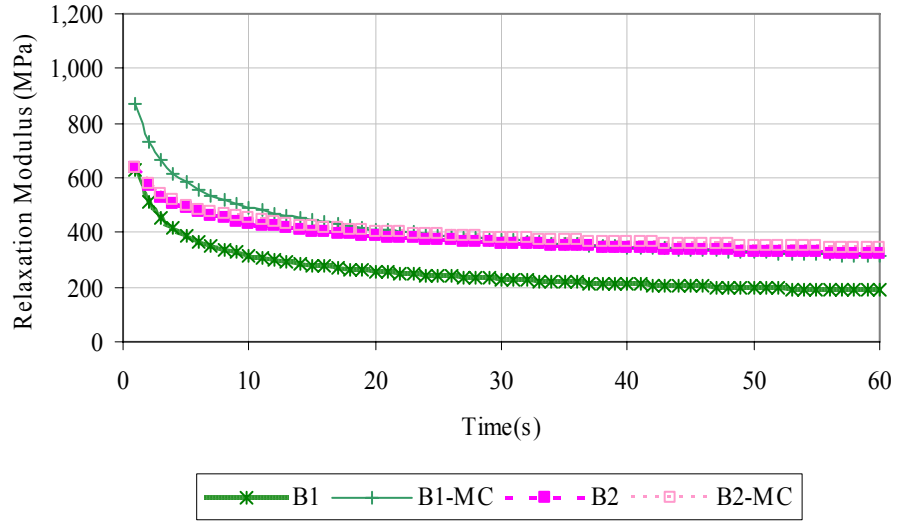
Figure 5.7. Tensile relaxation modulus for mix type *B*
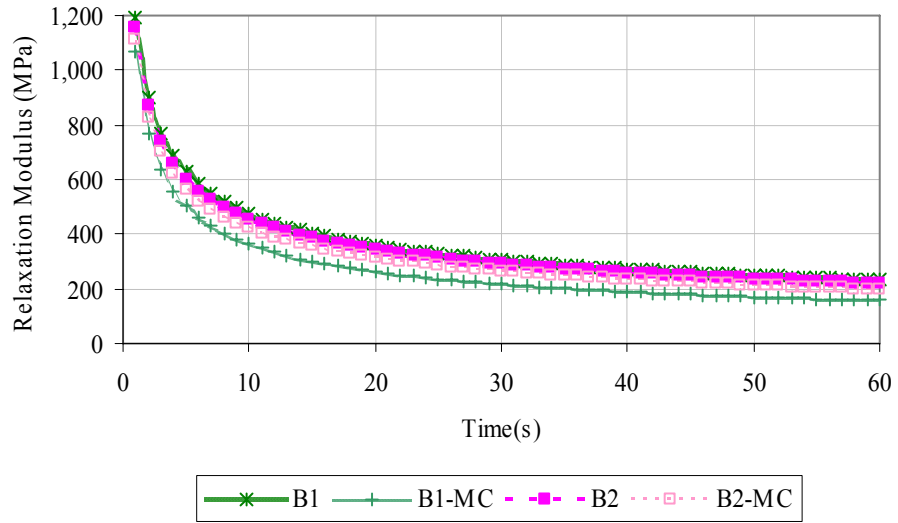
Figure 5.8. Compressive relaxation modulus for mix type *B*

Table 5.3. Tensile and Compressive Relaxation Modulus Test Parameters

	Tensile				Compressive			
Mix type	ΔH (J/mol)	C (K)	E_1 (MPa)	m	ΔH (J/mol)	C (K)	E_1 (MPa)	m
A1	218,403	11,409	1,509	0.46	245,743	12,837	1,650	0.43
A1-MC	215,116	11,237	1,317	0.51	215,119	11,237	1,743	0.41
A2	214,646	11,212	1,128	0.47	246,464	12,874	1,247	0.43
A2-MC	220,835	11,536	1,150	0.56	241,310	12,605	1,227	0.40
B1	404,990	21,155	628	0.30	239,485	12,510	1,192	0.40
B1-MC	302,512	15,802	874	0.25	188,325	9,838	1,065	0.47
B2	266,199	13,905	637	0.17	91,742	4,792	1,156	0.41
B2-MC	361,616	18,890	638	0.15	82,922	4,332	1,112	0.42

To assess the effectiveness of each test in differentiating between the unconditioned and conditioned response, a two-sample t-test was conducted. The null hypothesis, H_o, and the alternative hypothesis, H_a, were constructed as follows:

$$H_o : \mu_{dry} - \mu_{MC} = 0 \tag{5.6}$$

$$H_a : \mu_{dry} - \mu_{MC} \neq 0 \tag{5.7}$$

where μ_{dry} is the mean or true average response of the unconditioned results and μ_{MC} is the mean or true average response of the moisture conditioned results. Therefore, the t-test observes the difference between the average responses and estimates the probability or p-value, which is the smallest level of significance at which H_o can be rejected. The hypothesis test is based on comparing the p-value against a selected significance threshold level called α; if the p-value is less than α, H_o is rejected in favor of H_a. In this study, α was set to 0.05 or 5 percent. Statisticians often call the data 'significant' when H_o is rejected and 'not significant' otherwise (Devore 2000). Table 5.4 shows the statistical results of the comparisons between the unconditioned and conditioned responses of the different mix types, as well as the conclusions of the hypothesis tests.

Table 5.4. Results of the *t*-test Analysis Comparing the Unconditioned and Conditioned Response of the Tensile and Compressive Relaxation Test Results

Mix type	Tensile		Compressive	
	p-value	Hypothesis test	p-value	Hypothesis test
A1 versus *A1-MC*	0.0147	Reject H_o	0.2297	Accept H_o
A2 versus *A2-MC*	0.0680	Accept H_o	0.6478	Accept H_o
B1 versus *B1-MC*	0.0000	Reject H_o	0.0032	Reject H_o
B2 versus *B2-MC*	0.1001	Accept H_o	0.3702	Accept H_o

The implication of rejecting H_o is that the test was able to detect differences between the conditioned and unconditioned response. Therefore, in this context, it is desirable to reject H_o in order to consider the test suitable to distinguish between the two conditions. Based on Table 5.4 the tensile relaxation test for mixes *A1* and *B1* showed differences between the responses, while for the compressive test only the differences for mix *B1* were significant.

A statistical analysis of variance (ANOVA) was also performed to observe if the relaxation test was able to find differences between the different types of mixes within each condition. In this case the null and alternative hypotheses were:

$$H_o : \mu_{A1} = \mu_{A2} = \mu_{B1} = \mu_{B2} \tag{5.8}$$

$$H_a : \text{at least two of the } \mu_i\text{'s are different} \tag{5.9}$$

For this analysis, the test statistic or *F*-value is used to evaluate the differences in variation between the samples to the variation within each sample. Based on the number of samples, a probability is also computed, which is then compared against the selected significance threshold level ($\alpha = 0.05$ in this study) to conclude if the data are significant. When H_o is rejected, it is also relevant to determine which μ_i's are different from one another. A method for performing this further analysis is Tukey's honestly significant differences (HSD) for multiple comparisons. In Table 5.5, the results of the ANOVA and multiple comparisons are presented. For both conditions, the test was able to capture the difference between the different mix types. The results of the multiple comparisons are presented in parentheses, grouping the mixes with same mean values.

Table 5.5. ANOVA and Multiple Comparisons Results for the Tensile and Compressive Relaxation Results

| Mix condition | Tensile | | | Compressive | | |
	F-value	Hypothesis test	Multiple comparisons	F-value	Hypothesis test	Multiple comparisons
Unconditioned	12.202	Reject H_o	(A1, B2) (A2, B1)	4.903	Reject H_o	(A1) (A2, B1, B2)
Conditioned	20.536	Reject H_o	(A1, A2) (B1, B2)	18.703	Reject H_o	(A2) (A2, B2) (B1, B2)

Based on the results presented in Table 5.4 it is evident that the tensile and compressive relaxation tests are inconsistent in terms of differentiating the responses of the unconditioned versus the conditioned samples. Also, based on the ANOVA and multiple comparisons (Table 5.5) it is apparent that these tests are not effective in consistently differentiating between the different mix types. However, the multiple comparison results for the tensile tests seem to provide better results, with only two separate groups for each mix condition.

Dynamic Modulus Test

The dynamic test was performed on gradation A 150 mm (6 in) height samples and also on gradation A and B samples with a height of 100 mm (4 in). The test control, data acquisition, and software used during testing were developed by Industrial Process Controls Ltd. (IPC). The dynamic modulus and phase angle values were estimated as follows (AASHTO 2003a):

$$\sigma_0 = \frac{\overline{P}}{A} \tag{5.10}$$

where σ_o is the loading stress, $\overline{P}$ is the average peak load over the last five load cycles, and A is the area of the sample. Then, the strain is calculated as follows:

$$\varepsilon_0 = \frac{\overline{\Delta}}{GL} \tag{5.11}$$

where $\overline{\Delta}$ is the average peak deformation over the last five load cycles, and GL is the gauge length equal to 100 mm (4 in) for the gradation A 150 mm (6 in) height samples and to 50 mm (2 in) for the gradation A and B 100 mm (4 in) height samples. Finally, the dynamic modulus is estimated as:

$$\left|E^*\right| = \frac{\sigma_0}{\varepsilon_o} \tag{5.12}$$

The phase angle in degrees is estimated also using the data over the last five load cycles for each test condition as follows:

$$\phi = 360\left(\frac{t_i}{t_p}\right) \tag{5.13}$$

where t_i is the average lag time between a cycle of stress and strain, and t_p is the average time for a stress cycle.

After estimating the values of dynamic modulus for each frequency and test temperature, a sigmoidal function was employed to fit the time-dependent dynamic modulus (ARA 2004):

$$\log(E^*) = \delta + \frac{\alpha}{1 + e^{\beta + \gamma(\log t_r)}} \tag{5.14}$$

where E^* is the dynamic modulus, δ is the minimum value of E^*, $(\delta + \alpha)$ is the maximum value of E^*, β and γ are the parameters that describe the shape of the sigmoidal function, and t_r is the time of loading at the reference temperature. The difference in the values of δ and α are usually associated with the aggregate gradation, binder content, and air void content, while the β and γ parameters depend on the characteristics of the asphalt binder (ARA 2004). The value of t_r was estimated as follows:

$$\log(t_r) = \log\left(\frac{t}{a_T}\right) \tag{5.15}$$

where t is the time of loading at any given temperature, and a_T is the temperature shift factor. The time is computed as the inverse of the loading frequency: $t = 1/\omega$. To obtain the shift factors and build the master curve, the results at 37.8 °C (100 °F) and 54.4 °C (130 °F) were shifted to a reference temperature of 21.1 °C (70 °F). The values for δ, α, β, and γ, as well as the shift factors, a_T, were obtained by numerical optimization where the sum of squared errors between the measured dynamic modulus values and the estimated values obtained using Equation 5.14 were minimized. The values of the fitting parameters and shift factors for each mix type are presented in Table 5.6, and the fitted curves appear in Figures 5.9 through 5.11.

Table 5.6. Dynamic Modulus Test Parameters and Temperature Shift Factors

Sample height (mm)	Mix type	δ	α	β	γ	$a_{(37.8 °C)}$	$a_{(54.4 °C)}$
150	*A1*	3.55	3.50	-0.81	0.33	-2.15	-3.99
	A2-MC	3.82	2.83	-0.99	0.47	-2.21	-3.79
	A2	3.53	3.09	-1.01	0.46	-1.90	-3.44
	A2-MC	4.02	2.47	-0.94	0.58	-2.10	-3.31
100	*A1*	2.65	4.65	-1.15	0.25	-3.31	-4.51
	A2-MC	2.58	4.65	-1.05	0.24	-2.92	-3.97
	A2	3.00	4.75	-0.58	0.20	-3.07	-4.44
	A2-MC	3.09	4.86	-0.45	0.17	-3.87	-5.09
	B1	3.29	4.15	-0.48	0.28	-2.37	-3.42
	B1-MC	2.89	4.13	-0.98	0.34	-2.01	-3.15
	B2	3.44	4.22	-0.05	0.32	-1.38	-2.10
	B2-MC	3.89	4.32	0.19	0.31	-2.11	-3.05
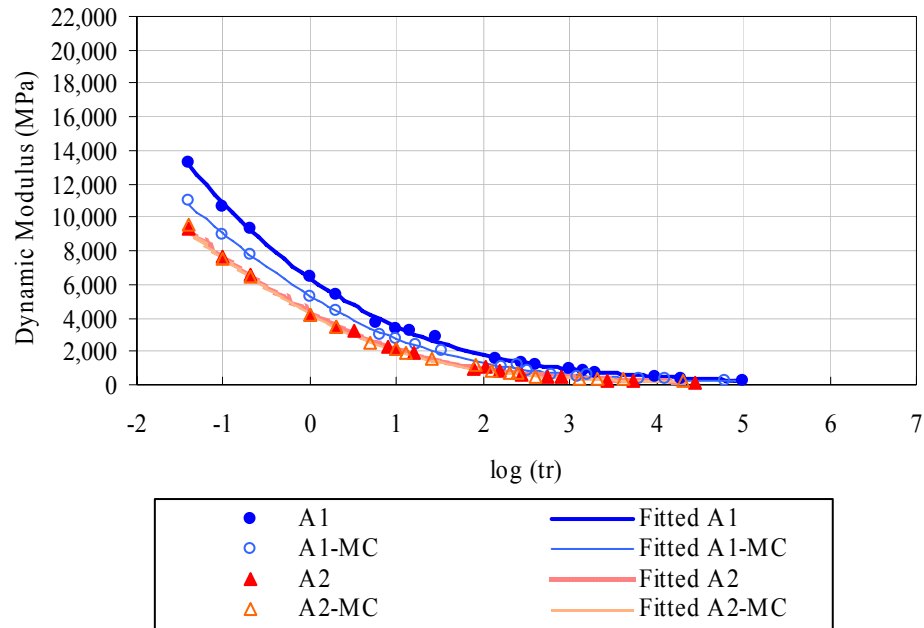
Figure 5.9. Dynamic modulus for the mix type *A* 150 mm (6 in) height samples
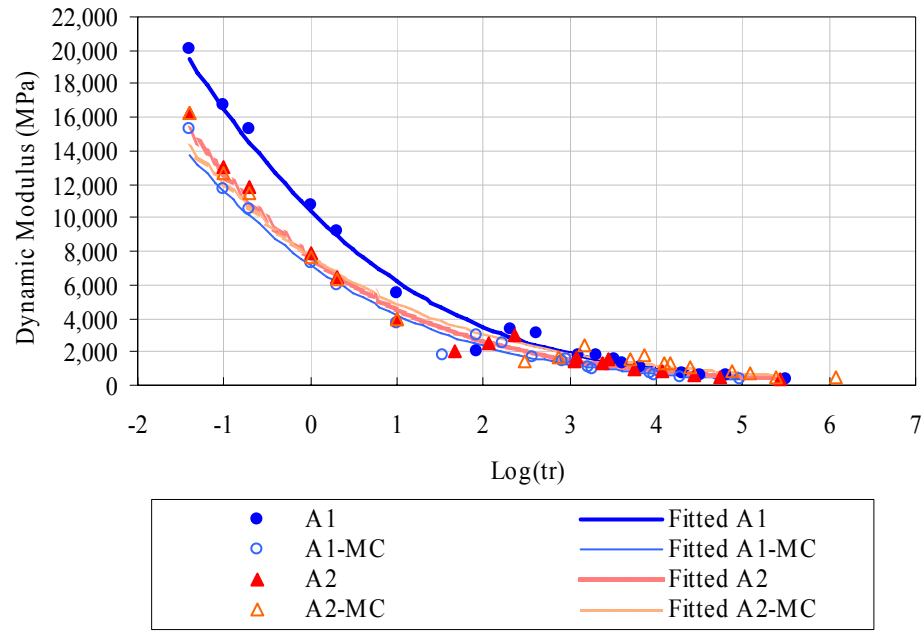
Figure 5.10. Dynamic modulus for mix type *A* 100 mm (4 in) height samples
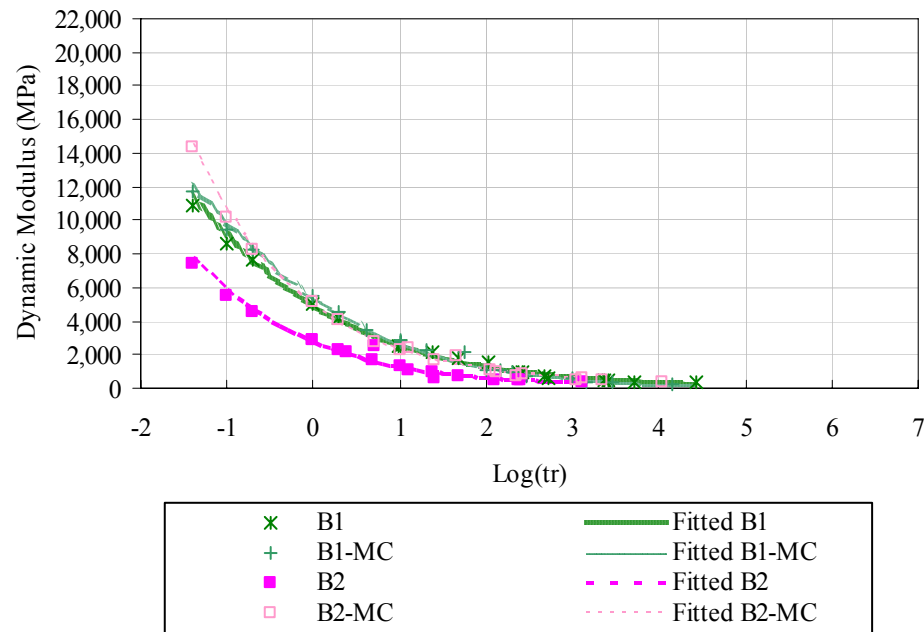
Figure 5.11. Dynamic modulus for mix type *B* 100 mm (4 in) height samples

The effectiveness of the dynamic test to differentiate between the unconditioned and moisture conditioned response was assessed using the statistical *t*-test presented in the previous section. The null and alternative hypothesis considered were the same ones presented in Equations 5.6 and 5.7. Table 5.7 shows the statistical results of the comparisons between the unconditioned and conditioned response of the different mix types, as well as the conclusions of the hypothesis tests. The only cases in which the dynamic test was able to distinguish between the unconditioned and conditioned results were for the 100 mm (4 in) height samples *A1* and *B2*. None of the 150 mm (6 in) height samples' tests showed differences between the responses.

An ANOVA was also performed to observe if the relaxation test was able to find differences between the different mix types within each condition. The null and alternative hypotheses considered are the same ones presented previously in Equations 5.8 and 5.9. In Table 5.8, the results of the ANOVA and multiple comparisons are presented. Only the 100 mm (4 in) height unconditioned samples showed differences in the response of the different mix types. For the other cases, the difference between the responses of the different mix types was not significant.

Table 5.7. Results of the *t*-test Analysis Comparing the Unconditioned and Conditioned Response of the Dynamic Modulus Test

Sample height (mm)	Mix type	*p*-value	Hypothesis Test
150	*A1 vs. A1-MC*	0.2480	Accept H_o
	A2 vs. A2-MC	0.9711	Accept H_o
100	*A1 vs. A1-MC*	0.0276	Reject H_o
	A2 vs. A2-MC	0.7646	Accept H_o
	B1 vs. B1-MC	0.7299	Accept H_o
	B2 vs. B2-MC	0.0050	Reject H_o

Table 5.8. ANOVA and Multiple Comparisons Results for the Dynamic Modulus Test

Sample height (mm)	Mix Condition	*F*-value	Hypothesis test	Multiple comparisons
150	Unconditioned	2.785	Accept H_o	-
	Conditioned	0.332	Accept H_o	-
100	Unconditioned	9.053	Reject H_o	(A1, A2) (A2, B1) (B1, B2)
	Conditioned	1.118	Accept H_o	-

Based on the statistical results of Tables 5.7 and 5.8 we can conclude that the dynamic test was not consistent in differentiating between the unconditioned and conditioned response and between the responses of different mix types. If only 150 mm (6 in) height samples were tested, according to the AASHTO standard, none of the mixes would have been significant. In addition, when comparing the 100 mm (4 in) height sample results to the ones presented previously for the tensile and compressive relaxation modulus (Tables 5.4 and 5.5), the conclusions obtained for each one of the statistical tests are different.

Approximation Methods

Several approximation methods were used to convert the frequency-domain data acquired during the dynamic modulus test to time-domain data. The results at each temperature (21.1 °C [70 °F], 37.8 °C [100 °F], and 54.4 °C [130 °F]) were converted to time-domain using three different methods: generalized Maxwell model, Schapery and Park approximation, and Ninomiya and Ferry interconversion. Then, the results were fitted to a master curve using the Arrhenius approach (Equations 5.2 through 5.4). The results of these methods were compared to the relaxation compressive master curve fitted to a reference temperature of 20 °C (68 °F). Each approximation method is explained subsequently, followed by the statistical analysis of the results.

Generalized Maxwell Model

The generalized Maxwell model consists of a series of n individual units of springs and dashpots as shown in the schematic of Figure 5.12, where the relaxation properties for the spring and the dashpot are E and $\eta \cdot$s, respectively.
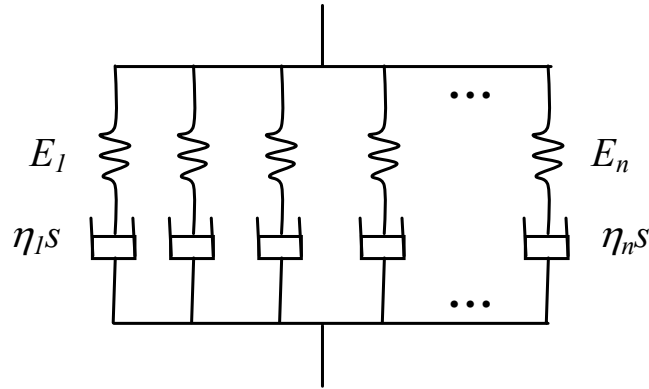
Figure 5.12. Schematic of the generalized Maxwell model

The data collected at any given temperature are fitted by minimizing the following objective function:

$$f(E) = \sum_{j=1}^{m} \left(\left[\frac{E'(\omega_j)}{E'^o(\omega_j)} - 1 \right]^2 + \left[\frac{E''(\omega_j)}{E''^o(\omega_j)} - 1 \right]^2 \right)$$ (5.16)

where m is the total number of frequencies used in the test, $E'^o(\omega_j)$ is the measured storage modulus, $E''^o(\omega_j)$ is the measured loss modulus, $E'(\omega_j)$ is the estimated storage modulus, and $E''(\omega_j)$ the estimated loss modulus. To calculate the measured storage and loss modulus at any given frequency, j, the following relationships are used:

$$E'(\omega) = E^*(\omega)\cos\phi$$ (5.17)

$$E''(\omega) = E^*(\omega)\sin\phi$$ (5.18)

where E^* is the complex dynamic modulus and ϕ is the phase angle.

Using the Laplace transformation, the expression to estimate the retardances of a single i^{th} spring and dashpot unit is as follows:

$$\overline{Q}_i(s) = \frac{1}{\overline{U}_i(s)} = \frac{1}{J_i + \phi_i s} = \frac{1}{(1/E_i) + (1/\eta_i s)} = \frac{\eta_i s}{1 + \dfrac{\eta_i s}{E_i}}$$ (5.19)

Defining $\tau_{mi} = \dfrac{\eta}{E}$ transforms Equation 5.19 to:

$$\overline{Q}_i(s) = \frac{E_i\,\tau_{m_i}\,s}{1+\tau_{m_i}s} \tag{5.20}$$

Since the Maxwell model consists of a series of n springs and dashpots in parallel the total value of $\overline{Q}(s)$ corresponds to the addition of the individual values for each unit:

$$\overline{Q}(s) = \sum_{i=1}^{n}\overline{Q}_i(s) = \sum_{i=1}^{n}\frac{E_i\,\tau_{m_i}\,s}{1+\tau_{m_i}s} \tag{5.21}$$

replacing s by $j\omega$ to find E^* as a function of ω:

$$E^*(\omega) = \sum_{i=1}^{n}\overline{Q}_i(j\omega) = \sum_{i=1}^{n}\frac{E_i\,\tau_{m_i}\,j\omega}{1+\tau_{m_i}j\omega} \tag{5.22}$$

and multiplying by $\dfrac{(1-E_i\,\tau_{m_i}\,j\omega)}{(1-E_i\,\tau_{m_i}\,j\omega)}$:

$$E^*(\omega) = \sum_{i=1}^{n}\left(\frac{E_i\,\tau_{m_i}^2\,\omega^2}{1+\tau_{m_i}^2\,\omega^2}\right) + j\sum_{i=1}^{n}\left(\frac{E_i\,\tau_{m_i}\,\omega}{1+\tau_{m_i}^2\,\omega^2}\right) \tag{5.23}$$

which is also equivalent to:

$$E^*(\omega) = E'(\omega) + jE''(\omega) \tag{5.24}$$

Therefore, Equation 5.23 was used to estimate $E'(\omega)$ and $E''(\omega)$, which were then used to estimate and minimize the objective function presented in Equation 5.16. Finally, when the number of units of springs and dashpots that minimize the objective function was determined, the following equation was used to estimate the dynamic modulus as a function of time with $t = 1/\omega$:

$$E(t) = \sum_{i-1}^{n}E_i\,\exp\left(\frac{-t}{\tau_{m_i}}\right) \tag{5.25}$$

The results at each temperature were then shifted to a reference temperature of 21.1 °C (70 °F) using the power law and the Arrhenius equation (Equations 5.2 to 5.4). These results (labeled Max in Figures 5.13 through 5.16) were then compared against those obtained from the relaxation compressive master curve, fitted to a reference temperature of 20 °C (68 °F). The values of the relaxation modulus (labeled Arr in Figures 5.13 through 5.16) correspond to the ones previously presented in Figures 5.6 and 5.8, with the difference that in the case of Figure 5.13 through 5.16 the scale is logarithmic.
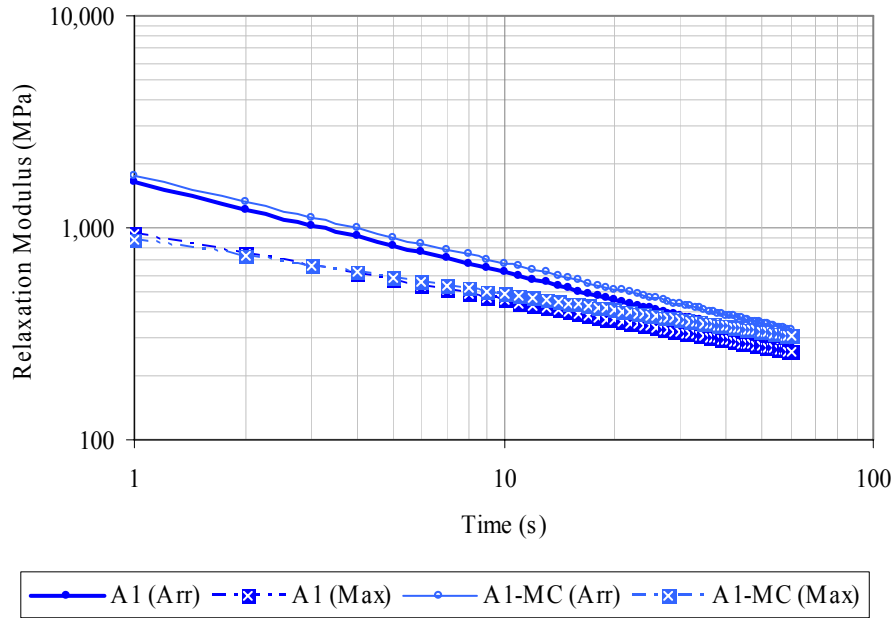
Figure 5.13. Comparison between the compressive relaxation modulus results and the general Maxwell model results for mix type *A1*
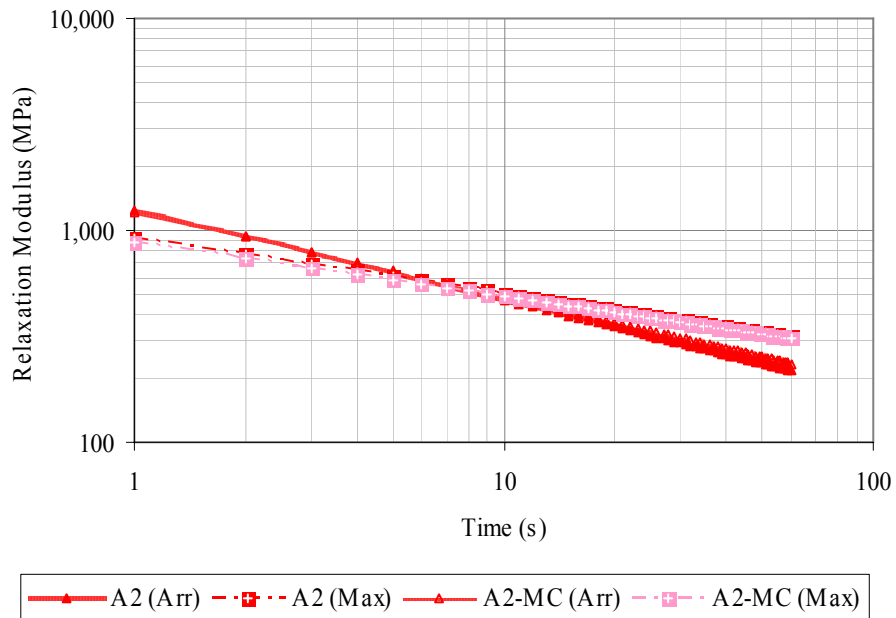
Figure 5.14. Comparison between the compressive relaxation modulus results and the general Maxwell model results for mix type *A2*
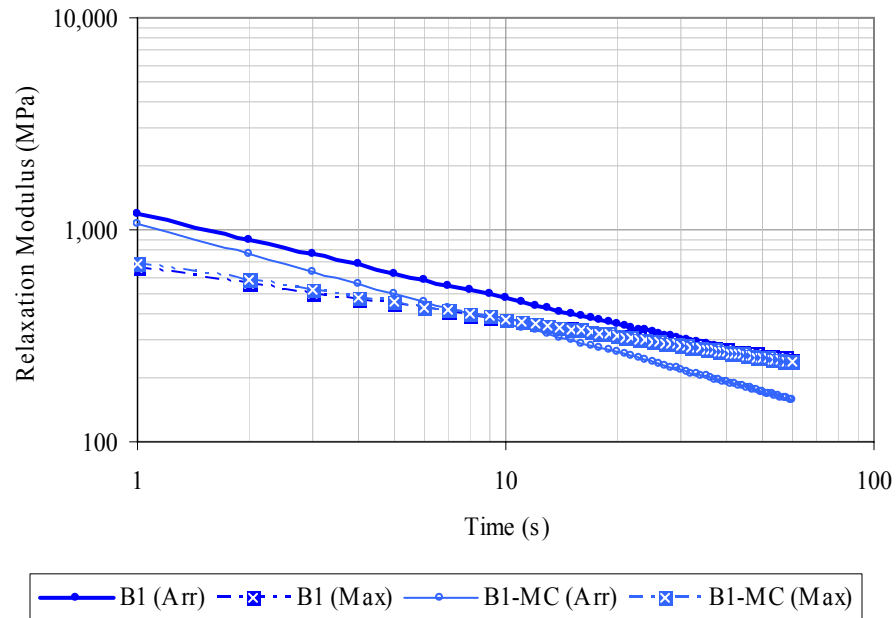
Figure 5.15. Comparison between the compressive relaxation modulus results and the general Maxwell model results for mix type *B1*
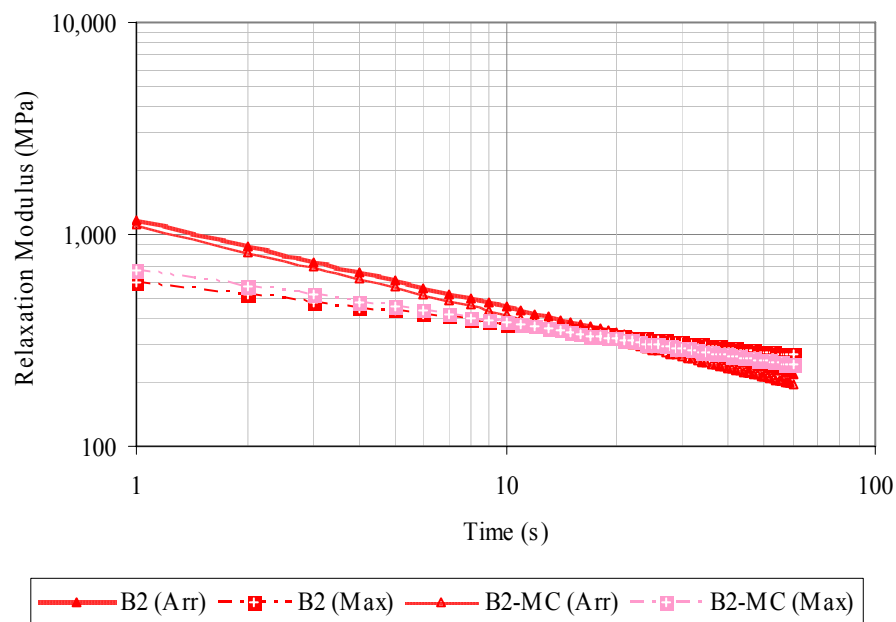
Figure 5.16. Comparison between the compressive relaxation modulus results and the general Maxwell model results for mix type *B2*

Schapery and Park Approximation

Schapery and Park (1999) presented different methods to characterize asphalt mixes subjected to uniaxial tension tests. Among others, they proposed an approximate relationship between storage modulus and relaxation modulus as follows:

$$E(t_r) = \frac{1}{\lambda'} E'(\omega_r)\bigg|_{\omega_r = (1/t_r)} \tag{5.26}$$

where ω_r is the reduced frequency, t_r is the reduced time, $E'(\omega r)$ is the storage modulus, and $E(t_r)$ is the relaxation modulus at any given temperature. The adjustment function λ' is defined as:

$$\lambda' = \Gamma(1-n)\cos\left(n\frac{\pi}{2}\right) \tag{5.27}$$

where Γ is the gamma function, and n is the log-log slope of the storage modulus with respect to the reduced frequency:

$$n = \frac{d\log(E'(\omega_r))}{d\log(\omega_r)} \tag{5.28}$$

The use of the adjustment function, λ', is recommended when n is smaller than 1, which means that this approximation is not valid for data acquired at very low frequencies (Schapery and Park 1999). The dynamic modulus results at each temperature were analyzed using this approach to estimate the relaxation modulus as a function of time. Then, the results at each temperature were shifted to a reference temperature of 21.1 °C (70 °F) using the power law and the Arrhenius equation (Equations 5.2 to 5.4). The estimated data were then compared against the relaxation compressive master curve, fitted to a reference temperature of 20 °C (68 °F). Figures 5.17 through 5.20 present the plots of the estimated values (labeled S&P) and the relaxation modulus values (labeled Arr). The values of the relaxation modulus correspond to the ones previously presented in Figure 5.6 and 5.8, with the difference that in this case the scale is logarithmic.
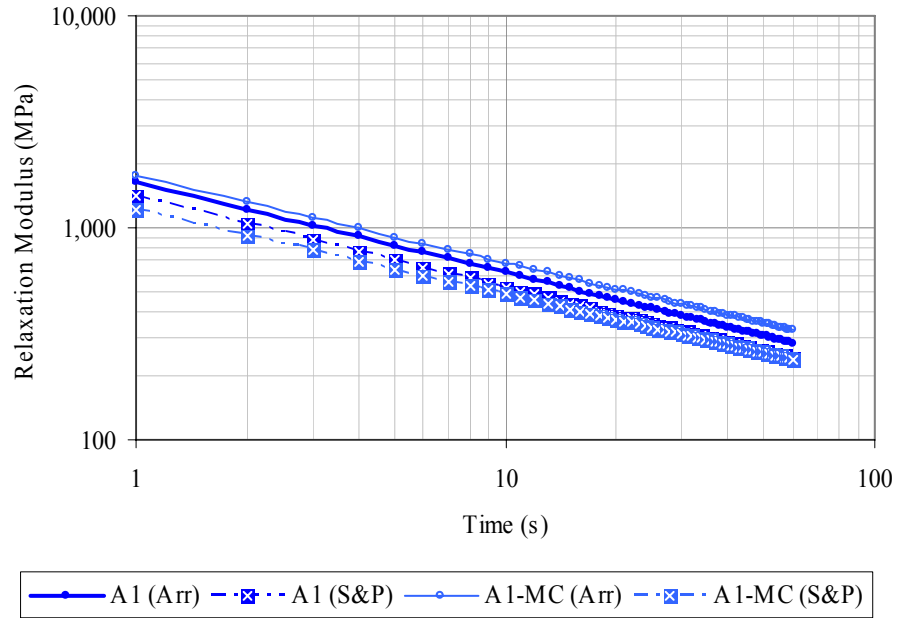
Figure 5.17. Comparison between the compressive relaxation modulus results and the Shapery and Park approximation for mix type *A1*
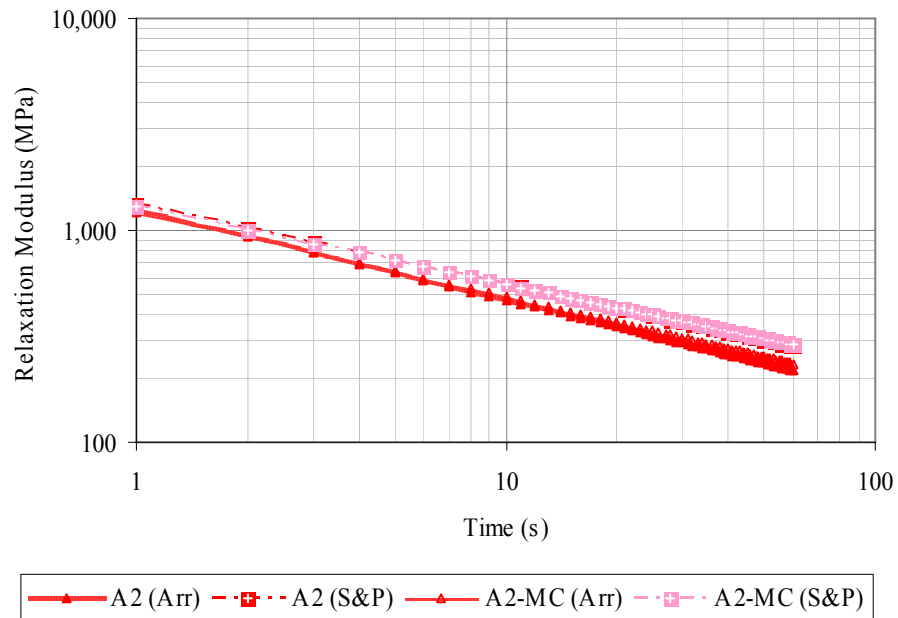
Figure 5.18. Comparison between the compressive relaxation modulus results and the Schapery and Park approximation for mix type *A2*
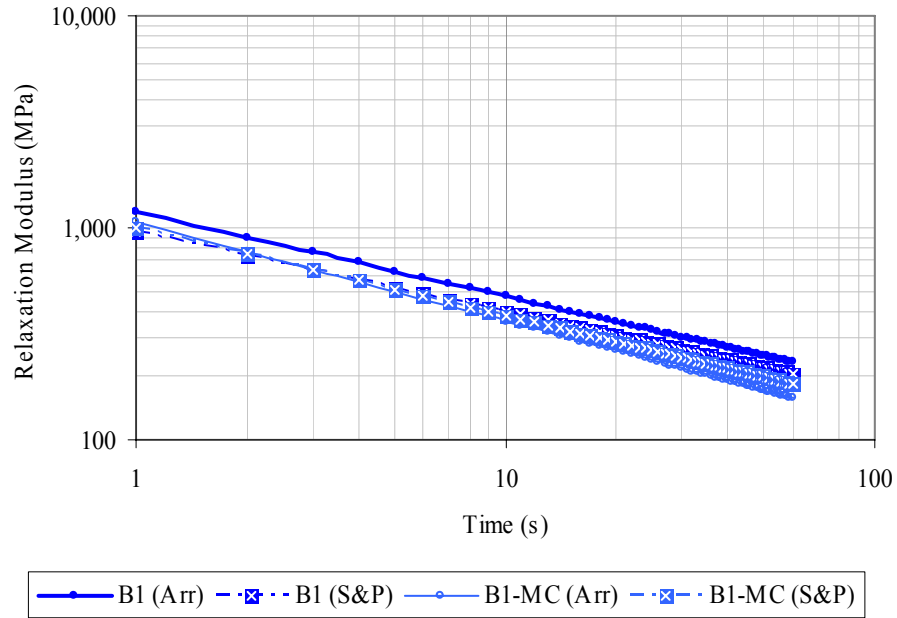
Figure 5.19. Comparison between the compressive relaxation modulus results and the Schapery and Park approximation for mix type *B1*
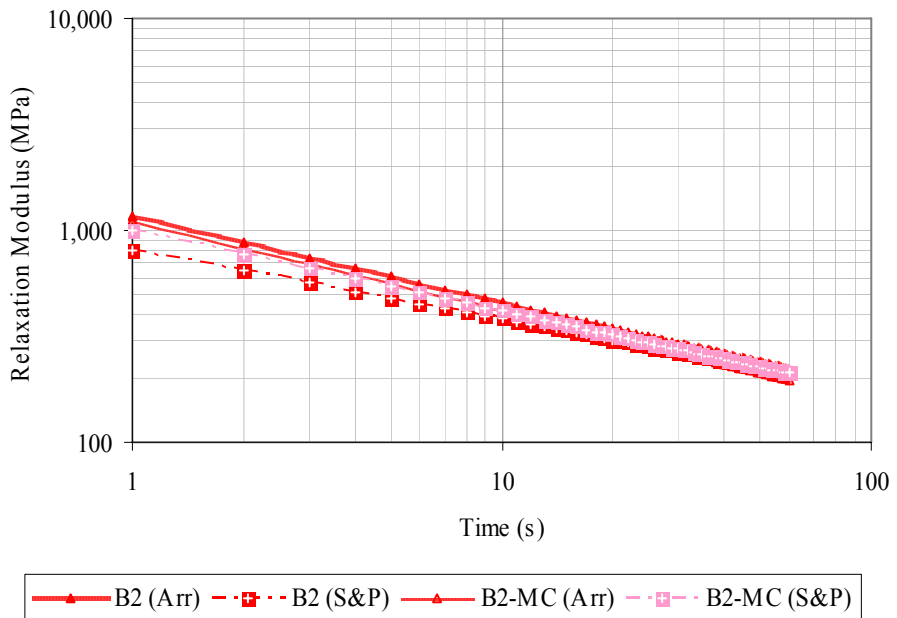
Figure 5.20. Comparison between the compressive relaxation modulus results and the Schapery and Park approximation for mix type *B2*

Ninomiya and Ferry Interconversion

Ninomiya and Ferry (1959) explored the interrelationships between linear viscoelastic functions and estimated relaxation values from several values of the real and imaginary components of the complex modulus (E' and E'') as an alternative method to differentiation. The proposed approximation is as follows:

$$E'(\omega) - E(t)\big|_{t=1/\omega} \cong 0.4E''(0.4\omega) - 0.14E''(10\omega) \tag{5.29}$$

A plot of ω in units of rad/s versus E'' was created to estimate the values of $E''(0.4\omega)$ and $E''(10\omega)$. In addition, the values of E' and E'' were computed according to Equations 5.17 and 5.18. This analysis was performed on the dynamic modulus values acquired at every temperature. Then, the results were shifted to a reference temperature of 21.1 °C (70 °F) using the power law and the Arrhenius equation presented previously in Equations 5.2 to 5.4. These results (labeled N&F in Figures 5.21 through 5.24) were then compared against the ones obtained from the relaxation compressive master curve (labeled Arr in Figures 5.21 through 5.24), fitted to a reference temperature of 20 °C (68 °F). The values of the relaxation modulus correspond to the ones presented in Figures 5.6 and 5.8, with the difference that the scale is logarithmic.
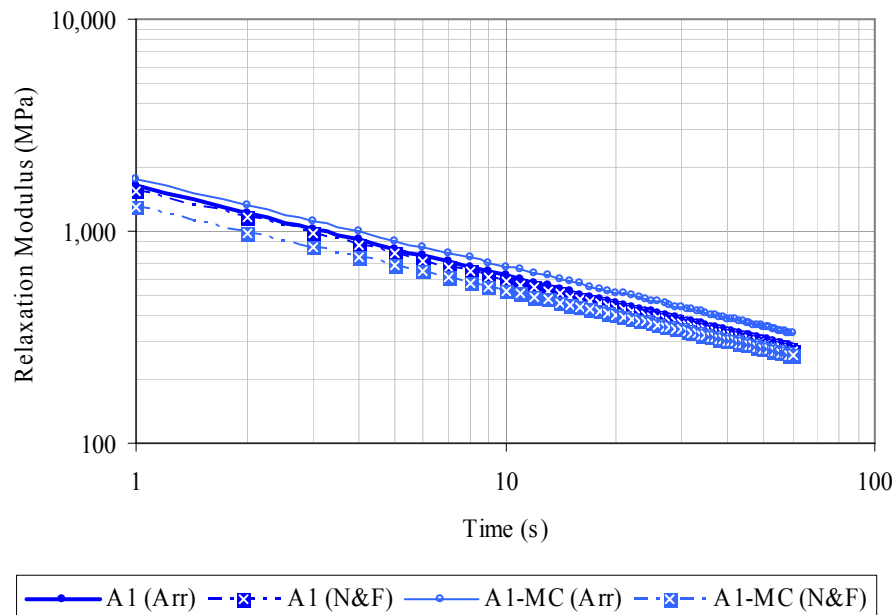
Figure 5.21. Comparison between the compressive relaxation modulus results and the Ninomiya and Ferry Interconversion for mix type *A1*
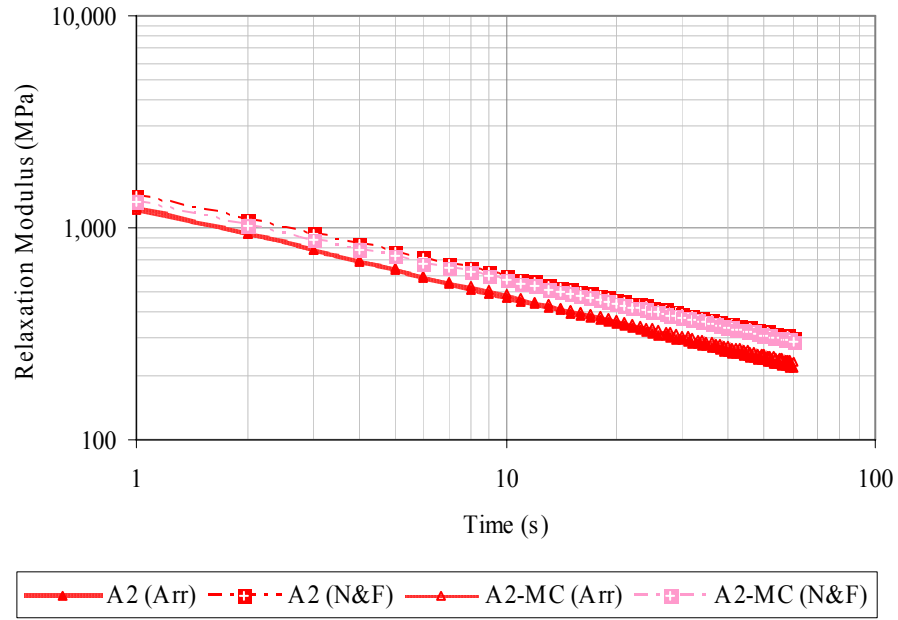
Figure 5.22. Comparison between the compressive relaxation modulus results and the Ninomiya and Ferry Interconversion for mix type *A2*
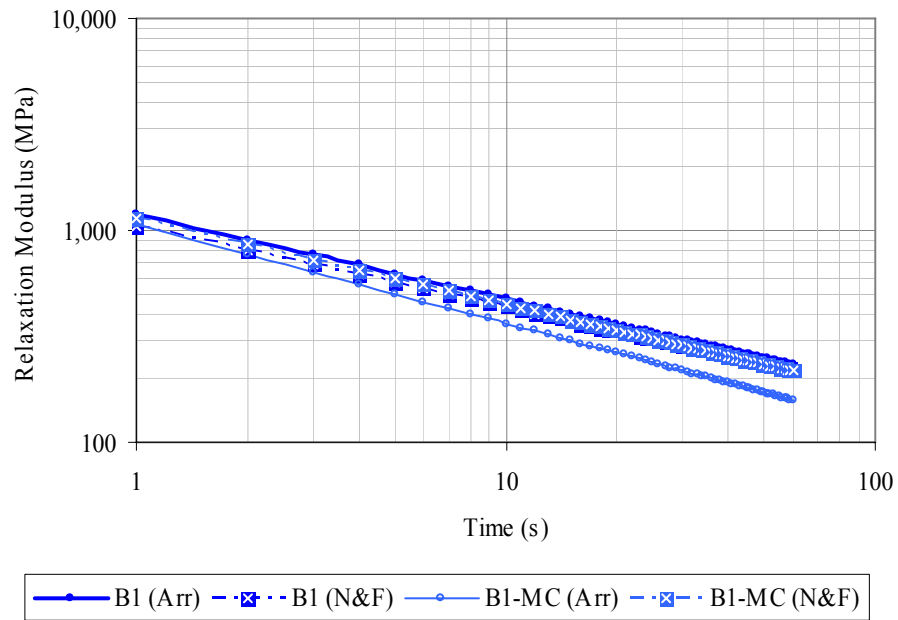
Figure 5.23. Comparison between the compressive relaxation modulus results and the Ninomiya and Ferry Interconversion for mix type *B1*
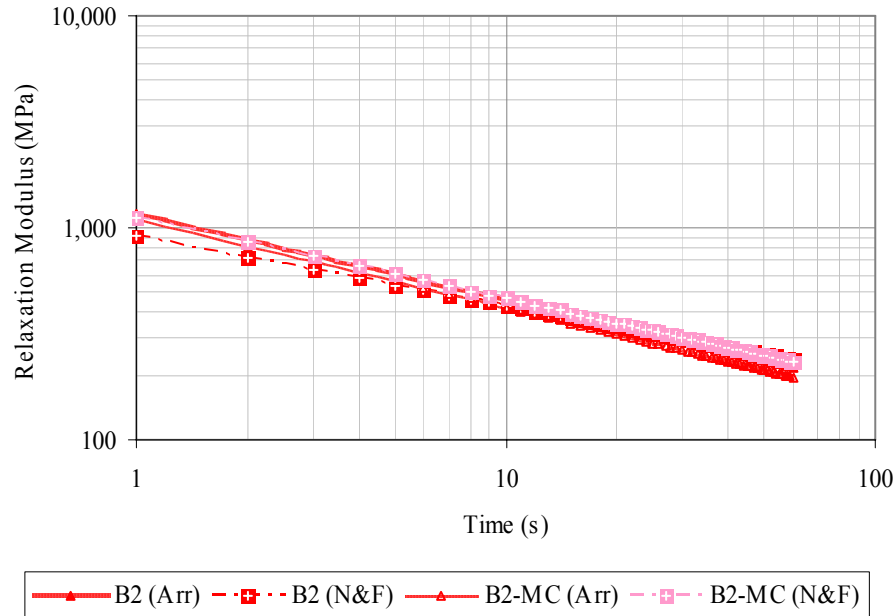
Figure 5.24. Comparison between the compressive relaxation modulus results and the Ninomiya and Ferry Interconversion for mix type *B2*

Statistical Analysis

The results of the approximation methods were compared to the compression relaxation tests using a statistical *t*-test analysis. The comparison was done against the results of each of the approximation methods to detect differences in the estimations. The hypothesis test was constructed as follows:

$$H_o : \mu_{RM} - \mu_{APPROXIMATION} = 0 \tag{5.30}$$

$$H_a : \mu_{RM} - \mu_{APPROXIMATION} \neq 0 \tag{5.31}$$

where μ_{RM} is the mean response of the compressive relaxation modulus results and $\mu_{APPROXIMATION}$ is the mean of the results obtained using the approximation method. The calculated *p*-value was compared against a significance threshold level of $\alpha = 0.05$ to derive a conclusion of accepting or rejecting the null hypothesis, H_o, in favor of the alternative hypothesis H_a. In this context, it is desirable to accept H_o in order to conclude that the fitted relaxation test results and the approximation results have no differences. In Table 5.9, a summary of the statistical results is presented, including the estimated *p*-value, the conclusion of the hypothesis test, and the average percent difference between the results:

$$\%\overline{\Delta} = \frac{\sum_1^{60}\left(\dfrac{E(t)_{APPROXIMATION} - E(t)_{RM}}{E(t)_{RM}}\right)*100}{60} \qquad (5.32)$$

where 60 represents the duration of the relaxation modulus test, in seconds. The highlighted values represent the best approximations, having the highest *p*-value and the lowest average percent difference.

Table 5.9. Statistical Analysis Results for the Approximation Methods

Mix type	Maxwell			Schapery and Park			Ninomiya and Ferry		
	p-value	Test	%Δ	*p*-value	Test	%Δ	*p*-value	Test	%Δ
A1	0.0045	Reject H_o	18	0.0904	Accept H_o	15	0.5935	Accept H_o	5
A1-MC	0.0015	Reject H_o	18	0.0003	Reject H_o	28	0.0050	Reject H_o	22
A2	0.0419	Reject H_o	26	0.0264	Reject H_o	24	0.0040	Reject H_o	32
A2-MC	0.2240	Accept H_o	19	0.0600	Accept H_o	19	0.0427	Reject H_o	20
B1	0.0456	Reject H_o	10	0.0776	Accept H_o	13	0.3577	Accept H_o	7
B1-MC	0.0900	Accept H_o	29	0.4240	Accept H_o	11	0.0189	Reject H_o	30
B2	0.3671	Accept H_o	14	0.0925	Accept H_o	10	0.7939	Accept H_o	6
B2-MC	0.8641	Accept H_o	13	0.9281	Accept H_o	4	0.2021	Accept H_o	14

Based on the statistical analysis, none of the results of the approximation methods were suitable to fit the dynamic modulus results of mixes *A1-MC* and *A2*. For the other mixes, at least two methods showed good correlation. The Schapery and Park approximation produced the best results, with six out of the eight mixes showing a good fit between the relaxation modulus and the approximated values (accept H_o). The Ninomiya and Ferry interconversion also yielded good results, with three mixes showing the largest *p*-value and lowest average relative difference among the results (highlighted values). The method that gave the poorest results was the generalized Maxwell model.

The results of the approximations show that tests performed in dynamic compression are not always comparable to the tests performed in direct static compression (relaxation test). In addition, the data analysis and statistical results of the dynamic and relaxations test presented in the previous section showed that none of the tests was consistent in differentiating between the conditioned and unconditioned response or between the different mix types within each condition (unconditioned and conditioned). Among the relaxation tests, the tensile results

showed better results when capturing the differences between moisture conditioned and unconditioned samples and when comparing different mix types within each condition. This observation is consistent with other researchers' reports that express that tensile tests are more efficient in evaluating moisture damage (Hicks 1991; Lottman 1978). A possible explanation to these observations is that tensile tests are able to better capture the interface strength between the asphalt and the aggregate, which is weakened by the moisture conditioning, as compared to compression tests that rely more on the aggregate structure. Therefore, a model based on fracture mechanics, which incorporates several properties of the asphalt mix instead of using a single test parameter as prescribed in traditional laboratory test methods, was developed to assess moisture damage as described in the next chapter.

CHAPTER VI

FRACTURE MODEL TO ASSESS MOISTURE DAMAGE [*]

The influence of air void structure on the moisture susceptibility of asphalt mixes was further studied using a fracture mechanics approach that accounted for fundamental material properties of the asphalt mix. The fracture model, based on Paris' law, was used to evaluate the crack growth of the conditioned and unconditioned samples. The input parameters of the model were the adhesive bond surface energy, the viscoelastic properties of the asphalt mix, the dissipated energy due to damage, and the tensile strength.

The next section explains the derivation of the crack growth equation and the experimental methods used to determine the viscoelastic properties, the dissipated energy due to damage, and the tensile strength of the asphalt mix. Then, a comparative analysis of the results with emphasis on the influence of air void structure is offered. Validation of the model using asphalt mixes with known field performance is presented in Chapter VII, along with the results for the corresponding asphalt mastic fractions. The model parameters for the asphalt mastics were obtained using the DMA.

Derivation of the Model

A crack growth index was used to evaluate the moisture susceptibility of the asphalt mix samples. The equation to estimate the crack growth was derived from Paris' law, which can be expressed in terms of the J-integral as follows:

$$\frac{dr}{dN} = A(J_R)^n \qquad (6.1)$$

where r is the average crack radius, N is the number of load cycles, A and n are material constants, and J_R is the J-integral, which can be expressed as the change in pseudostrain energy per unit volume of the intact material with respect to the change in crack surface area (*c.s.a.*) as follows:

$$J_R = \frac{\partial W_R}{\partial(c.s.a.)} = \frac{\dfrac{\partial W_R}{\partial N}}{\dfrac{\partial(c.s.a.)}{\partial N}} \tag{6.2}$$

It is assumed that *c.s.a.* has a value of $2\pi r^2$. Based on the experimental results, it was found that a linear relationship exists between the normalized pseudostrain energy and the natural logarithm of the load cycles, $W_R = a + b \ln(N)$. Therefore, b can be expressed as $b = \partial W_R/\partial \ln(N)$ and the expression for the J-integral becomes:

$$J_R = \frac{\dfrac{\partial W_R}{\partial \ln N}\dfrac{d \ln N}{dN}}{4\pi r \dfrac{dr}{dN}} = \frac{b}{4\pi r N \dfrac{dr}{dN}} \tag{6.3}$$

$$J_R = \frac{b}{4\pi r N \dfrac{dr}{dN}} \tag{6.4}$$

The value of the constant A has been expressed by Lytton et al. (1993) as:

$$A = k\left(\frac{E_R}{E_1 \Delta G_f - E_1 E_\infty E_R J_R}\right)^n \left(\frac{1}{\sigma_t^2 I_1}\right)^n \int_0^{\Delta t} (w(t))^n \, dt \tag{6.5}$$

where k is a material constant, E_1 is the initial relaxation modulus, ΔG_f is the partial wet adhesive bond surface energy between the asphalt binder and the aggregate, E_∞ is the final value of the relaxation modulus after a long elapsed time, E_R is the reference modulus, σ_t is the tensile strength of the material, I_1 is a parameter that describes the shape of the stress-strain curve, and $w(t)$ is a function that describes the shape of the applied load with respect to time.

The material constant k is different for each material but varies only slightly between various materials. For simplicity, k is assumed to have a value of 1. In the type of tests conducted in this study, E_∞ is close to zero. Therefore, the denominator of the first bracket is reduced to $E_1 \Delta G_f$. The shapes of the stress-strain curves are similar for the mixes used in this study, and thus the parameter I_1 can be assumed to be the same and equal to 1 for all mixes. In addition, since an identical sinusoidal loading shape is applied to all samples, the value of $\int_0^{\Delta t} (w(t))^n \, dt$ is equal for all samples. These considerations reduce the expression for A to:

$$A = k\left(\frac{E_R}{E_1 \Delta G_f \sigma_t^2}\right)^n \tag{6.6}$$

Substituting the terms of A and J_R back in the Paris' law equation gives:

$$\frac{dr}{dN} = k\left(\frac{E_R}{E_1 \Delta G_f \sigma_t^2}\right)^n \left(\frac{b}{4\pi r N \frac{dr}{dN}}\right)^n \tag{6.7}$$

The above equation can be rearranged to give the following expressions:

$$\left(\frac{dr}{dN}\right)^{1+n} r^n = k\left(\frac{E_R}{E_1 \Delta G_f \sigma_t^2}\right)^n \left(\frac{b}{4\pi N}\right)^n \tag{6.8}$$

$$(dr)^{1+n} r^n = k\left(\frac{E_R}{E_1 \Delta G_f \sigma_t^2}\right)^n \left(\frac{b}{4\pi}\right)^n \left(\frac{dN^{1+n}}{N^n}\right) \tag{6.9}$$

Integrating both sides gives the following:

$$\int_{r_0}^{r} r^{\frac{n}{1+n}} dr = k^{\frac{1}{1+n}}\left(\frac{E_R}{E_1 \Delta G_f \sigma_t^2}\right)^{\frac{n}{1+n}} \int_{1}^{N}\left(\frac{b}{4\pi}\right)^{\frac{n}{1+n}}\left(\frac{dN}{N^{\frac{n}{1+n}}}\right) \tag{6.10}$$

$$\frac{(r)^{\frac{2n+1}{1+n}} - (r_o)^{\frac{2n+1}{1+n}}}{\left(\frac{2n+1}{1+n}\right)} = k^{\frac{1}{1+n}}\left(\frac{E_R}{E_1 \Delta G_f \sigma_t^2}\right)^{\frac{n}{1+n}}\left(\frac{b}{4\pi}\right)^{\frac{n}{1+n}}(1+n)\left(N^{\frac{1}{1+n}} - 1^{\frac{1}{1+n}}\right) \tag{6.11}$$

The equation to estimate crack growth in asphalt mixes can be then expressed as:

$$r = \left[r_o^{\frac{2n+1}{1+n}} + (2n+1)\left(\frac{bE_R}{4\pi E_1 \Delta G_f \sigma_t^2}\right)^{\frac{n}{1+n}}\left(N^{\frac{1}{1+n}} - 1^{\frac{1}{1+n}}\right)\right]^{\frac{1+n}{2n+1}} \tag{6.12}$$

Schapery (1981) derived the relationship between the exponent n in Equation 6.1 and m, which is the exponent of time in the power law equation of the relaxation modulus in Equation 5.2. He found that if the surface energy of the material and the length of the fracture process zone ahead of the crack are constant, then $n = 1/m$. However, if the tensile strength of the material and surface energy are constants during fracture, then $n = (1 + 1/m)$. Later, Lytton et al. (1993) associated the former case with strain-controlled loading and the latter case with stress-

controlled loading. As such, for the strain-controlled loading conducted in this study the relationship $n = 1/m$ was adopted.

Asphalt Mix Samples

The asphalt mix samples used to estimate the crack growth index consist of gradation *A* and gradation *B* cored and trimmed samples to a final dimension of 100 mm (4 in) diameter by 100 mm (4 in) height. The material properties and sample preparation were previously described in Chapter III. The aggregate gradations are included in Tables 3.11 and 3.12 and a plot can be found in Figure 3.1. The description of the air void characterization using X-ray CT and image analysis is also included in Chapter III. Figures 3.8, 3.9, and 3.10 show details of the air void structure, while Table 3.18 presents the air void content and air void size results. The moisture conditioning procedure is detailed at the end of Chapter III.

Determination of the Model Parameters

To obtain the input parameters used to estimate the crack growth, surface energy measurements and mechanical tests were performed on the samples. The estimation of the surface energy components was explained in Chapter III and the determination of the viscoelastic parameters was completed by performing a direct compressive and tensile relaxation test previously described in Chapter V. The other mechanical tests required to obtain the dissipated energy and the tensile strength are explained next. The sample setup for the mechanical tests was done as described in Appendix C. Three replicate samples of each mix type were tested.

Viscoelastic Properties

Relaxation tests at 10 °C (50 °F), 20 °C (68 °F), and 30 °C (86 °F) were conducted on the asphalt mix samples. The strain level for the relaxation test should be low enough to prevent damaging the sample. Therefore, the selected strain level was 200 $\mu\varepsilon$, which has been used with success to perform similar relaxation tests (Si 2001; Walubita 2006). The test protocol, relaxation modulus estimation, and Arrhenius function to fit the data were presented in Chapter VI. In this case, the relaxation modulus results at 10 °C (50 °F) and 20 °C (68 °F) were shifted to a reference temperature of 30 °C (86 °F). The resulting E_1 and *m* parameters are presented at the end of the Adhesive Bond Energy subsection; only the tensile relaxation results are considered in the crack growth model.

Dissipated Pseudostrain Energy and Reference Modulus

A dynamic direct tension test was used to determine the dissipated pseudostrain energy parameter of the model (*b*). The strain level during the dynamic direct tension test should be high enough to induce some damage. As described subsequently, damage was detected by the change in the stress versus pseudostrain relationship. Therefore, based on others' experience, the dynamic direct tension test consisted of the application of a haversine strain shape at a strain level of 350 $\mu\varepsilon$ for 0.1 s followed by a rest period of 0.9 s as shown in Figure 6.1 (Si 2001; Walubita 2006). The loading frequency was 1 Hz, and the total number of applied load cycles was 1000. The test was performed at a temperature of 30 °C (86 °F), and three replicates for each mix type and moisture condition were used. The load-induced displacements were measured using three LVDTs placed at 120° along the circumference of the sample that were zeroed before the beginning of the test (Figure 5.2). The distance between the LVDT holders was 50 mm (2 in) since only 100 mm (4 in) height samples were used for this test. Details of the LVDT configuration and sample setup are presented in Appendix C, while the test setup was previously shown in Figure 5.3. The test was performed on the same replicates used for the relaxation modulus test, and the procedure was performed within 10 min after the relaxation modulus test at 30 °C (86 °F) was completed.
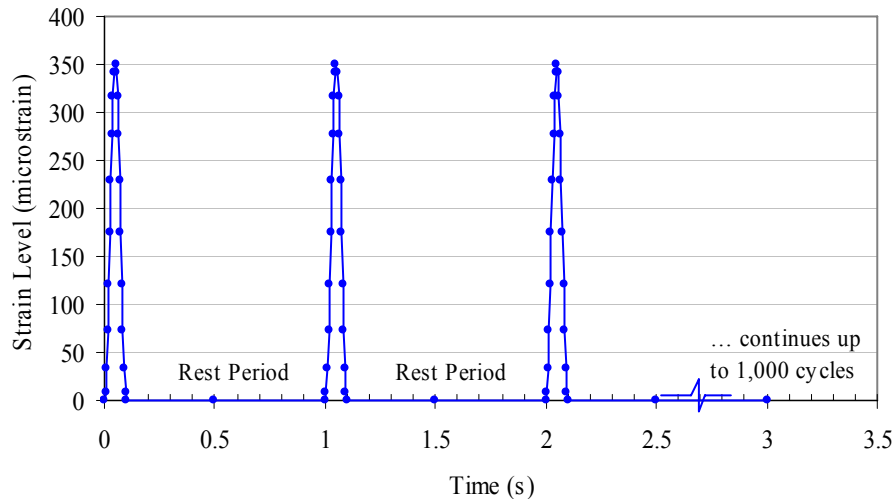
Figure 6.1. Loading protocol for the dynamic direct tension test

The applied stress was calculated as follows:

$$\sigma_m(t) = \frac{P(t)}{\pi r^2}$$

(6.13)

where $\sigma_m(t)$ is the measured time-dependent tensile stress, $P(t)$ is the applied load, and r is the radius of the sample. The viscoelastic stress was then computed for each load cycle using the Boltzmann superposition as follows (Si 2001):

$$\sigma_{VE}(t) = \Sigma_{i=1}^{x} E_1 (\tau - t_i)^{-m} \left(\frac{d\varepsilon}{dt} \right)_i dt$$

(6.14)

where E_1 is the initial relaxation modulus, τ is the last value of time in the load cycle, t is the ith value of time in the load cycle, m is the modulus relaxation rate, $\left(\dfrac{d\varepsilon}{dt} \right)_i$ is the change in strain for every i^{th} time increment, dt is the time increment, and x is the number of data points recorded during each load cycle.

The pseudostrain, $\varepsilon_R(t)$, is calculated as the ratio of the viscoelastic stress to the reference modulus (Si 2001):

$$\varepsilon_R(t) = \frac{\sigma_{VE}(t)}{E_R}$$

(6.15)

The reference modulus, E_R, was estimated as follows:

$$E_R = \frac{\sigma_m(t)_{max}}{\varepsilon_{max}}$$

(6.16)

where $\sigma_m(t)_{max}$ is the maximum measured time-dependent tensile stress that usually corresponds to the first load cycle (nonlinear response), and ε_{max} is the applied target tensile strain of 350 $\mu\varepsilon$. This value for E_R makes the pseudostrain equal to the actual applied strain.

When the values of the applied stress, $\sigma_m(t)$, are plotted versus the computed pseudostrain, $\varepsilon_R(t)$, they form an oval-shaped loop, as shown in Figure 6.2. The area inside the loop, which represents the DPSE in each load cycle, was computed using the area by coordinates method (Wolf and Ghilani 2002). In essence, the pseudostrain energy quantifies the difference between the energy at high strain level used in the dynamic test and the linear viscoelastic energy that is measured at small strain levels. In order to account for the reduction in material that is capable of dissipating energy, the DPSE was normalized by the ratio of (S_i/S_o) as follows:

$$W_R = \frac{DPSE}{\left(\dfrac{S_i}{S_0}\right)} \qquad\qquad (6.17)$$

where the value of S_i is the pseudostiffness and is computed for each load cycle as the ratio of the maximum applied stress and the pseudostrain, and S_o is the maximum pseudostiffness, which usually corresponds to the first load cycle.
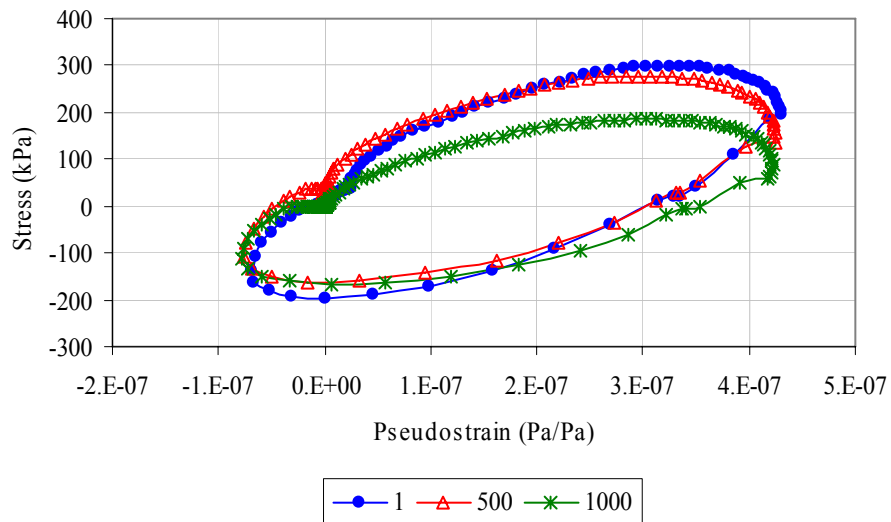
Figure 6.2. Applied stress versus computed pseudostrain for different load cycles

Distinction needs to be made between the viscoelastic properties used in calculating the DPSE energy in Equation 6.14 and those used in the crack growth expression presented in Equation 6.12. In calculating the dissipated pseudostrain energy, the viscoelastic properties and the reference modulus are associated with the undamaged state, which is the dry state. Therefore, the values of E_1 and m in Equation 6.14, the value of S_o in Equation 6.17, and the value of the reference modulus, E_R, used to compute the pseudostrain correspond to the dry state. However, based on the derivation of Schapery (1981) and Lytton et al. (1993), the values of E_1 and n in Equation 6.12 correspond to the material surrounding the crack, either dry or moisture conditioned.

When W_R is plotted against number of load cycles on a semi-log scale, the relationship yields a linear trend as shown in Figure 6.3. The relationship can be described as follows:

$$W_R = a + b \ln(N) \tag{6.18}$$

The intercept, denoted by a, represents the energy that is associated with the initial damage and material nonlinearity due to the difference in the strain used in determining the viscoelastic properties (200 $\mu\varepsilon$) and the strain used in the damage dynamic test (350 $\mu\varepsilon$). The slope, b, represents the rate of fracture damage accumulation with respect to load cycles.
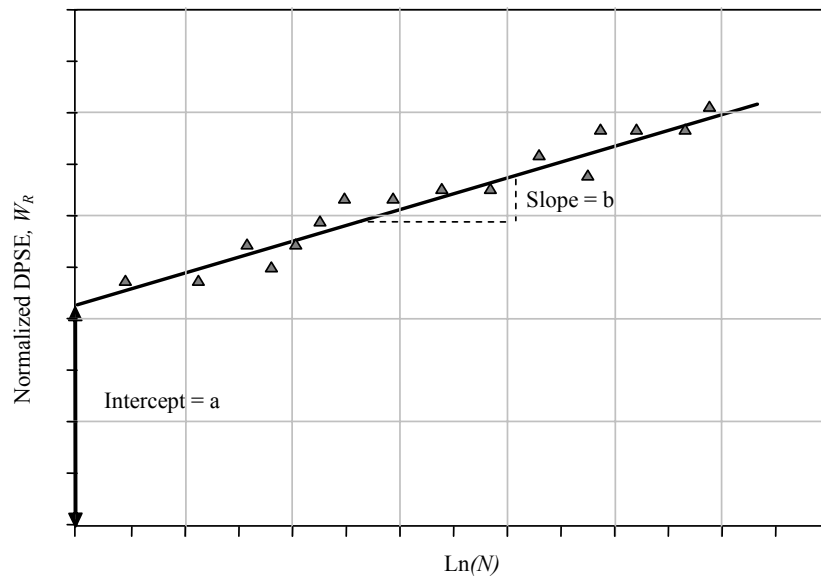
Figure 6.3. Schematic representation of the change in DPSE with load cycles

The material nonlinearity corresponds to the behavior of the intact portion of the material at higher strain levels, while the initial damage is caused by the presence of initial cracks and voids (r_o in Equation 6.12). It is difficult to partition the initial energy, a, into the nonlinear and initial damage fractions. Therefore, the initial energy, a, was subtracted from the pseudostrain energy, W_R, and the mixes were compared based on the crack growth behavior, which corresponds to the second part of Equation 6.12, and includes the slope b of the W_R versus $\ln(N)$ relationship (Figure 6.3). Then, the expression of the crack growth index ($c.g.i.$) becomes:

$$c.g.i. = (r - r_o) = \left[(2n+1)^{\frac{1+n}{2n+1}} \left(\frac{bE_R}{4\pi E_1 \Delta G_f \sigma_t^2} \right)^{\frac{n}{2n+1}} \left(N^{\frac{1}{1+n}} - 1^{\frac{1}{1+n}} \right)^{\frac{1+n}{2n+1}} \right] \quad (6.19)$$

Tensile Strength

After the dynamic tension test, when the sample is assumed to have developed some damage, a tensile strength test at 30 °C (86 °F) and a rate of 0.25 mm/min (0.01in/m in) was conducted on the samples until failure. The test was performed within 10 min of the completion of the dynamic direct tension test. During the test, the load and axial deformation were recorded every 0.1 s. Three replicates for each mix type and moisture condition were tested, and the average results are listed at the end of the Adhesive Bond Energy subsection. Details of the LVDT configuration and sample setup are presented in Appendix C, while the test setup was previously shown in Figure 5.3. Failure in the tensile strength test usually occurred in the center of the sample, between the LVDT holders as shown in Figure 6.4.

As expected, the conditioned samples differed from the unconditioned samples after failure. The conditioned samples exhibited a significant amount of stripping or loss of adhesion between the asphalt binder and the aggregate, while the unconditioned samples showed better-coated aggregates through the section of the sample, as illustrated in Figure 6.5. Furthermore, a considerable amount of water was observed on all the failed surfaces of the conditioned gradation *A* samples and in some of the conditioned gradation *B* samples. Apparently, during the moisture conditioning procedure, water was able to permeate the voids under vacuum and was unable to escape due to the small void sizes and lack of permeability.

Figure 6.4. Type of sample failure after the completion of the tensile strength test
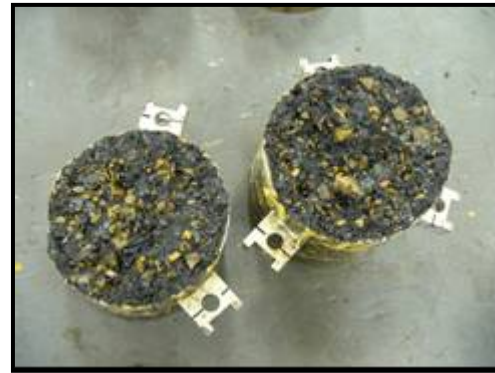
(a)   (b)

Figure 6.5. Failed samples after the tensile strength test. (a) unconditioned samples showing well-coated aggregates (b) conditioned sample showing stripping failure

The maximum tensile strength and corresponding failure strain are calculated as follows:

$$\sigma_{t\,max} = \frac{P_{max}}{\pi r^2} \tag{6.20}$$

$$\varepsilon_f = 10^6 \frac{\Delta L_{max}}{L_0} \tag{6.21}$$

where P_{max} is the peak tensile load, r is the radius of the sample, ε_f is the failure tensile strain at P_{max} in microns, ΔL_{max} is the deformation at P_{max}, and L_0 is the distance between the LVDT holders. For each sample, ε_f was calculated as the average of the three LVDTs deformations.

Adhesive Bond Energy

The surface energy characteristics of the asphalt binder and the aggregates were obtained using the WP and the USD as explained in Chapter III. Based on Tables 3.7 and 3.8, the value of the fracture component of the adhesive bond energy is $\Delta G_{ba}{}^a = 254.24$ erg/cm^2 in a dry condition and $\Delta G_{bwa}{}^a = -30.51$ erg/cm^2 in the presence of water. These values correspond to the bond surface energy between the aggregate and the asphalt binder in a fully dry condition (when no moisture is present in the mix) and in a fully wet condition (when water saturates the interfaces between the asphalt binder and the aggregate). During testing, however, the material is not completely dry or fully saturated; a partially wet condition exists at the interface of the aggregate and the asphalt binder (Kim et al. 2004; Lytton et al. 1993; Zollinger 2005). In Equation 6.19, the adhesive bond surface energy between the asphalt binder and the aggregate, ΔG_f, represents the value in a partially wet condition. The ratio of the partially wet bond energy to the dry bond energy was assumed proportional to the ratio of the normalized pseudostiffness under wet conditions (MC) to that under dry conditions as follows:

$$\Delta G_f = \frac{\left(\dfrac{S_i}{S_0}\right)_{MC}}{\left(\dfrac{S_i}{S_0}\right)_{DRY}} \Delta G_{ba}^a \tag{6.22}$$

Table 6.1 shows a summary of all input parameters used in the *c.g.i.* equation (Equation 6.19).

Table 6.1. Input Parameters for the Crack Growth Index Equation

Mix type	E_1 (MPa)	m	$n = 1/m$	E_R * (MPa)	b	ΔG_f ** (J/m^2)	σ_t (kPa)
A1	396	0.4684	2.1430	2,350	9.0×10^{-4}	0.2542	333
A1-MC	297	0.5279	1.9053	1,955	1.7×10^{-3}	0.1767	242
A2	232	0.4649	2.1605	1,984	2.0×10^{-4}	0.2542	309
A2-MC	865	0.5369	1.8800	1,910	7.0×10^{-4}	0.2222	271
B1	153	0.3661	3.0552	1,234	2.8×10^{-3}	0.2542	387
B1-MC	288	0.2926	3.4511	957	2.6×10^{-3}	0.2459	240
B2	335	0.1953	5.4944	1,231	5.1×10^{-3}	0.2542	322
B2-MC	321	0.1731	5.8168	1,214	3.6×10^{-3}	0.2470	336

* The E_R values for the MC samples are not used in the analysis, only the dry ones
** Using $S_i = S_{1000}$ in Equation 6.22

Results and Analysis

The crack growth values for the replicates of each mix type were calculated and plotted against the number of load cycles as shown in Figures 6.6 through 6.9. The relationship between these two variables represents the moisture damage rate with respect to load cycles. The average crack growth for each mix type was also determined as presented in Figure 6.10. These plots suggest that there are certain air void structures that are more susceptible to moisture damage than others.

Moisture sensitivity of each asphalt mix type was evaluated by computing the ratio of the conditioned to the unconditioned or dry crack growth values. The higher the value of the ratio, the more prone the mix will be to moisture damage; the closer the ratio is to 1, the less moisture susceptible. The average ratio of the crack growth at $N = 1000$ for mixes A1, A2, B1, and B2 was equal to 3.24, 2.89, 1.34, and 0.82, respectively. Thus, the most susceptible mix to moisture conditioning was mix A1, which had a uniform air void structure and the smallest range of air void content and air void sizes as previously presented in Figures 3.8 and 3.10. For mix B2, the ratio was less than 1.0, which could have been due to the larger air void size and content (Table 3.18) or due to inherent sample variability. Another possible explanation for this behavior is that the air void structure of mix type B was less affected by moisture damage. However, in the case of mix type B the same sample replicates were used for both the dynamic modulus and the tensile tests, and therefore a more plausible reason for the observed behavior is those samples had an important initial level of damage that hindered the observation of further crack growth. Another important variable that could have an effect on the results was the moisture conditioning process, which was done on the 150 mm (6 in) height samples of mix type A and the smaller 100

mm (4 in) samples of mix type *B*. This observation is based on the fact that all the conditioned samples of mix *A* had water in the failed surfaces while only a few of the samples of mix type *B* did.
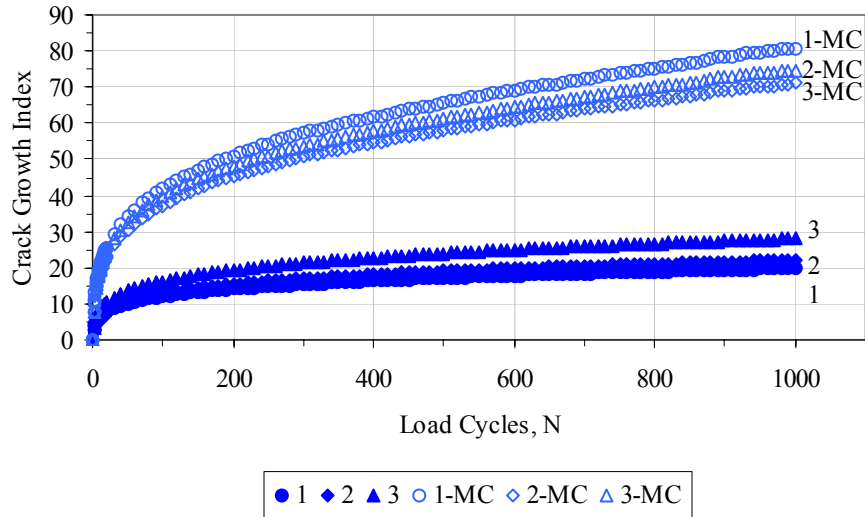
Figure 6.6. Crack growth index as a function of load cycles for the replicates of mix type *A1*
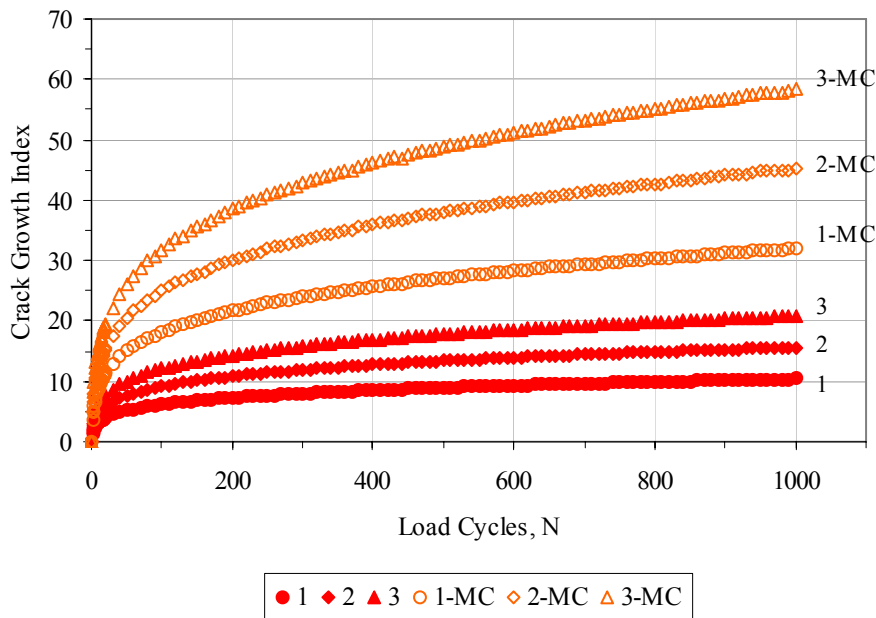
Figure 6.7. Crack growth index as a function of load cycles for the replicates of mix type *A2*
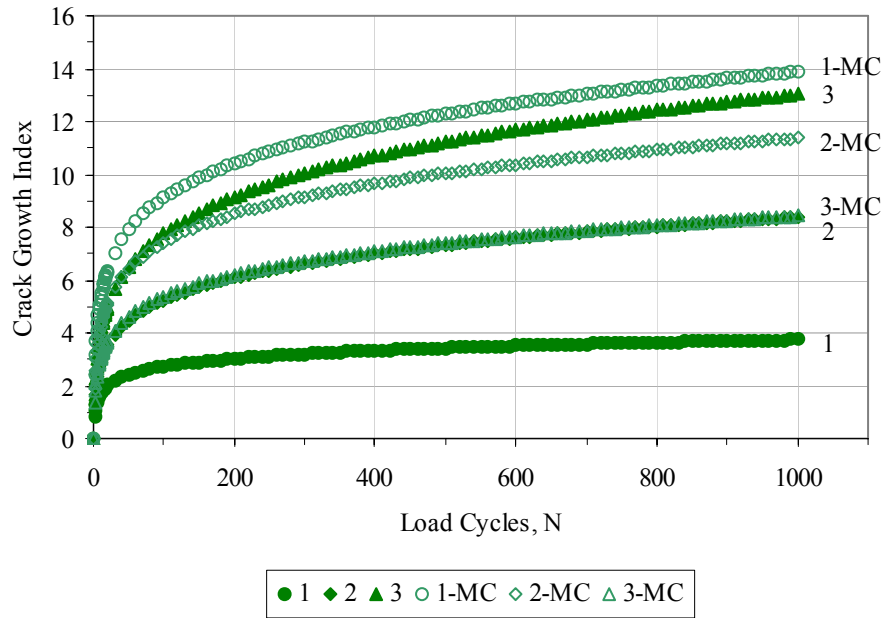
Figure 6.8. Crack growth index as a function of load cycles for the replicates of mix type *B1*
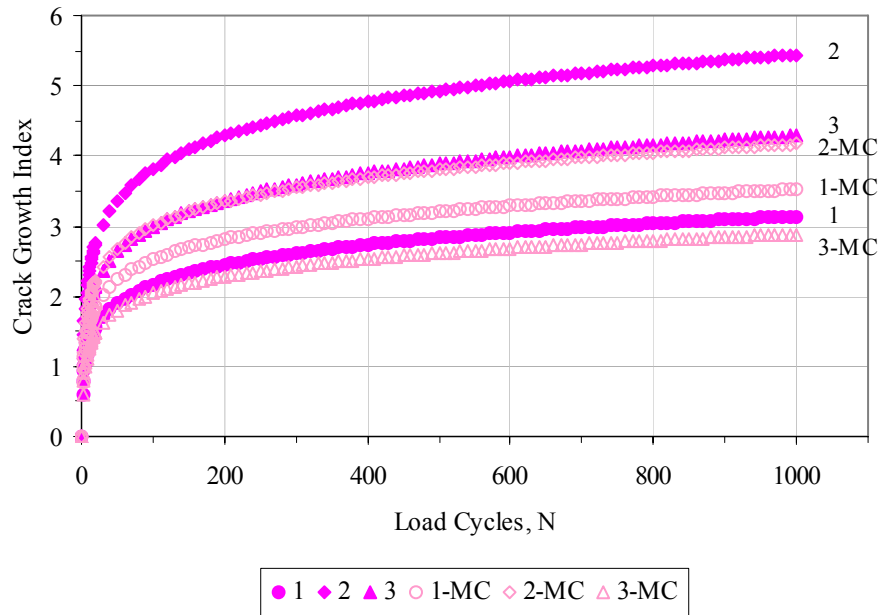
Figure 6.9. Crack growth index as a function of load cycles for the replicates of mix type *B2*
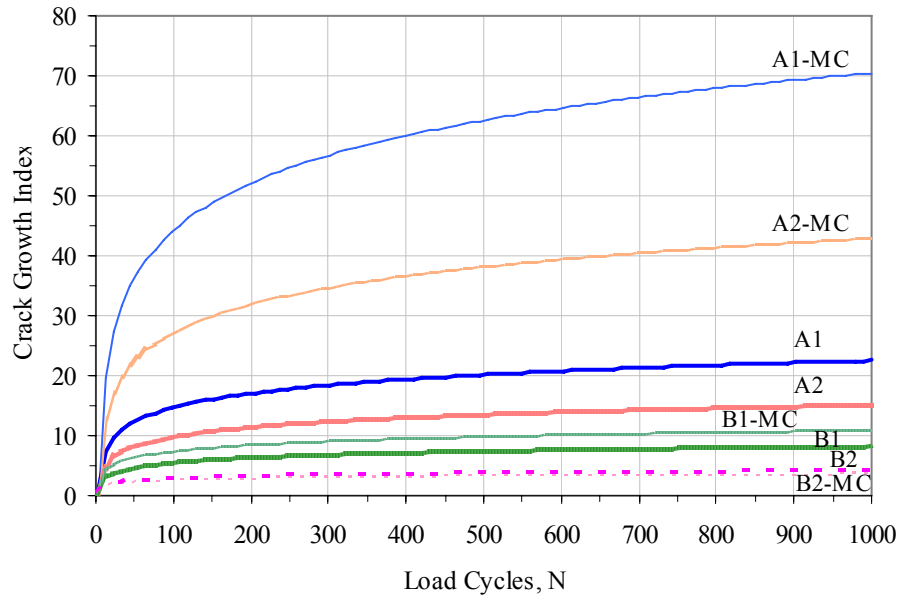
Figure 6.10. Average crack growth index as a function of load cycles for each mix type

A two-sample t-test was performed on the crack growth values at $N = 1000$ load cycles to evaluate if the crack growth index was sensitive to the effect of sample conditioning. The following null (H_o) and alternative (H_a) hypothesis were used:

$$H_o : \mu_{dry} - \mu_{MC} = 0 \tag{6.23}$$

$$H_a : \mu_{dry} - \mu_{MC} \neq 0 \tag{6.24}$$

where μ_{dry} is the average response of the unconditioned results and μ_{MC} is the average response of the moisture conditioned results. The statistical two-sample t-test was performed by comparing the difference between the average responses, estimating the probability or p-value, and comparing it against a significance threshold level of $\alpha = 0.05$. If the p-value was less than α, H_o was rejected in favor of H_a, which implied that the crack growth values between the conditioned and unconditioned responses were different. Table 6.2 shows the statistical results of the comparisons between the unconditioned and conditioned responses of the different mix types, as well as the conclusions of the hypothesis tests.

Table 6.2. Results of the Two-Sample *t*-test Analysis Comparing the Unconditioned and Conditioned Response of the Crack Growth Index

Mix type	p-value	Hypothesis test
A1 versus *A1-MC*	0.000	Reject H_o
A2 versus *A2-MC*	0.023	Reject H_o
B1 versus *B1-MC*	0.413	Accept H_o
B2 versus *B2-MC*	0.373	Accept H_o

As expected based on the results presented in Figures 6.6 through 6.9, mixes *A1* and *A2* presented significant differences in the conditioned and unconditioned mean values (Reject H_o), but mixes *B1* and *B2* showed no statistically significant differences in the unconditioned versus conditioned crack growth values.

A statistical ANOVA was also performed to evaluate the effectiveness of the model in capturing the differences between the different mix types within each condition. The statistical hypotheses considered for the unconditioned and conditioned case were:

$$H_o : \mu_{A1} = \mu_{A2} = \mu_{B1} = \mu_{B2} \tag{6.25}$$

$$H_a : \text{at least two of the } \mu_i\text{'s are different} \tag{6.26}$$

In this case, the test statistic or *F*-value was used to evaluate the differences in variation between the responses of the different mix types to the variation within the replicates of each sample type by comparing it against the selected significance threshold level of $\alpha = 0.05$. When the *F*-value was less than α, H_o was rejected, which implied that the responses were statistically different. The results of this analysis are presented in Table 6.3.

Table 6.3. Results of the ANOVA Comparing the Responses of the Different Mix Types within Each Condition

Mix condition	*F*-value	p-value	Hypothesis test
Unconditioned	12.425	0.002	Reject H_o
Conditioned	64.187	0.000	Reject H_o

The results show that the crack growth values of the different mix types within each condition (unconditioned and moisture conditioned) were statistically different.

CHAPTER VII
VALIDATION OF THE FRACTURE MODEL [*]

The validity and applicability of the crack growth model were further studied using asphalt mixes with known field performance. The DMA results on their corresponding asphalt mastic fraction were also available (Lytton et al. 2005; Zollinger 2005). Asphalt mixes were prepared in the laboratory using the same mix designs as the field mixes and following the mix preparation protocol previously discussed in Chapter III. The validation process consisted of the following steps:

1) dynamic testing of asphalt mixes,
2) analysis to determine the crack growth model parameters,
3) surface energy measurements of the aggregates and asphalt binders,
4) dynamic testing and analysis for asphalt mastics, and
5) comparison of the analysis results with field performance.

Subsequent sections describe the methodology and results of the validation study. The first section describes the characteristics of the asphalt mixes, followed by a section that includes a description of the asphalt mastics. The values used as inputs for the fracture model and the results of the analysis are given in the last section of this chapter.

Description of Mixes and Field Performance

A list of the selected mixes for this validation study in terms of their type, location, aggregate and asphalt binder type, and reported field performance is presented in Table 7.1. The reported variables correspond to the ones presented by Lytton el al. (2005). The aggregate gradations are presented in Figure 7.1. Although no information was available on the initial or target air void content of the mixes after construction, the in-place air voids requirement for dense-graded mixes in Texas is from 5 to 9 percent, and in Ohio the requirement is approximately 4 to 8 percent (ODOT 2005; TxDOT 2004a).

---

[*] Presented at the 86th Annual Meeting of the Transportation Research Board, "Moisture Susceptibility of Asphalt Mixtures with Known Field Performance Using Dynamic Analysis and a Crack Growth Model" by Edith Arambula, Eyad Masad, Amy Epps Martin, January 24, 2007, Washington, D.C., and accepted for publication in the 2007 series of the *Transportation Research Record: Journal of the Transportation Research Board* (forthcoming).

Table 7.1. Description of the Asphalt Mixes Used in the Validation Study

Mix label	Highway	Mix type	Location	Field moisture performance	Aggregate type	Binder grade
AF	Texas IH 20	Superpave	Atlanta, TX	Good	River Gravel	PG 76-22
BF	Ohio SR 511	Type 1	Ashland County, OH	Fair to Poor	Gravel, Limestone, Reclaimed Asphalt Pavement (RAP)	PG 64-22
CF	Ohio SR 226	Type 1 Intermediate	Wayne County, OH	Poor	Gravel, RAP	PG 64-28
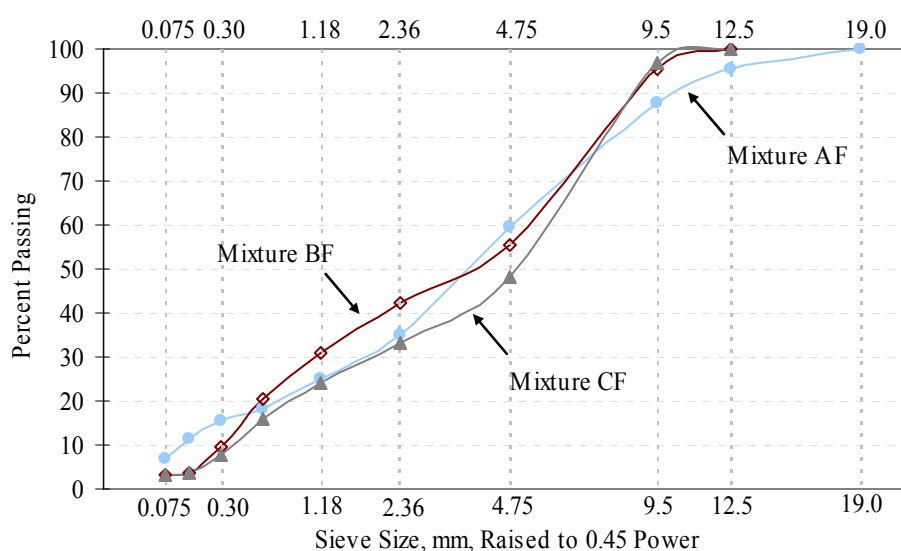
Figure 7.1. Aggregate gradations for the mixes with known field performance

Mix *AF* was used by the TxDOT in Harrison County in the construction of Interstate Highway 20. The mix design included 67 percent siliceous river gravel, 32 percent limestone screenings (TXI Limestone), and 1 percent hydrated lime. The asphalt binder content was 5.0 percent by weight of the mix. Based on field and laboratory test results, mix *AF* exhibited overall good performance, and did not exhibit evidence of moisture damage.

Mix *BF* was constructed on State Route 511 in Ashland County, Ohio. It included 32 percent limestone, 22 percent gravel, 26 percent natural sand, and 20 percent reclaimed asphalt pavement (RAP). During sample preparation, the RAP material was proportionally replaced with the other aggregates in the mix. Therefore, the final mix proportion included 40 percent

limestone, 27.5 percent gravel, and 32.5 percent natural sand. The asphalt binder content was 5.4 percent by weight of the mix.

Mix *CF* was constructed on State Route 226 in Wayne County, Ohio. It consisted of 52 percent gravel, 14 percent limestone, 14 percent natural sand, and 20 percent RAP. Again, the RAP material was replaced for a final mix proportion of 65 percent gravel, 17.5 percent limestone, and 17.5 percent natural sand. The asphalt binder content was 5.0 percent by weight of the mix.

The Ohio Department of Transportation (ODOT) performed a field evaluation of certain pavement sections where mixes *BF* and *CF* were used. The reported pavement condition rating (PCR) for mix *BF* dropped from 95 to 89 from 2000 to 2004 and for mix *CF* dropped from 97 to 60 from 1998 to 2004. Extensive amounts of cracking and raveling were observed in these pavements, especially in the sections where mix *CF* was applied. According to ODOT, the primary cause of the moisture-induced distresses is the type of gravel aggregate used (Lytton et al. 2005).

The crack growth model was used to evaluate the moisture susceptibility of mixes *AF*, *BF*, and *CF*. Six replicates for each mix type were prepared and compacted in the laboratory using the SGC. The compacted samples with a dimension of 150 mm (6 in) diameter by 165 mm (6.5 in) height were cored and trimmed to a final size of 100 mm (4 in) diameter by 150 mm (6 in) height. Three of the six replicates were moisture conditioned following the modified Lottman test procedure without the freezing step that was explained in Chapter III. The procedure specifies 70 to 80 percent vacuum saturation with water by weight. To satisfy this requirement, samples of mix *AF* required 25 s of saturation time, while samples of mix *BF* and *CF* required 900 s.

Three LVDTs placed 120° from one other were used measure the load-induced displacement; the vertical distance between LVDT holders was 100 mm (4 in). To obtain the parameters required to estimate the *c.g.i.* in Equation 6.19, relaxation, direct dynamic tension, and tensile strength tests were performed on the samples and surface energy values were obtained to estimate the partial wet adhesive bond energy value. Details of these tests protocols were presented in previous chapters.

The WP and the USD were used to estimate the values of the surface energy components of the asphalt binder and the aggregates, respectively. The results of the adhesive bond surface energy with and without the presence of water for the different types of aggregates are presented

in Table 7.2. These results correspond to the wetting contact angle measured with the WP, used previously to better differentiate the response of the asphalt mastic fractions (Lytton et al. 2005). The values presented in Table 7.2 correspond to each individual type of aggregate. Since more than one aggregate type is present in each mix, to obtain ΔG^a for the mix, a weighted average based on the corresponding aggregate proportions was utilized (Table 7.3).

As mentioned in Chapter VI, the ΔG^a values presented in Table 7.3 correspond to a fully dry or a fully wet condition, although during testing the material is not completely dry or fully saturated, but a partially wet condition exists at the interface of the aggregate and the asphalt binder. Therefore, the adhesive bond surface energy between the asphalt binder and the aggregate, ΔG_f, used in the fracture model represents the value in a partially wet condition and estimated using Equation 6.22.

Table 7.2. Adhesive Bond Surface Energy with and without the Presence of Water for the Mixes with Known Field Performance

Mix type	Field moisture Performance	Aggregate	Adhesive dry $\Delta G_{ba}{}^a$ (erg/cm^2)	Adhesive wet $\Delta G_{bwa}{}^a$ (erg/cm^2)
AF	Good	Gravel	93.36	-75.20
		TXI Limestone	118.87	-151.14
BF	Fair to Poor	Limestone	87.49	-115.58
		Gravel	94.56	-160.22
CF	Poor	Limestone	81.27	-119.82
		Gravel	90.92	-161.87

Table 7.3. Weighted Average for the Adhesive Bond Surface Energy with and without the Presence of Water for the Mixes with Known Field Performance

Mix type	Field moisture performance	aggregates	Weighted Adhesive Dry $\Delta G_{ba}{}^a$ (erg/cm^2)	Weighted Adhesive Wet $\Delta G_{bwa}{}^a$ (erg/cm^2)	Ratio $\dfrac{\Delta G_{ba}{}^a}{\Delta G_{bwa}{}^a}$
AF	Good	Gravel and TXI Limestone	101.6	-99.7	1.0186
BF	Fair to Poor	Gravel and Limestone	90.4	-133.8	0.6756
CF	Poor	Gravel and Limestone	88.9	-153.0	0.5811

Characterization of Asphalt Mastic Samples and Model Parameters

Several cylindrical asphalt mastic samples 12 mm (0.5 in) diameter by 50 mm (2 in) height were cored from a sample compacted using the SGC. The samples were prepared with a mixture of aggregates smaller than the no. 16 (1.18 mm) sieve and asphalt binder and tested using the DMA (Lytton et al. 2005). The asphalt mastic of mix *AF* consisted of 97 percent limestone screenings and 3 percent hydrated lime; mix *BF* consisted of 72 percent natural sand and 28 percent limestone sand; and mix *CF* consisted of 50 percent natural sand and 50 percent limestone sand. The DMA samples were prepared by mixing the filler and the asphalt binder prior to mixing with the rest of the aggregates using a mechanical mixer. After short-term oven aging for 2 h at 135 °C (275 °F), the SGC was used to compact the asphalt mastic samples to 152 mm (6 in) diameter by 85 mm (3.4 in) height. Next, the sides of the samples were trimmed to a height of 50 mm (2 in), and several samples 12 mm (0.48 in) in diameter were cored out of the compacted sample as shown in Figure 7.2.

Figure 7.2. Typical asphalt mastic samples used for the DMA test

Some of the asphalt mastic samples were moisture conditioned following a method established by Kim et al. (2004) in which the samples are placed in distilled water under vacuum

for 1 h. The saturation level of the samples, measured using Equation 2.10, was 125 percent on average, indicating that water not only permeated into the voids but also diffused into the asphalt binder.

The testing of the asphalt mastic samples was similar to that of the asphalt mixes, except that the DMA applies dynamic shear while the asphalt mixes were tested using a direct tension tests. The dry and wet asphalt mastic samples were subjected to a sinusoidal shear strain in the DMA in order to evaluate the accumulation of damage. The linear viscoelastic properties of the asphalt mastic samples were determined by applying a low static shear strain level, and fatigue damage was evaluated by applying a high cyclic shear strain level (Lytton et al. 2005). All DMA tests were performed at room temperature. The high cyclic shear strain test was performed until sample failure and the number of applied load cycles recorded as N_f. The collected data were used to estimate the input parameters for the crack growth index (Equation 6.19). As shown subsequently, variability in the crack growth index can be reduced by normalizing with respect to tensile strength. Therefore, the normalized crack growth index denoted by R was estimated as:

$$R = c.g.i.\left(\sigma_t^2\right)^{\frac{2n+1}{n}} \tag{7.1}$$

$$R = \left[(2n+1)^{\frac{1+n}{2n+1}}\left(\frac{bE_R}{4\pi E_1 \Delta G_f}\right)^{\frac{n}{2n+1}}\left(N^{\frac{1}{1+n}} - 1^{\frac{1}{1+n}}\right)^{\frac{1+n}{2n+1}}\right] \tag{7.2}$$

This data analysis was identical to that applied to the asphalt mixes presented in the previous chapter.

Results

Table 7.4 presents a summary of the average input parameters used to estimate the crack growth index $c.g.i.$ (Equation 6.19) and the normalized crack growth index R (Equation 7.2) for the asphalt mixes, including the values of E_1, m, n, E_R, b, σ_t, and ΔG_f. As mentioned in the previous chapter, when calculating the DPSE, the viscoelastic properties and E_R are associated with the undamaged state, which is the dry state. Therefore, the values of E_1 and m in Equation 6.14, the value of S_o in Equation 6.17, and the value of E_R used to compute the pseudostrain correspond to the dry state. However, based on the derivation by Schapery and Lytton et al., the values of E_1

and *n* in Equation 6.19 correspond to the material surrounding the crack, either dry or moisture conditioned (Lytton et al. 1993; Schapery 1981).

Table 7.5 presents the average of the *c.g.i* and *R* results for the asphalt mixes at $N = 1000$ load cycles along with their coefficients of variation (COV). These results show that the variation in the results is reduced when normalizing with respect to the tensile strength value, which exhibited the highest variability among the measured material properties. The COV was higher under wet conditions for mixes *BF* and *CF*, which were more moisture susceptible as compared to mix *AF*. The parameters used to compute the normalized crack growth index *R* for the asphalt mastics are presented in Table 7.6.

Table 7.4. Average Surface Energy and Mechanical Test Parameters for the Asphalt Mix Samples

Mix type	E_1 (MPa)	m	$n = 1/m$	E_R * (MPa)	b	σ_t (kPa)	ΔG_f ** (J/m^2)
AF	1,728.2	0.1231	8.24	2,132.0	0.0122	350.7	0.1016
AF-MC	1,506.6	0.1185	8.53	2,714.5	0.0148	358.1	0.0953
BF	926.4	0.1044	9.85	1,462.1	0.0136	94.3	0.0904
BF-MC	590.2	0.1163	8.82	1,228.0	0.0125	60.4	0.0862
CF	1,106.5	0.1290	8.22	1,583.9	0.0160	96.2	0.0889
CF-MC	896.9	0.0987	10.18	1,425.4	0.0525	68.0	0.0569

* The E_R values for the MC samples are not used in the analysis, only the dry ones
** Using $S_i = S_{1000}$ in Equation 6.22

Table 7.5. Crack Growth Indices and COV for the Asphalt Mix Samples

Mix type	Crack growth index, *r*		Normalized crack growth index, *R*	
	Average	COV (%)	Average	COV (%)
AF	3.69	19.8	0.61	16.4
AF-MC	4.06	10.2	0.68	2.9
BF	13.05	25.6	0.73	25.5
BF-MC	27.56	40.7	0.88	23.6
CF	20.35	34.3	0.79	8.7
CF-MC	52.84	66.7	1.30	43.4

Table 7.6. Average Surface Energy and Mechanical Test Parameters for the Asphalt Mastic Samples

Mix type	E_I (MPa)	m	$n = 1/m$	E_R * (MPa)	b	ΔG_f ** (J/m^2)	N_f
AF	79.4	0.3142	3.18	75.0	145.8	0.1189	13,628
AF-MC	57.6	0.2299	4.35	–	105.5	0.0926	5,330
BF	30.1	0.5442	1.83	95.0	150.5	0.0875	5,521
BF-MC	34.1	0.3702	2.70	–	171.3	0.0699	1,633
CF	121.1	0.4511	2.22	61.0	74.5	0.0813	18,253
CF-MC	18.0	0.4581	2.18	–	180.6	0.0437	4,590

* Only the dry E_R values were reported in the study by Lytton et al. 2005
** Using a value of $\Delta G_{ba}{}^a$ based on the corresponding aggregate proportions used to prepare the asphalt mastic samples and considering $S_i = S_{Nf}$ in Equation 6.22 for the MC values

The values of R for the asphalt mixes and the asphalt mastics were plotted against the number of load cycles as shown in Figures 7.3 through 7.8. According to Figures 7.3 through 7.5, mix *AF* is the least moisture susceptible and mix *CF* is the most susceptible to moisture damage. Based on Figures 7.6 through 7.8, it is also apparent that the asphalt mastic fraction of mix *CF* is the most susceptible to moisture damage. The asphalt mastic of mix *BF* failed earlier than the asphalt mastic of mix *AF*. The failure point for the asphalt mastic of mix *BF*, around 4000 load cycles, corresponds to the number of load cycles at which the asphalt mastic of mix *CF* started to exhibit a rapid increase in the wet to dry ratio.
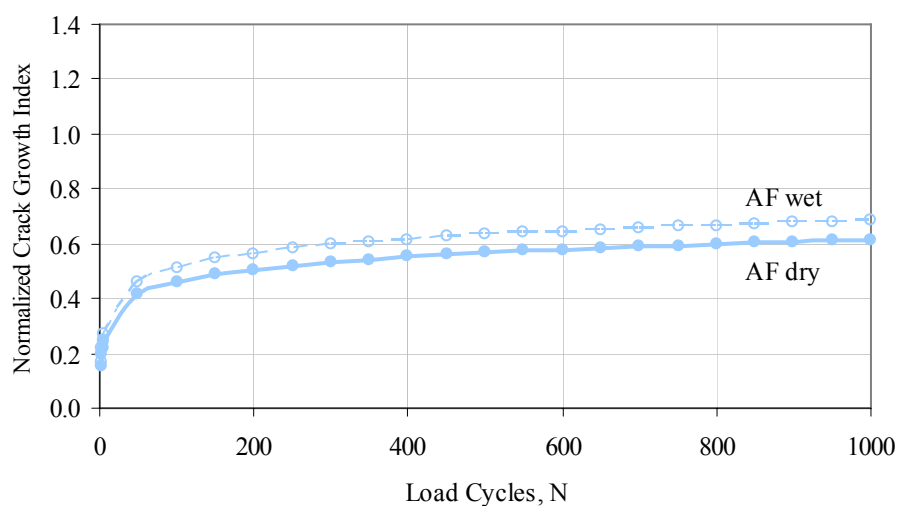
Figure 7.3. Normalized crack growth parameter for the asphalt mix samples of mix type *AF*
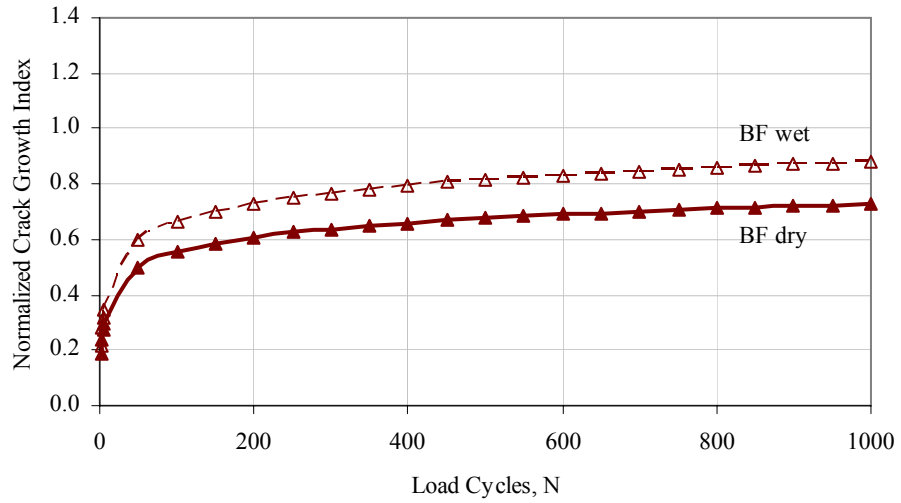
Figure 7.4. Normalized crack growth parameter for the asphalt mix samples of mix type *BF*
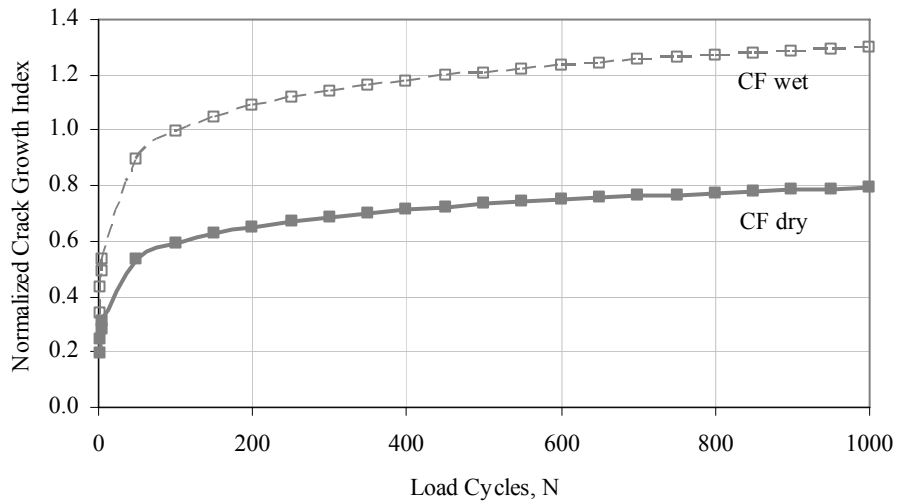
Figure 7.5. Normalized crack growth parameter for the asphalt mix samples of mix type *CF*
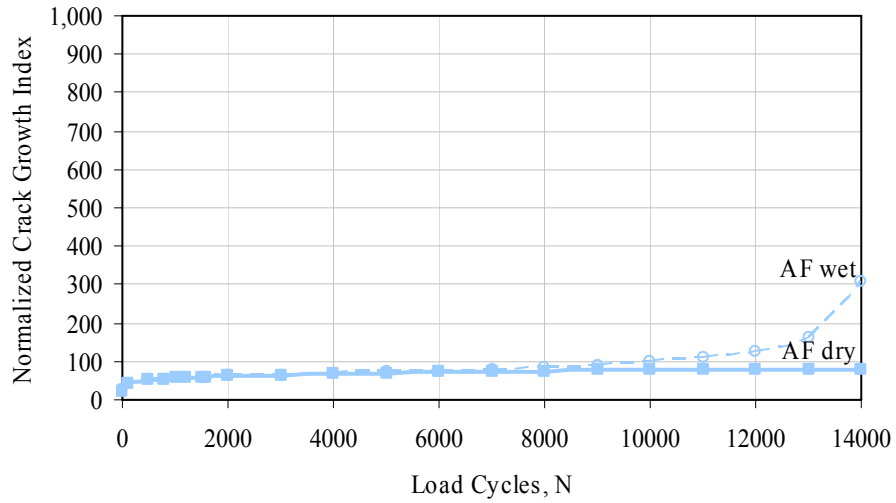
Figure 7.6. Normalized crack growth parameter for the asphalt mastic fraction of mix type *AF*
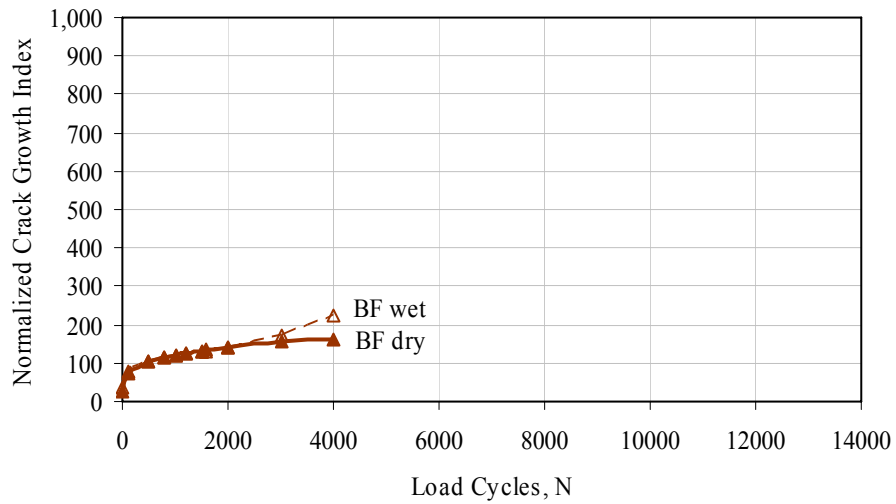
Figure 7.7. Normalized crack growth parameter for the asphalt mastic fraction of mix type *BF*
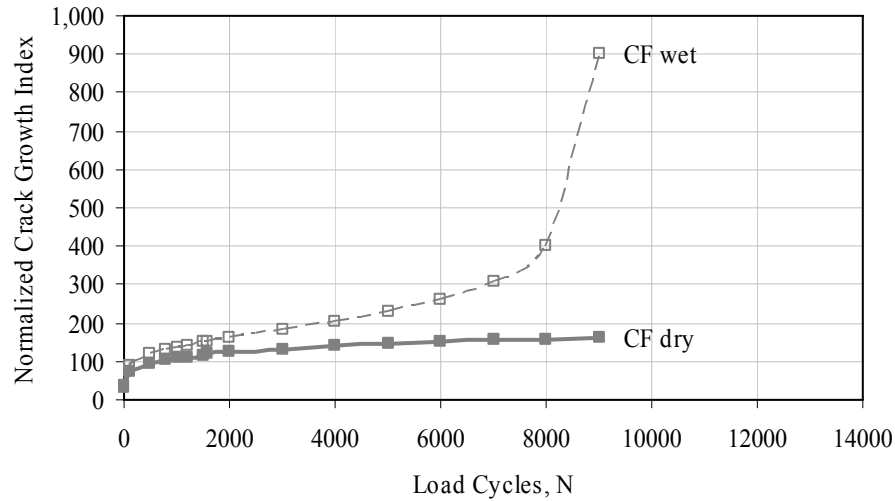
Figure 7.8. Normalized crack growth parameter for the asphalt mastic fraction of mix type *CF*

To assess the effect of the adhesive bond energy between the asphalt and the aggregate, the unconditioned to conditioned ratio, $\dfrac{\Delta G_{ba}{}^a}{\Delta G_{bwa}{}^a}$, previously presented in Table 7.3 was compared to the conditioned (wet) to unconditioned (dry) ratio of the normalized crack growth index for the asphalt mixes, R^{wet}/R^{dry}, obtained using Equation 7.2 at $N = 1000$. The relationship between these two parameters is presented in Figure 7.9. The mix with the highest $\dfrac{\Delta G_{ba}{}^a}{\Delta G_{bwa}{}^a}$ ratio and a ratio of R^{wet}/R^{dry} closer to 1 is expected to be more resistant to moisture damage (Bhasin et al. 2006). Mix *CF* had the lowest $\dfrac{\Delta G_{ba}{}^a}{\Delta G_{bwa}{}^a}$ value and the ratio of R^{wet}/R^{dry} at $N = 1000$ was equal to 1.64, the highest among the three mixes. This observation confirms that mix *CF* is the most susceptible to moisture damage. On the other hand, mix *AF* had the highest $\dfrac{\Delta G_{ba}{}^a}{\Delta G_{bwa}{}^a}$ value and the lowest R^{wet}/R^{dry} value at $N = 1000$ of 1.11. Therefore, mix *AF* is considered the least prone to moisture damage among the analyzed mixes, which is consistent with the reported field performance.
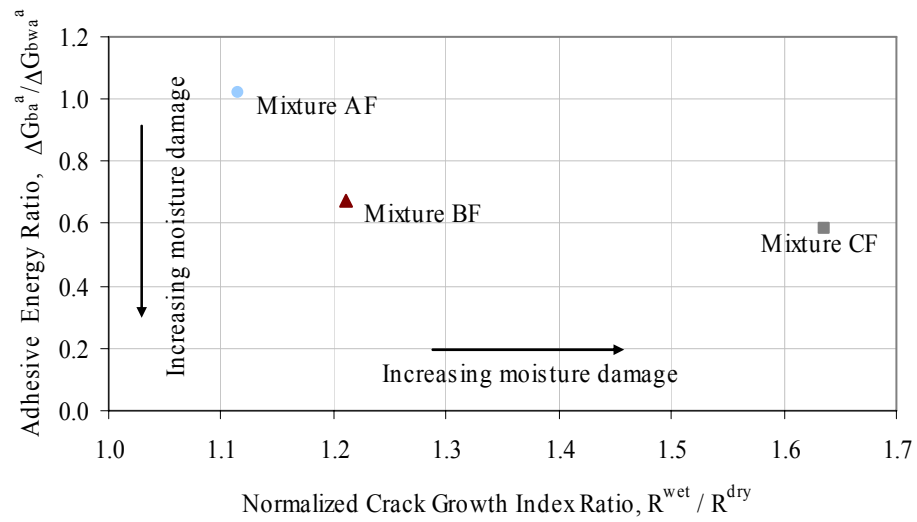
Figure 7.9. Adhesive bond energy ratio versus the normalized crack growth index ratio for the asphalt mix samples

CHAPTER VIII
CONCLUSIONS, RECOMMENDATIONS, AND FUTURE RESEARCH

Transportation infrastructure in general and roads in particular are an important asset of every country, allowing social and economic development. With the increasing demand on the street and highway system, the condition, functionality, and serviceability of the roads are critical and therefore every year billions of dollars are spent on maintenance. Many of the distresses that occur in asphalt pavement initiate or increase in severity due to moisture. Moisture damage is the term used to encompass the negative effects and functional deterioration that moisture in liquid or vapor form causes on the pavement. Two main goals were set for this study:

1) to explore the mechanisms of water transport in asphalt mixes, and

2) to identify the influence of air void structure on moisture damage.

Asphalt mix samples were prepared in the laboratory using two different gradations and trimming different sections from the bottom and top to increase the differences in air void structures. X-ray CT and image analysis techniques were utilized to estimate the air void content, size distribution, and connectivity. These results were used to study the mechanisms of capillary rise and permeability. The results of the capillary rise experiment based on the capillary rise, Washburn, and Laplace equations were able to show the influence of air void size on water rise and contact angles. Also, the rate of moisture infiltration was estimated, which can be useful to explore the causes of moisture damage in dry regions where capillary rise and moisture infiltration could be the main sources of moisture in the asphalt pavement rather than infiltration of surface water.

In addition, dynamic and relaxation tests were used to estimate the moisture susceptibility of the asphalt mixes. The results showed that these tests were not consistent for that purpose, possibly because the compressive loads are supported mainly by the aggregates and not by the mastic, which is weakened during the moisture conditioning procedure. Therefore, it was considered necessary to develop a crack growth model based on fracture theory to evaluate the moisture susceptibility of the asphalt mixes in relation to their air void structure.

The crack growth model incorporated different fundamental material properties such as the adhesive bond surface energy and mechanical properties of the asphalt mix such as relaxation modulus, relaxation rate, dissipated pseudostrain energy, and tensile strength. The model was validated using mixes with known field performance prepared in the laboratory and results of

their corresponding mastic fractions acquired with the DMA. The advantage of the crack model is that it accounts for the interactions between fundamental chemical and mechanical properties of the materials and the mix rather than relying on a single test parameter like the traditional test methods that offer only a limited understanding of the factors influencing moisture damage.

A summary of the main findings of the moisture transport study, the dynamic and relaxation tests, and the crack growth model analysis and validation are presented next. Following, several recommendations for improving the mechanical test protocols are provided. At the end, a section that discusses future research is included.

Mechanisms of Moisture Transport

The mechanisms of moisture transport were explored using laboratory experiments and X-ray CT image analysis. The constant head method was used to measure the permeability of the samples for both gradation *A* and gradation *B* mixes. After several trials and test setups, no water flow was achieved and thus all samples were classified as impermeable. X-ray CT images were used to corroborate the permeability observations using an air void connectivity algorithm. The results showed no vertical air void connectivity in the samples, which corroborated the lack of experimental permeability and low estimated permeability values.

Capillary rise in asphalt mixes was evaluated using a laboratory setup, in which several samples were placed in a shallow water bath at a constant depth for a period of 36 days. Using an algorithm to align and subtract the X-ray images acquired at different times, the voids filled with water were estimated. Also, the connectivity algorithm was used to estimate the vertical air void connectivity of the analyzed samples. The contact angle between the water and the mastic was estimated using the radius or size of the connected air voids filled with water after a wetting period of 36 days. Based on the analyses, the following observations were made regarding the capillary rise experiment:

- Water rise was observed in the asphalt mix samples during the wetting period. Therefore, the mechanism of capillary rise of subsurface water in asphalt pavements could be an important factor contributing to moisture-induced distresses in asphalt pavements. The capillary rise phenomenon makes water more accessible to the asphalt binder in the mix. Given the relative humidity gradient between the voids filled with water and the asphalt-aggregate interface, moisture would be driven by

this gradient to diffuse through the asphalt binder or mastic film, ultimately debonding the binder from the aggregate.

- The samples in which smaller number of voids were filled with water corresponded to the moisture conditioned samples (*A1-MC*, *A2-MC*), and the unconditioned sample with the smallest sizes of connected air voids (*A2*). The moisture conditioned samples have a smaller relative humidity gradient between the interior of the sample and the source of water. As such, these samples are expected to have smaller contact angles than their dry counterparts. The rate of capillary rise in a sample is directly proportional to the void radius (Washburn equation). Therefore, although *A2* is expected to ultimately have higher capillary rise than the other unconditioned samples (*A1*, *B1,* and *B2*), the rate of capillary rise in *A2* is much slower.

- The radii or sizes of voids that were filled with water and the height of water rise were used in the capillary rise equation to calculate the distribution of contact angles in the samples. The average contact angle between the water and the mastic in these samples was between 59° and 71°. The sample with the highest percent of voids filled with water at the end of the wetting period had the smallest average contact angle.

- The measurements were limited by the image resolution, and thus it is reasonable to expect smaller voids to be present in the mixes, which would have had a higher capillary rise than that measured. The average contact angles calculated in this study can be used to estimate the capillary rise in smaller voids.

- Smaller voids have higher capillary rise under static equilibrium with water weight. However, it takes more time for water to rise in these smaller voids.

- The results showed that some samples had more voids filled with water after moisture conditioning than the connected voids in the dry state. This phenomenon is attributed to the damage cause by moisture conditioning leading to more connected voids with access to moisture.

- These findings can be incorporated in the mix design process in order to achieve an optimum air void structure with the highest resistance to moisture transport within the life of the pavement.

Dynamic and Relaxation Tests

A dynamic modulus test and direct tensile and compressive relaxation tests were evaluated in this study in terms of their effectiveness in evaluating moisture susceptibility. The direct tensile and compressive relaxation test results were used to calculate the relaxation modulus with a power function. The estimated relaxation moduli, obtained at different temperatures, were shifted to a reference temperature of 20 °C (68 °F) using the Arrhenius equation. In addition, the results of the dynamic test were used to describe the dynamic modulus of the samples by means of a sigmoidal function. With the use of temperature shift factors, the dynamic moduli obtained at different test temperatures were shifted to a reference temperature of 21.1 °C (70 °F). A statistical t-test was used to estimate the difference between the unconditioned and conditioned responses for each sample type and to assess the effectiveness of the tests to capture moisture susceptibility. An ANOVA was used to estimate the difference in response between the various mix types within each condition.

The results of the dynamic modulus test were converted from frequency-domain to time-domain using three different approximation methods. The results were fitted to a master curve using the Arrhenius equation and then compared to the fitted compressive relaxation modulus results using a statistical t-test and average relative differences. Based on the results of the statistical analysis, the following observations were made:

- The dynamic modulus results performed on the 150 mm (6 in) height samples, which is the standard size specified by the AASHTO standard, showed no differences between the unconditioned and conditioned response and no differences among the different mix types within each condition. The dynamic modulus results for the 100 mm (4 in) height samples showed some differences between the unconditioned and conditioned responses. Also, some differences among the dynamic modulus of the unconditioned mixes were detected but no differences were shown for the conditioned mixes.

- The statistical analysis of the tensile and compressive relaxation test results showed differences among the different mix types within each condition. Differences were also detected between the unconditioned and conditioned responses for the tensile results of mixes *A1* and *B1*, while for the compressive results differences were only detected for mix *B1*.

- Based on the statistical analysis results, it is concluded that neither the dynamic test nor the relaxation test was consistent to evaluate the moisture susceptibility of the asphalt mixes. The direct tensile relaxation test provided better results, distinguishing between the unconditioned and conditioned response of two of the four mix types, and providing more reasonable conclusions when comparing the results of the mixes within each condition. Since the moisture conditioning procedure weakens the asphalt-binder adhesive bond strength and deteriorates the interface between the two materials, the tensile relaxation test better captures the interface strength. On the other hand, because the compressive test depends more on the aggregate structure, it is less affected by the weakening of interface strength of the material.

- The Schapery and Park approximation and the Ninomiya and Ferry interconversion gave better conversions between the frequency-domain data and the time-domain data. However, for some of the mixes, none of the approximation methods used yielded a good conversion between frequency-domain data and time-domain data.

Crack Growth Model and Validation

Several qualitative and quantitative methods have been developed in the past for the evaluation of moisture damage. Qualitative methods are based on a subjective visual assessment of damage, while the majority of the quantitative methods rely on measuring the change of a single test parameter (indirect tensile strength, dynamic modulus, etc.) after moisture conditioning. These approaches do not account for the interactions between the fundamental chemical and mechanical properties of the mix constituents and therefore offer only a limited understanding of the factors influencing moisture damage. To overcome these shortcomings, a crack growth model based on Paris' law for viscoelastic materials was developed to assess the moisture susceptibility of asphalt mixes and asphalt mastics. The advantages of the method are that its derivation is based on principles of fracture mechanics and that it accounts for several fundamental chemical and mechanical material properties.

The method was used to estimate the effect of air void structure on moisture susceptibility by means of calculating the crack growth index (*c.g.i.*) of moisture conditioned and unconditioned asphalt mix samples prepared in the laboratory. The parameters for the *c.g.i.* equation were obtained from different mechanical and surface energy tests. The ratio of the *c.g.i.*

between the conditioned and the unconditioned results showed that mix *A1*, which had a uniform air void structure and the lowest range of both air void content and air void size, was the most susceptible to moisture damage. These results emphasize the importance of determining a mix design and compaction method that would develop an air void structure that has optimum resistance to moisture damage.

The method was further validated using asphalt mixes and their asphalt mastic fraction. For the asphalt mixes, the normalized crack growth index, *R*, and the wet to dry ratio of this index (R^{wet}/R^{dry}) agreed with reported field performance. For the mastics, the DMA was used to test the samples and obtain the model parameters. The data analysis for the mastics showed similar results to that for the asphalt mixes in terms of differentiating between the conditioned and unconditioned behavior and in terms of a ranking of the mixes according to reported field performance.

Recommendations

The relaxation test was used to estimate the viscoelastic properties of the mix, the dynamic direct tensile test was used to estimate the DPSE and the reference modulus, while the tensile test was used to estimate the tensile strength of the asphalt mixes. The strain levels for the relaxation and dynamic direct tensile test were selected based on previous experience with a low strain level for the relaxation modulus test in order to avoid causing damage and a higher strain level for the direct dynamic tensile test. These strain magnitudes, however, simulated a percent of the failure strain (ε_f in Equation 6.21) obtained from a tensile strength test at 20 °C; 20 percent of ε_f for the relaxation test and 35 percent of ε_f for the dynamic direct tensile test (Walubita 2006). Based on the results of this study and the previous observations, the following changes to the test protocols are recommended:

- Perform the tensile test at 20 °C (68 °F) instead of 30 °C (86 °F) and use this temperature as a reference to construct the relaxation master curve.
- Perform the tensile test at a loading rate of 1.25 mm/min (0.05in/in) instead of 0.25 mm/min (0.01in/in) in order to minimize the secondary creep effects and to obtain a precise peak strain value. Apply the load until sample failure or until the peak load decreases by 25 percent, whichever occurs first.

- Estimate the strain level for the relaxation modulus test based on tensile strength results performed on trial samples. Consider a strain level of 20 percent of the value of the failure strain, ε_f, if the results are obtained at 20 °C (68 °F). If a higher temperature is used for the tensile test, for example 30 °C (86 °F) as used in this study, the percent of the failure strain should be around 10 percent.

- Estimate the strain level for the dynamic direct tensile test based on tensile strength results performed on trial samples. Consider a strain level of 35 percent of the value of the failure strain, ε_f, if the results are obtained at 20 °C (68 °F). If a higher temperature is used for the tensile test, for example 30 °C (86 °F) as used in this study, the percent of the failure strain should be around 17 percent.

- Use a set of replicates for the relaxation modulus and dynamic direct tensile test and a different set of replicates for the tensile strength test.

- Perform the dynamic direct tensile test at 20 °C (68 °F) instead of 30 °C (86 °F). The selected temperature needs to match the reference temperature used to construct the relaxation master curve.

Future Research

This section offers some ideas for future research that stem from the observations of this study. The ideas are arranged in topics; first, topics related to the crack growth model are discussed, followed by air void structure and moisture transport.

Crack Growth Model

The results of the crack growth index show very good results in evaluating the moisture susceptibility of asphalt mixes and asphalt mastics and assessing the effect of air void structure. Additional mixes and asphalt mastic samples should be studied to corroborate the effectiveness of the model, especially open graded mixes and mixes with known field performance.

The crack growth index equation should also be further developed as a probabilistic analysis tool. The probabilistic effect of moisture damage on crack growth should be obtained by estimating the fracture growth distribution of different mixes. This can be achieved by considering probability distributions of variables such as the void content, size, aspect ratio, roundness, eccentricity, and length. The aspect ratio and the roundness should be used to distinguish air voids from cracks. Also, it would be of significance to determine where the cracks

occur in terms of their eccentricity, or in other words, how far away from the center of the sample the cracks initiate. This could give a better understanding of the spatial distribution of damage.

The parameters for the crack growth model were obtained by performing tests in a controlled strain mode. The use of tests conducted in a controlled stress mode should also be explored. Current research explores the relationship between these two modes of loading in mastic samples using the DMA (Masad et al. 2007). This type of analysis should be extrapolated to asphalt mixes as well.

Alternative moisture conditioning procedures should also be explored, and a unified moisture conditioning method for asphalt mixes should be proposed.

The effect of asphalt binder aging should be explored and taken into account in the crack growth model; surface energy measurements on aged binders are an alternative to incorporating this effect.

Air Void Structure

From the results of the study, it is clear that the average air void content is not enough to understand the effects of moisture damage. The air void structure or change of air void content and air void size with depth plays an important role in understanding the occurrence of moisture damage. Additional studies of the effect of the horizontal air void distribution, connectivity, and permeability should be conducted.

Other compaction processes besides the SGC should be explored in the laboratory, and field cores subjected to diverse compaction equipment and compaction patters should be studied. Once an optimum air void structure is identified, studies should be conducted to identify how to achieve these air void structures in the field.

Moisture Transport

This study focused on capillary rise of water in asphalt mixes. Researchers have measured the moisture diffusion coefficients in mastic samples and reported difficulties providing accurate readings of the same type of measurements in asphalt mixes, mainly because of the complexity and heterogeneity of the material (Kassem et al. 2006). The high variability observed in the measurements was related to the location of the measuring devices within the sample. To overcome these shortcomings, a numerical model should be used to obtain the moisture diffusion

characteristics and diffusion coefficients of the asphalt mix. X-ray CT images should be used to discretize the three different phases: air voids, mastic, and aggregates, and a non-steady moisture diffusion equation can be solved for all three material phases under specific boundary conditions. This result could establish whether it is possible for moisture to diffuse into the asphalt mix under a relative humidity gradient, provide information on the influence of microstructure distribution on moisture diffusion, and determine the rate of moisture diffusion in the mastic.

REFERENCES

Airey, G. D., and Choi, Y.-K. (2002). "State of the Art Report on Moisture Sensitivity Test Methods for Bituminous Pavement Materials." *Road Materials and Pavement Design*, 3/4, 355-372.

Al-Omari, A., and Masad, E. (2004). "Three Dimensional Simulation of Fluid Flow in X-Ray CT Images of Porous Media." *International Journal for Numerical and Analytical Methods in Geomechanics*, 28(13), 1327-1360.

Al-Omari, A., Tashman, L., Masad, E., Cooley, A., and Harman, T. (2002). "Proposed Methodology for Predicting HMA Permeability." *Journal of the Association of Asphalt Pavement Technologists*, 71, 30-58.

Al-Rousan, T., Masad, E., Myers, L., and Speigelman, C. (2005). "A New Methodology for Shape Classification of Aggregates Used in Asphalt Mixes." *Transportation Research Board 84th Annual Meeting,* TRB, Washington D.C.

Alam, M. M., Tandon, V., Nazarian, S., and Tahmoressi, M. (1998a). "Identification of Moisture-Susceptible Asphalt Concrete Mixes Using Modified Environmental Conditioning System." *Transportation Research Record*, 1630, 106-116.

Alam, M. M., Vemuri, N., Tandon, V., Nazarian, S., and Picornell, M. (1998b). "Evaluation of Environmental Conditioning System (ECS) for Predicting Moisture Damage Susceptibility HMAC." *Report 1455-2F*, Center for Highway Materials Research, El Paso, Texas.

American Association of State Highway and Transportation Officials (AASHTO). (2002a). "Bulk Specific Gravity of Compacted Asphalt Mixtures Using Saturated Surface-Dry Specimens." *T 166*. Standard Specifications for Transportation Materials and Methods of Sampling and Testing, American Association of State Highway and Transportation Officials, Washington, D.C.

American Association of State Highway and Transportation Officials (AASHTO). (2002b). "Effect of Water on Cohesion of Compacted Bituminous Mixtures." *T 165*. Standard Specifications for Transportation Materials and Methods of Sampling and Testing, American Association of State Highway and Transportation Officials, Washington, D.C.

American Association of State Highway and Transportation Officials (AASHTO). (2002c). "Percent Air Voids in Compacted Dense and Open Bituminous Paving Mixtures." *T 269*. Standard Specifications for Transportation Materials and Methods of Sampling and Testing, American Association of State Highway and Transportation Officials, Washington, D.C.

American Association of State Highway and Transportation Officials (AASHTO). (2002d). "Preparing and Determining the Density of Hot-Mix Asphalt (HMA) Specimens by Means of the Superpave Gyratory Compactor." *T 312*. Standard Specifications for Transportation Materials and Methods of Sampling and Testing, American Association of State Highway and Transportation Officials, Washington, D.C.

American Association of State Highway and Transportation Officials (AASHTO). (2002e). "Standard Method of Test for Determining Dynamic Modulus of Hot-Mix Asphalt Concrete Mixtures." *TP 62*. Standard Specifications for Transportation Materials and Methods of Sampling and Testing, American Association of State Highway and Transportation Officials, Washington, D.C.

American Association of State Highway and Transportation Officials (AASHTO). (2002f). "Standard Method of Test for Resistance of Compacted Asphalt Mixtures to Moisture-Induced Damage." *T 283*. Standard Specifications for Transportation Materials and Methods of Sampling and Testing, American Association of State Highway and Transportation Officials, Washington, D.C.

American Association of State Highway and Transportation Officials (AASHTO). (2003a). "Mixture Conditioning of Hot-Mix Asphalt (HMA)." *R 30*. AASHTO Provisional Standards, American Association of State Highway and Transportation Officials, Washington, D.C.

American Association of State Highway and Transportation Officials (AASHTO). (2003b). "Standard Method of Test for Determining Dynamic Modulus of Hot-Mix Asphalt Concrete Mixtures." *TP 62*. AASHTO Provisional Standards, American Association of State Highway and Transportation Officials, Washington, D.C.

American Association of State Highway and Transportation Officials (AASHTO). (2003c). "Superpave Volumetric Design for Hot-Mix Asphalt (HMA)." *PP 28*. AASHTO Provisional Standards, American Association of State Highway and Transportation Officials, Washington, D.C.

American Association of State Highway and Transportation Officials (AASHTO). (2003d). "Superpave Volumetric Mix Design." *MP 2*. AASHTO Provisional Standards, American Association of State Highway and Transportation Officials, Washington, D.C.

American Society of Testing and Materials (ASTM). (2006a). "Standard Guide for Computed Tomography (CT) Imaging." *E 1441*. Annual Book of ASTM Standards, American Society of Testing and Materials, West Conshohocken, Pennsylvania.

American Society of Testing and Materials (ASTM). (2006b). "Standard Test Method for Bulk Specific Gravity and Density of Compacted Bituminous Mixtures Using Automatic

Vacuum Sealing Method." *D 6752*. Annual Book of ASTM Standards, American Society of Testing and Materials, West Conshohocken, Pennsylvania.

American Society of Testing and Materials (ASTM). (2006c). "Standard Test Method for Effect of Moisture on Asphalt Concrete Paving Mixtures." *D 4867/D 4867M - 04*. Annual Book of ASTM Standards, American Society of Testing and Materials, West Conshohocken, Pennsylvania.

American Society of Testing and Materials (ASTM). (2006d). "Standard Test Method for Effect of Water on Compressive Strength of Compacted Bituminous Mixtures." *D 1075*. Annual Book of ASTM Standards, American Society of Testing and Materials, West Conshohocken, Pennsylvania.

American Society of Testing and Materials (ASTM). (2006e). "Standard Test Method for Materials Finer than 75 μm (No. 200) Sieve in Mineral Aggregates by Washing." *C 117-04*. Annual Book of ASTM Standards, American Society of Testing and Materials, West Conshohocken, Pennsylvania.

American Society of Testing and Materials (ASTM). (2006f). "Standard Test Method for Maximum Specific Gravity and Density of Bituminous Paving Mixtures Using Automatic Vacuum Sealing Method." *D 6857*. Annual Book of ASTM Standards, American Society of Testing and Materials, West Conshohocken, Pennsylvania.

American Society of Testing and Materials (ASTM). (2006g). "Standard Test Methods for Measurement of Hydraulic Conductivity of Saturated Porous Materials Using a Flexible Wall Permeameter." *D 5084*. Annual Book of ASTM Standards, American Society of Testing and Materials, West Conshohocken, Pennsylvania.

Applied Research Associates (ARA). (2004). "Guide for Mechanistic-Empirical Design of New and Rehabilitated Pavement Structures." *Report I-37A*, National Cooperative Highway Research Program, Champaign, Illinois.

Asphalt-Institute. (1995). "Performance Graded Asphalt Binder, Specification and Testing." *Report SP-1*, The Asphalt Institute, Lexington, Kentucky.

Bhasin, A., Masad, E., Little, D., and Lytton, R. (2006). "Limits on Adhesive Bond Energy for Improved Resistance of Hot Mix Asphalt to Moisture Damage." *Transportation Research Board 85th Annual Meeting,* TRB, Washington D.C.

Birgisson, B., Roque, R., and Page, G. C. (2003). "Evaluation of Water Damage Using Hot Mix Asphalt Fracture Mechanics." *Journal of the Association of Asphalt Pavement Technologists*, 72, 424-462.

Chandan, C., Sivakumar, K., Masad, E., and Fletcher, T. (2004). "Application of Imaging Techniques to Geometry Analysis of Aggregate Particles." *Journal of Computing in Civil Engineering*, 18(1), 75-82.

Chen, J.-S., Lin, K.-Y., and Young, S.-Y. (2004). "Effects of Crack Width and Permeability on Moisture-Induced Damage of Pavements." *Journal of Materials in Civil Engineering*, 16(3), 276-282.

Cheng, D. (2002). "Surface Free Energy of Asphalt-Aggregate System and Performance Analysis of Asphalt Concrete Based on Surface Energy." Ph.D. Dissertation, Texas A&M University, College Station, Texas.

Cheng, D., Little, D. N., Lytton, R. L., and Holste, J. C. (2002). "Use of Surface Free Energy Properties of the Asphalt-Aggregate System to Predict Moisture Damage Potential." *Journal of the Association of Asphalt Pavement Technologists*, 71, 59-88.

Christensen, D. W., and Anderson, D. A. (1992). "Interpretation of Dynamic Mechanical Test Data for Paving Grade Asphalt Cements." *Journal of the Association of Asphalt Pavement Technologists*, 61, 67-116.

D'Angelo, J., and Anderson, R. M. (2003). "Material Production, Mix Design & Pavement Design Effects on Moisture Damage." *Proc. Moisture Sensitivity of Asphalt Pavements: A National Seminar*, Transportation Research Board, San Diego, California, 187-201.

Devore, J. L. (2000). *Probability and Statistics for Engineering and the Sciences*, 5th Ed., Duxbury, Pacific Grove, California.

Elphingstone, G. M. (1997). "Adhesion and Cohesion in Asphalt-Aggregate Systems." Ph.D. Dissertation, Texas A&M University, College Station, Texas.

Emery, J., and Seddik, H. (1997). "Moisture Damage of Asphalt Pavements and Antistripping Additives: Causes, Identification, Testing, and Mitigation." Transportation Association of Canada, Ottawa, Canada.

Epps, J., Berger, E., and Anagnos, J. N. (2003). "Treatments." *Proc. Moisture Sensitivity of Asphalt Pavements: A National Seminar*, Transportation Research Board, San Diego, California, 117-177.

Federal Highway Administration (FHWA). (1996). "Highway Statistics Summary to 1995." US Department of Transportation, Washington, D.C.

Federal Highway Administration (FHWA). (1997). "Highway Statistics 1996." US Department of Transportation, Washington, D.C.

Federal Highway Administration (FHWA). (1998). "Highway Statistics 1997." US Department of Transportation, Washington, D.C.

Federal Highway Administration (FHWA). (1999). "Highway Statistics 1998." US Department of Transportation, Washington, D.C.

Federal Highway Administration (FHWA). (2000). "Highway Statistics 1999." US Department of Transportation, Washington, D.C.

Federal Highway Administration (FHWA). (2001). "Highway Statistics 2000." US Department of Transportation, Washington, D.C.

Federal Highway Administration (FHWA). (2002). "Highway Statistics 2001." US Department of Transportation, Washington, D.C.

Federal Highway Administration (FHWA). (2003). "Highway Statistics 2002." US Department of Transportation, Washington, D.C.

Federal Highway Administration (FHWA). (2004). "Highway Statistics 2003." US Department of Transportation, Washington, D.C.

Federal Highway Administration (FHWA). (2005). "Highway Statistics 2004." US Department of Transportation, Washington, D.C.

Federal Highway Administration (FHWA). (2006). "Highway Statistics 2005." US Department of Transportation, Washington, D.C.

Fletcher, T., Chandan, C., Masad, E., and Sivakumar, K. (2002). "Measurements of Aggregate Texture and Its Influence of Hot Mix Asphalt (HMA) Permanent Deformation." *Journal of Testing and Evaluation*, 30(6), 1-8.

Fredlund, D. G., and Rahardjo, H. (1993). *Soil Mechanics for Unsaturated Soils*, John Wiley & Sons Inc., New York.

Hefer, A. W. (2004). "Adhesion in Bitumen-Aggregate Systems and Quantification of the Effects of Water on the Adhesive Bond." Ph.D. Dissertation, Texas A&M University, College Station, Texas.

Hicks, R. G. (1991). "Moisture Damage in Asphalt Concrete: Synthesis of Highway Practice." *NCHRP Report 175*, National Cooperative Highway Research Program, Washington, D.C.

Hicks, R. G., Santucci, L., and Aschenbrener, T. (2003). "Introduction and Seminar Objectives." *Proc. Moisture Sensitivity of Asphalt Pavements: A National Seminar*, Transportation Research Board, San Diego, California, 3-35.

Hu, P. S., and Reuscher, T. R. (2004). "Summary of Travel Trends 2001 National Household Travel Survey." US Department of Transportation, Washington, D.C.

InstroTek. (2003a). "AggPlus System: Coarse and Fine Aggregates." <http://www.instrotek.com/AggPlusManualRev7.pdf> (December 3, 2006).

InstroTek. (2003b). "CoreLok Operator's Guide." <http://www.instrotek.com/CoreLokManualRev20.pdf> (December 3, 2006).

Kassem, E., Masad, E., Bulut, R., and Lytton, R. (2006). "Measurements of Moisture Suction and Diffusion Coefficient in Hot Mix Asphalt and Their Relationships to Moisture Damage." *Transportation Research Board 85th Annual Meeting,* TRB, Washington, D.C.

Ketcham, R. A., and Carlson, W. D. (2001). "Acquisition, Optimization and Interpretation of X-Ray Computed Tomographic Imagery: Applications to the Geosciences." *Computers & Geosciences*, 27(4), 381-400.

Ketcham, R. A., and Iturrino, G. J. (2005). "Nondestructive High-Resolution Visualization and Measurement of Anisotropic Effective Porosity in Complex Lithologies Using High-Resolution X-Ray Computed Tomography." *Journal of Hydrology*, 302(1-4), 92-106.

Kiggundu, B. M., and Roberts, F. L. (1988). "Stripping in HMA Mixtures: State-of-the-Art and Critical Review of Test Methods." *NCAT Report 88-02*, National Center for Asphalt Technology, Auburn, Alabama.

Kim, Y.-R., Little, D. N., and Lytton, R. L. (2004). "Effect of Moisture Damage on Material Properties and Fatigue Resistance of Asphalt Mixtures." *Transportation Research Board 83rd Annual Meeting,* TRB, Washington, D.C.

Kringos, N., and Scarpas, A. (2005). "Raveling of Asphaltic Mixes Due to Water Damage: Computational Identification of Controlling Parameters." *Transportation Research Board 84th Annual Meeting,* TRB, Washington, D.C.

Little, D. N., and Jones, D. R. (2003). "Chemical and Mechanical Mechanisms of Moisture Damage in Hot Mix Asphalt Pavements." *Proc. Moisture Sensitivity of Asphalt Pavements: A National Seminar*, Transportation Research Board, San Diego, California, 37-70.

Lottman, R. P. (1978). "Predicting Moisture-Induced Damage to Asphaltic Concrete." *NCHRP Report 192*, National Cooperative Highway Research Program, Washington, D.C.

Lottman, R. P. (1982). "Predicting Moisture-Induced Damage to Asphaltic Concrete: Field Evaluation." *NCHRP Report 246*, National Cooperative Highway Research Program, Washington, D.C.

Lytton, R. L., Masad, E. A., Zollinger, C., Bulut, R., and Little, D. (2005). "Measurements of Surface Energy and Its Relationship to Moisture Damage." *Report 0-4524-2*, Texas Transportation Institute, College Station, Texas.

Lytton, R. L., Uzan, J., Fernando, E. G., Roque, R., Hiltmen, D., and Stoffels, S. (1993). "Development and Validation of Performance Prediction Models and Specifications for Asphalt Binders and Paving Mixtures." *SHRP A-357*, Strategic Highway Research Program, Washington, D.C.

Masad, E. (2004). "X-Ray Computed Tomography of Aggregates and Asphalt Mixes." *Materials Evaluation*, 62(7), 775-783.

Masad, E., Al-Omari, A., and Lytton, R. (2006a). "A Simple Method for Predicting Laboratory and Field Permeability of Hot Mix Asphalt." *Transportation Research Board 85th Annual Meeting,* TRB, Washington, D.C.

Masad, E., Birgisson, B., Al-Omari, A., and Cooley, A. (2004). "Analytical Derivation of Permeability and Numerical Simulation of Fluid Flow in Hot-Mix Asphalt." *Journal of Materials in Civil Engineering*, 16(5), 487-496.

Masad, E., Branco, V. T. F. C., Little, D. N., and Lytton, R. L. (2007). "A Unified Method for the Dynamic Mechanical Analysis of Sand Asphalt Mixtures." *The International Journal of Pavement Engineering*, submitted for publication.

Masad, E., Castelblanco, A., and Birgisson, B. (2006b). "Effects of Air Void Size Distribution, Pore Pressure, and Bond Energy on Moisture Damage." *Journal of Testing and Evaluation*, 34(1), 1-9.

Masad, E., Luce, A., and Mahmoud, E. (2006c). "Aggregate Base Residual Stresses Affecting Geogrid Reinforced Flexible Pavement Response." *Report 5-1707-03-1*, Texas Transportation Institute, College Station, Texas.

Masad, E., Muhunthan, B., Shashidhar, N., and Harman, T. (1999). "Internal Structure Characterization of Asphalt Concrete Using Image Analysis." *Journal of Computing in Civil Engineering*, 13(2), 88-95.

Masad, E., Saadeh, S., Al-Rousan, T., Garboczi, E., and Little, D. (2005). "Computations of Particle Surface Characteristics Using Optical and X-Ray CT Images." *Computational Materials Science*, 34(4), 406-424.

Maupin, G. W. (2000). "Investigation of Test Methods, Pavements, and Laboratory Design Related to Asphalt Permeability." *Report VTRC 00-R24*, Virginia Transportation Research Council, Charlottesville, Virginia.

McGennis, R. B., Kennedy, T. W., and Machmehl, R. B. (1984). "Stripping and Moisture Damage in Asphalt Mixtures." *Report 253-1*, Center for Transportation Research, Austin, Texas.

Medani, T. O., and Huurman, M. (2003). "Constructing the Stiffness Master Curves for Asphaltic Mixes." *Report 7-01-127-3*, Delft University of Technology, Delft, The Netherlands.

Medani, T. O., Huurman, M., and Molenaar, A. A. A. (2004). "On the Computation of Master Curves for Bituminous Mixes." *Proc. Third EuroBitumen Congress*, Vienna, Austria.

Miller, J. S., and Bellinger, W. Y. (2003). "Distress Identification Manual for the Long-Term Pavement Performance Program." *Report FHWA-RD-03-031*, FHWA Office of Infrastructure Research and Development, McLean, Virginia.

Mohamed, E. H. H., Halim, A. O. A. E., and Kennepohl, G. J. (1993). "Assessment of the Influence of Compaction Method on Asphalt Concrete Resistance to Moisture Damage." *Construction and Building Materials*, 7(3), 149-156.

Mohammad, L. N., Herath, A., and Huang, B. (2003). "Evaluation of Permeability of Superpave Asphalt Mixtures." *Transportation Research Board 82nd Annual Meeting,* TRB, Washington, D.C.

Ninomiya, K., and Ferry, J. D. (1959). "Some Approximate Equations Useful in the Phenomenological Treatment of Linear Viscoelastic Data." *Journal of Colloid Science*, 14, 36-48.

Ohio Department of Transportation (ODOT). (2005). "2005 Construction and Material Specifications." Ohio Department of Transportation, Columbus, Ohio.

Sasaki, I., Moriyoshi, A., Hachiya, Y., and Nagaoka, N. (2006). "New Test Method for Moisture Permeation in Bituminous Mixtures." *Journal of the Japan Petroleum Institute*, 49(1), 33-37.

Schapery, R. A. (1981). "Nonlinear Fracture Analysis of Viscoelastic Composite Materials Based on a Generalized J Integral Theory." *Proc. Japan – U.S. Conference on Composite Materials*, Tokyo, Japan.

Schapery, R. A., and Park, S. W. (1999). "Methods of Interconversion Between Linear Viscoelastic Material Functions - Part II an Approximate Analytical Method." *International Journal of Solids and Structures*, 36, 1677-1699.

Si, Z. (2001). "Characterization of Microdamage and Healing of Asphalt Concrete Mixtures." Ph.D. Dissertation, Texas A&M University, College Station, Texas.

Solaimanian, M., Fedor, D., Bonaquist, R., Soltani, A., and Tandon, V. (2006). "Simple Performance Test for Moisture Damage Prediction in Asphalt Concrete." *Journal of the Association of Asphalt Pavement Technologists*, 75, 345-380.

Solaimanian, M., Harvey, J., Tahmoressi, M., and Tandon, V. (2003). "Test Methods to Predict Moisture Sensitivity of Hot Mix Asphalt Pavements." *Proc. Moisture Sensitivity of Asphalt Pavements: A National Seminar*, Transportation Research Board, San Diego, California, 77-110.

St. Martin, J., Cooley, L. A., and Hainin, H. R. (2003). "Production/Construction Issues for Moisture Sensitivity of Hot Mix Asphalt Pavements." *Proc. Moisture Sensitivity of Asphalt Pavements: A National Seminar*, Transportation Research Board, San Diego, California, 209-222.

Tandon, V., and Nazarian, S. (2001). "Modified Environmental Conditioning System: Validation and Optimization." *Report 1826-1F*, El Paso, Texas.

Tashman, L., Masad, E., D'Angelo, J., Bukowski, J., and Harman, T. (2002). "X-Ray Tomography to Characterize Air Void Distribution in Superpave Gyratory Compacted Specimens." *The International Journal of Pavement Engineering*, 3(1), 19-28.

Tashman, L., Masad, E., Peterson, B., and Saleh, H. (2001). "Internal Structure Analysis of Asphalt Mixes to Improve the Simulation of Superpave Gyratory Compaction to Field Conditions." *Journal of the Association of Asphalt Pavement Technologists*, 70, 605-645.

Terrel, R. L., and Al-Swailmi, S. (1994). "Water Sensitivity of Asphalt-Aggregate Mixes: Test Selection." *Report SHRP-A-403*, Strategic Highway Research Program, Washington, D.C.

Texas Department of Transportation (TxDOT). (1999). "Prediction of Moisture Induced Damage to Bituminous Paving Materials Using Molded Specimens." *Tex 531 C*. Test Procedures, Texas Department of Transportation, Austin, Texas.

Texas Department of Transportation (TxDOT). (2004a). "Hamburg Wheel-Tracking Test." *Tex 242 F*. Test Procedures, Texas Department of Transportation, Austin, Texas.

Texas Department of Transportation (TxDOT). (2004b). "Standard Specifications for Construction and Maintenance of Highways, Streets, and Bridges." Texas Department of Transportation, Austin, Texas.

Texas Department of Transportation (TxDOT). (2005). "Superpave Gyratory Compacting of Test Specimens of Bituminous Mixtures." *Tex 241 F*. Test Procedures, Texas Department of Transportation, Austin, Texas.

Tunnicliff, D. G., and Root, R. E. (1984). "Use of Antistripping Additives in Asphaltic Concrete Mixtures: Laboratory Phase." *NCHRP Report 274*, National Cooperative Highway Research Program, Washington, D.C.

VanOss, C. J., Chaudhury, M. K., and Good, R. J. (1988). "Interfacial Lifshitz-van der Waals and Polar Interactions in Macroscopic Systems." *Chemical Reviews*, 88(6), 927-941.

Walubita, L. F. (2006). "Comparison of Fatigue Analysis Approaches for Predicting Fatigue Lives of Hot-Mix Asphalt (HMAC) Mixtures." Ph.D. Dissertation, Texas A&M University, College Station, Texas.

Washburn, E. W. (1921). "The Dynamics of Capillary Flow." *The Physical Review*, 17(3), 273-283.

Wolf, P. R., and Ghilani, C. D. (2002). *Elementary Surveying: An Introduction to Geomatics*, 10th Ed., Prentice Hall, Upper Saddle River, New Jersey.

Young, J. F., Mindess, S., Gray, R. J., and Bentur, A. (1998). *The Science and Technology of Civil Engineering Materials*, Prentice Hall, Upper Saddle River, New Jersey.

Zollinger, C. J. (2005). "Application of Surface Energy Measurement to Evaluate Moisture Susceptibility of Asphalt and Aggregates." M.S. Thesis, Texas A&M University, College Station, Texas.

APPENDIX A

ASPHALT BINDER SURFACE ENERGY CALCULATIONS

The contact angle between the asphalt-coated plates and water, formamide, and glycerol were measured and reported in Table 3.2. Since the properties of these solvents are known (Table 3.1.), Equation 2.15 presented in Chapter II was solved as a system of three equations with three unknowns (γ_S^{LW}, γ_S^-, and γ_S^+) as previously presented in Equation 2.16:

$$\begin{bmatrix} y_1 \\ y_2 \\ y_3 \end{bmatrix} = \begin{bmatrix} a_{11} & a_{12} & a_{13} \\ a_{21} & a_{22} & a_{23} \\ a_{31} & a_{32} & a_{33} \end{bmatrix} \begin{bmatrix} x_1 \\ x_2 \\ x_3 \end{bmatrix} \tag{A.1}$$

The values of the coefficients to form the 3×3 matrix were estimated using Equations 2.17 through 2.19 and the surface energies of the solvents reported in Table 3.1. The matrix of coefficients is presented as follows with $i = 1 =$ water, $i = 2 =$ formamide, and $i = 3 =$ glycerol:

$$\begin{bmatrix} 0.1283 & 0.2153 & 0.1822 \\ 0.1387 & 0.0521 & 0.0593 \\ 0.1387 & 0.2170 & 0.2368 \end{bmatrix} \tag{A.2}$$

The inverse of the matrix of coefficients is:

$$\begin{bmatrix} 0.4483 & 9.5239 & -2.7302 \\ 20.4881 & -4.2360 & -14.7075 \\ -19.0405 & -1.6982 & 19.3032 \end{bmatrix} \tag{A.3}$$

The measured contact angles are used to estimate the values of the y vector in Equation A.1 for both the advancing and receding angles. These values are shown in Table A.1.

Table A.1. Values of the y Parameters Used to Calculate the Surface Energy of the Asphalt Binder

Coefficient	Advancing	Receding
y_1	0.9656	1.4667
y_2	1.1009	1.7115
y_3	1.0569	1.5660

Using the results of Equation A.3 and the values presented in Table A.1, the estimated x_1, x_2, and

x_3 values corresponding to $\sqrt{\gamma_S^{LW}}$, $\sqrt{\gamma_S^-}$, and $\sqrt{\gamma_S^+}$ for the PG 76-22 asphalt binder sample for

both the advancing (healing) and receding (fracture) measurements are calculated and presented

in Table A.2.

Table A.2. Values of the x Parameters Used to Calculate the Surface Energy of the Asphalt
Binder

Coefficient	Advancing	Receding
x_1	8.0322	12.6827
x_2	-0.4234	-0.2318
x_3	0.1455	-0.6048

The value of the polar (AB) surface energy is computed using:

$$\gamma_S^{AB} = 2\sqrt{\gamma_S^+ \cdot \gamma_S^-} \tag{A.4}$$

and the total surface energy is computed as the sum of the AB and LW values (Equation 2.3). The

final surface energy components are reported in Table 3.3.

APPENDIX B

GRADATION B MIX DESIGN

The procedure followed to obtain the mix design for gradation *B* is explained in this appendix. Based on the design asphalt content of gradation *A*, an estimated binder content of 5.4 percent by weight of mix and two additional binder contents, one 0.5 percent above the estimated content (5.9 percent by weight of mix) and the other 1.0 percent above the estimated content (6.4 percent by weight of mix) were used. Replicates of loose and compacted asphalt mix samples were prepared for every binder content to calculate the Rice or maximum specific gravity (G_{mm}) and the bulk specific gravity (G_{mb}). The G_{mm} value was determined using loose asphalt mix samples of about 2,000 g each employing the Corelok® system (ASTM 2006a; InstroTek 2003b). The G_{mb} value was determined on compacted asphalt mix samples of about 4500 g each using the saturated surface-dry method (AASHTO 2002e). The compacted samples were prepared in the SGC using a design number of gyrations (N_{des}) of 100. The individual and average replicate results are presented in Table B.1.

Table B.1. Maximum Specific Gravity and Bulk Specific Gravity Results for Every Trial Asphalt Binder Content

Asphalt binder content (%)	Replicate	G_{mm} Individual	G_{mm} Average	G_{mb} Individual	G_{mb} Average
5.4	1	2.400	2.398	2.238	2.256
	2	2.396		2.273	
5.9	1	2.379	2.382	2.263	2.277
	2	2.385		2.290	
6.4	1	2.365	2.361	2.284	2.278
	2	2.356		2.271	

To estimate and revise the design binder content the volume of air (V_a), the voids filled with asphalt (*VFA*), and voids in the mineral aggregate (*VMA*) were computed as follows:

$$V_a = 100\left(1 - \frac{G_{mb}}{G_{mm}}\right)$$
(B.1)

$$VMA = 100\left(1 - \frac{G_{mb}P_s}{G_{sb}}\right) \tag{B.2}$$

$$VFA = 100\left(\frac{VMA - V_a}{VMA}\right) \tag{B.3}$$

where P_s is the percent of aggregate in the mix and G_{sb} is the bulk specific gravity of the combined aggregate:

$$G_{sb} = \frac{P_{fine} + P_{coarse}}{\dfrac{P_{fine}}{G_{sbfine}} + \dfrac{P_{coarse}}{G_{sbcoarse}}} \tag{B.4}$$

where P_{coarse} is the percentage by mass of aggregates larger than the no. 8 (2.36 mm) sieve, and P_{fine} is the percentage by mass of aggregates smaller than the mentioned size, which is defined as the primary control sieve size (AASHTO 2003d). In the case of gradation B, P_{fine} is 28 percent and P_{coarse} is 72 percent. The apparent bulk specific gravities for the coarse and fine fractions (G_{sbfine} and $G_{sbcoarse}$) were determined using the Corelok® system, and the values are reported in Table B.2 (InstroTek 2003a).

Table B.2. Bulk and Apparent Specific Gravities for the Fine and Coarse Fractions

Fraction	G_{sb}	G_{sa}
Fine	2.523	2.655
Coarse	2.598	2.631

Therefore, the bulk and apparent specific gravities of the combined aggregate were estimated as follows:

$$G_{sb} = \frac{28 + 72}{\dfrac{28}{2.523} + \dfrac{72}{2.598}} = 2.577 \tag{B.5}$$

$$G_{sa} = \frac{28 + 72}{\dfrac{28}{2.655} + \dfrac{72}{2.631}} = 2.638 \tag{B.6}$$

Using the averages presented in Table B.1 and the result of Equation B.5 in equations B.1, B.2, and B.3, the values of V_a, VMA, and VFA for every binder content were computed. The results are presented in Table B.3 and the corresponding plots in Figure B.1.

Table B.3. Volumetric Calculations for Every Trial Asphalt Binder Content

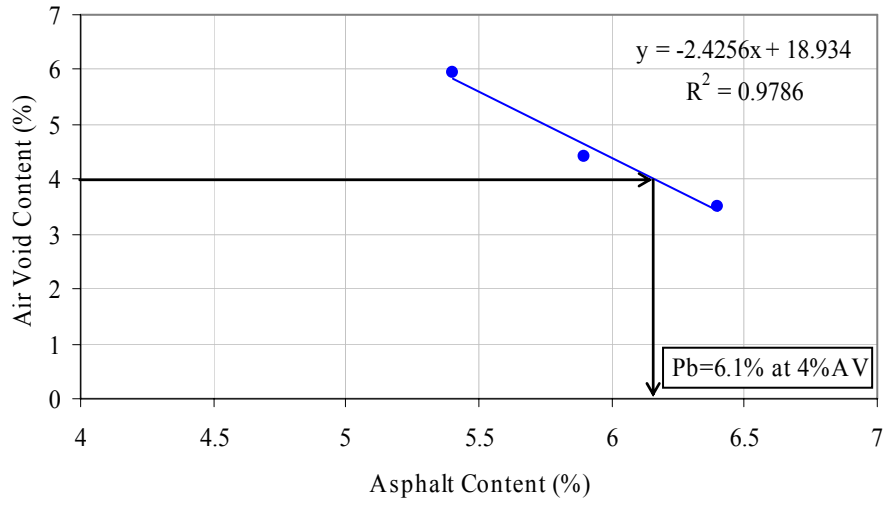| Asphalt binder content (%)	V_a (%)	VMA (%)	VFA (%)
5.4	5.9	17.2	65.4
5.9	4.4	16.8	73.8
6.4	3.5	17.3	79.6

Figure B.1. Percent air voids for every binder content and design binder content selection
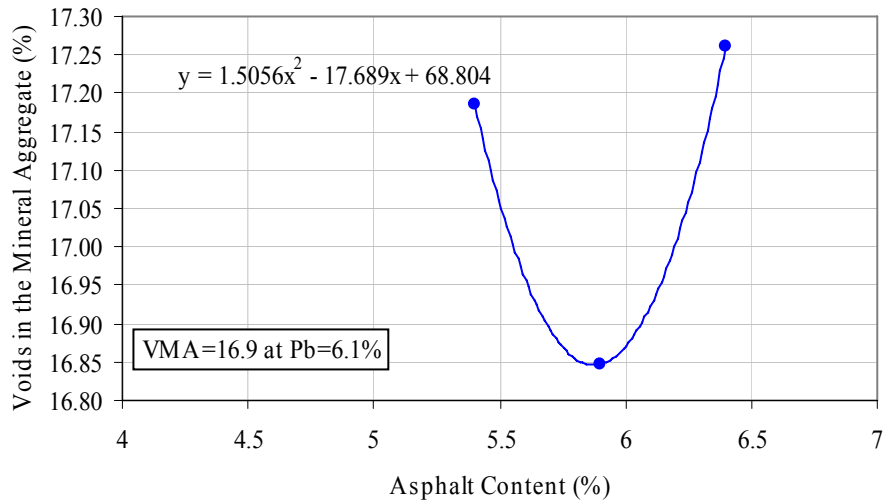

Figure B.2. Percent voids in the mineral aggregate for every binder content and corresponding value for the selected design binder content
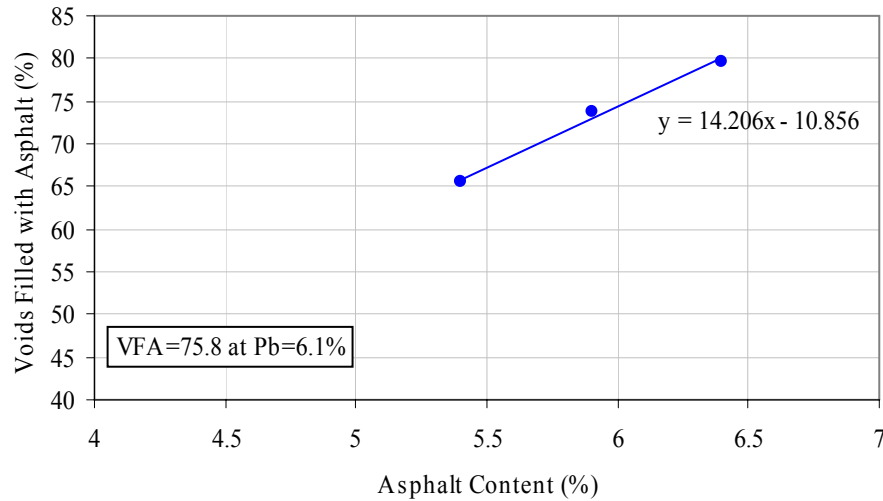
Figure B.3. Percent voids filled with asphalt for every binder content and corresponding value for the selected design binder content

The design binder content was determined from Figure B.1 using an air void value of 4 percent. The resulting design asphalt binder content for the selected target air voids was 6.1 percent by weight of mix. Using this value, the *VMA* and *VFA* values were estimated from Figures B.2 and B.3. These values along with the dust-to-binder ratio were verified against the requirements of Superpave mix design (AASHTO 2003d). The dust-to-binder ratio was computed as the ratio of the percent of material smaller than the no. 200 sieve (0.075 mm) and the effective binder content (P_{be}):

$$P_{be} = -(P_s \cdot G_b)\frac{(G_{se} - G_{sb})}{(G_{se} \cdot G_{sb})} + P_b \tag{B.7}$$

where G_b is the specific gravity of the binder equal to 1.03 g/cm^3 and G_{se} is the effective specific gravity of the combined aggregate calculated as follows:

$$G_{se} = G_{sb} + 0.8(G_{sa} - G_{sb}) \tag{B.8}$$

Substituting the previously acquired values, the following results are obtained:

$$G_{se} = 2.577 + 0.8(2.638 - 2.577) = 2.625 \tag{B.9}$$

$$P_{be} = -(93.9 \cdot 1.03)\frac{(2.625 - 2.577)}{(2.625 \cdot 2.577)} + 6.1 = -0.7 + 6.1 = 5.4 \tag{B.10}$$

$$\frac{P_{0.075}}{P_{be}} = \frac{4}{5.4} = 0.7 \tag{B.11}$$

A summary of the resulting mix design parameters for gradation *B* and a comparison against the required Superpave requirements is presented in Table B.4.

Table B.4. Mix Design Parameters and Superpave Requirements for Aggregate Gradation *B*

Parameter	Gradation *B*	Superpave Criteria
Design binder content by weight of mix	6.1	–
Percent voids in the mineral aggregate (*VMA*)	16.9	Minimum 14
Percent voids filled with asphalt (*VFA*)	75.8	65 to 78
Dust-to-binder ratio	0.7	0.6 to 1.2

APPENDIX C

SAMPLE SETUP FOR THE TENSILE TESTS

Several fundamental material properties need to be measured in order to obtain the input parameters for the crack growth model presented in Chapter VI. A tensile strength test is needed in order to obtain the maximum tensile strength under direct tensile loading. A relaxation modulus test is required to obtain the elastic relaxation modulus and the stress relaxation rate under direct static loading. In addition, a dynamic direct tension test is required to determine the rate of accumulation of fracture damage. The materials and test apparatus required for the tensile tests are detailed next. The procedures for fixing the LVDT holders and the load plates are detailed in Figure C.1.

Materials and Test Apparatus

- Loading mechanism
  - Capable of applying a continuous direct axial tensile load at a constant elongation (deformation) rate of 0.25 mm/min (0.01in/min) for a specified period (see Chapter VII for the tensile strength test description)
  - Capable of applying a tensile and compressive load to maintain a constant axial strain (deformation or displacement) in tension or compression mode for a specified loading period (see Chapter VI for the relaxation modulus test description)
  - Capable of applying a uniaxial repeated direct tensile load at a given strain level for a specified number of load cycles (see Chapter VII for the direct repeated tension test description)
  - Load cell capable of applying vertical loads of up to 24,241N (5000 lb) with an accuracy of $\pm 2\%$ of the required load level
- Temperature control system
  - Temperature-controlled cabinet or chamber capable of applying a range of temperatures between 10 °C and 30 °C (50 °F and 86 °F) and within ± 1 °C (± 2 °F) of the target test temperature

- o A thermocouple probe inserted inside an asphalt mix sample placed inside the temperature-controlled chamber for temperature monitoring purposes
- 3 LVDTs to measure the load-induced displacements with a resolution of at least 0.0025 mm (0.0001 in)
- Data acquisition system
  - o Computer system and software capable of recording the vertical deformation of the LVDTs and the applied load
- Loading plates
  - o Two loading plates to be attached to the upper and lower ends of the sample
  - o Both loading plates must be of the same diameter as the sample being tested to provide for positive centering of the sample under load
  - o The side of the loading plates attaching to the sample should be rough to provide an effective connection to the sample.
- Capping compound (2-ton epoxy) able to withstand at least 5000 N (1000 lb) loads at low and high temperatures
- Gluing compound (super glue) and an accelerator for attaching the LVDT holders to the samples
- Metal frame for gluing the load plates
- Allen wrench, spatula, markers, and ruler or straight edge

Figure C.1. LVDT Holders' and Load Plate Setup for the Tensile Tests

Step	Action
1	Clean, wipe with acetone, and dry the load plates.
2	Mix thoroughly equal parts of the 2-ton epoxy hardener and resin.

Figure C.1. Continued

Step	Action	
3	Place the bottom plate in the metal frame and apply the 2-ton epoxy mix to the bottom load plate using a spatula.	
4	Apply the 2-ton epoxy mix on the top end of the sample using a spatula.	
5	Place and center the sample on top of to the bottom load plate.	
6	Place the top load plate and apply some pressure (such as extra weight) to the sample. Allow the sample to set for about 24 h.	

Figure C.1. Continued

Step	Action
7	Mark the 120° positions around the sample diameter.
8	Using a ruler or a straight edge, mark a vertical line through the side of the sample using the 120° marks as guidelines.
9	Mark 25 mm (1 in) from the top edge and bottom edge of the sample.
10	Using an Allen wrench fix two clean LVDT holders with a center-to-center gap of 50 mm (2 in) using a caliper or ruler to measure the gap.

Figure C.1. Continued

Step	Action	
11	Apply epoxy glue to the LVDT holders and accelerator on the sample at the 25 mm (1 in) marks.	
12	Fix the LVDT holders on top of the 25 mm (1 in) marks. Make sure the LVDT holders are aligned with the vertical 120° line.	
13	Repeat steps 8 through 12 for the next 120° line.	

APPENDIX D

SAMPLE SETUP FOR THE DYNAMIC MODULUS TEST

In Chapter V dynamic and relaxation tests were presented in order to evaluate the moisture susceptibility of asphalt mixes. The materials and test apparatus are detailed next. Details of the LVDT holders' configuration are included in Figure D.1. The description of the sample setup for the dynamic modulus test is included in Figure D.2.

Materials and Test Apparatus

- Loading mechanism capable of applying a dynamic compressive load while keeping the strain within the required limits
- Temperature control system or chamber capable of applying a range of temperatures between 21.1 °C and 54.4 °C (70 °F and 130 °F) and within ± 1 °C (± 2 °F) of the target test temperature
- Thermocouple probe inserted inside an asphalt mix sample placed inside the temperature-controlled chamber for temperature monitoring purposes
- Data acquisition system capable of recording the vertical deformation of the LVDTs and the applied load
- IPC software and calibration files
- 3 LVDT holders and 3 LVDTs per sample to measure the load-induced displacements with a resolution of at least 0.0025 mm (0.0001 in)
- 3 Copper buttons per sample
- Two load plates of the same diameter of the sample
- Metal frame for marking the samples
- Gluing compound (super glue) and an accelerator for attaching the LVDT holders to the samples
- 2 mm (0.08 in) screwdriver with hexagonal rounded head
- Latex membranes
- Silicone grease
- Allen wrench, hexagonal head screws, markers, caliper, and ruler

Figure D.1. LVDT Holders' Configuration for the Dynamic Modulus Test

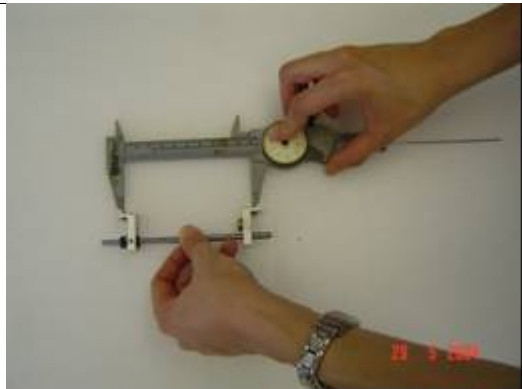| Step	Action	
1	Place the sample in the metal frame and mark the 120° positions.	
2	Using a ruler or a straight edge, mark a vertical line through the side of the sample using the 120° marks as guidelines.	
3	Detach and clean the copper buttons from sample or use new/clean ones if available	
4	Using an Allen wrench fix the LVDT holders to a center-to-center gap of 100 mm (4 in) for 150 mm (6 in) height samples and 50 mm (2 in) for the 10 mm (4 in) height samples. Use a caliper to measure the gap.	

Figure D.1. Continued

Step	Action	
5	Using a ruler or caliper mark 25 mm (1 in) from the top edge and bottom edge of the sample.	
6	Attach the copper buttons to the fixed LVDT holders.	
7	Apply epoxy glue to the sample at the 25 mm (1 in) mark.	
8	Fix the copper buttons on top of the glue spots. Make sure the LVDT holders are aligned with the vertical 120° lines.	

Figure D.1. Continued

Step	Action
9	Apply accelerator to the glue spots.
10	Remove the LVDT holders, attach another set of copper buttons, recheck the center-to-center gap, and proceed to step number 7 for the next position.
11	 Let the glue set for about 24 h before testing.

Figure D.2. Sample Setup for the Dynamic Modulus Test

Step	Action	
1	Introduce the samples into the environmental chamber of the loading equipment.	
2	Attach the LVDT holders to the sample starting with the bottom copper button and proceeding with the one on the top one. Use a 2 mm (0.08 in) round tip screw driver. Make sure the LVDT holders are securely fixed.	
3	Center the bottom plate, and place a double latex membrane greased with silicone on top of it.	
4	Sit the sample on top of the latex membranes and cover it with the other set of latex membranes already greased with silicone. Place the load plate on top.	
5	Insert the LVDTs in the holders and click the icon "levels" inside the dynamic modulus software screen.	

Figure D.2. Continued

Step	Action	
6	Adjust the LVDTs until the level on the screen reaches or it is close to zero and then fix the LVDT using the screw attached to the holder.	
7	Lower the ram to be almost in contact with the top load plate, centering the sample accordingly (use the groove on the top load plate as guideline).	
8	Click "start" on the software screen and close the "levels" screen.	
9	At the end of the frequency sweep, click the "fast" and "arrow up" buttons to bring the ram up and remove the top load plate and LVDTs from the sample.	
10	Remove the sample from the environmental chamber and unscrew the LVDT holders. Repeat step number 2 for the next samples to be tested.	

VITA

Edith Arámbula Mercado was born in Monterrey, Mexico. She received her Bachelor of Science (B.S.) in civil engineering from the Instituto Tecnológico y de Estudios Superiores de Monterrey (ITESM) in December of 1997. She worked as a project manager for the Kalos Industrial and Business Parks in Monterrey, Mexico, from June 1998 to February 2000. From March 2000 to December 2000, she worked for the Public Works Department of the City of San Pedro Garza Garcia, Mexico, developing and implementing a pavement management system. On January 2001, she joined the ITESM as a graduate student and worked as a graduate teaching assistant for the Department of Civil Engineering. She then started her Master of Science (M.S.) in civil engineering at Texas A&M University in August 2001, and received her M.S. in December of 2002. During that time, she worked as a graduate research assistant for the Texas Transportation Institute (TTI), conducting a research project sponsored by the Texas Department of Transportation (TxDOT). Afterward, she continued her studies at Texas A&M University, pursuing her Doctor of Philosophy (Ph.D.) in civil engineering while employed as a graduate research assistant for the TTI conducting a research project sponsored by the Federal Highway Administration (FHWA). In addition, during three different semesters of her Ph.D. studies she worked as a graduate teaching assistant for the Department of Civil Engineering. She received her Ph.D. in May of 2007.

Her permanent address is as follows:

Trinidad 225
Col. Vista Hermosa
Monterrey, Nuevo León, México
64620